Technische Universität München
Physik Department

Max-Planck-Institut für Astrophysik

A new scheme to treat neutrino effects in neutron-star mergers: implementation, tests and applications

Ricard Ardevol Pulpillo

Vollständiger Abdruck der von der Fakultät für Physik der Technischen Universität München zur Erlangung des akademischen Grades eines

Doktors der Naturwissenschaften (Dr. rer. nat.)

genehmigten Dissertation.

Vorsitzende:

- Prof. Dr. Laura Fabbietti

Prüfender der Dissertation:

- Apl. Prof. Dr. Hans-Thomas Janka
- Prof. Dr. Alejandro Ibarra

Die Dissertation wurde am 23.05.2018 bei der Technischen Universität München eingereicht und durch die Fakultat für Physik am 02.07.2018 angenommen.

Contents

Acknowledgements

First and foremost, I would like to thank my supervisor, Prof.Dr. Hans-Thomas Janka, for his dedication and investment in my education and my PHD project, which I trully appreciate. I also want to thank Oliver Just for his inestimable help, specially at the beginning of this new project, and for all the productive discussions, and to Andreas Bauswein who effectively introduced me to the world of computational astrophisics, provided the basis for this project and bestowed me with invaluable advice. I express my gratitude to the whole hydro-group, for always being the last one standing, and to all the other MPA groups with which I had the pleasure to interact. My thanks extend to the MPA system administrators, specially Andreas Weiss and Bernt Christandl, and to the MPA administration and secretariat, specially Frau Maria Depner. Not to forget the institutional support, I am grateful to the Max Planck Institute for Astrophysics, as well as the Max Planck for Computation and Data Facitlity, hosting the supercomputers Hydra and Draco, the Sonderforschungsbereich TR7 'Gravitationswellenastronomie', the Deutsche Forschungsgemeinschaft through the Excellence Cluster Universe (EXC 153) and the European Research Council.

M'agradaria donar les gràcies als meus pares, Josep i Margarida, pel seu constant suport i afecte, per l'educació que m'han brindat i per aguantar-me tots aquests anys. També m'agradaria donar les gràcies a la meva germana Aina, de qui estic molt orgullós, i a la resta de la meva família. I evidentment, no em puc oblidar de la Raquel, qui ha patit la pitjor part de aquest PHD amb estoicisme i comprensió, sense deixar ni un moment de cuidar-me i alentar-me a continuar endavant. Per tot això i molt més, gràcies.

This PHD would not have been possible (or so enjoyable) without the friendship, support and, in many cases too many interrupting knocks on my office door, provided by Anabele, Andreas, Jens, Matteo, Mattia, Max, Michael, Miranda, Ninoy, Phillip, Qingbo, Talytha, Vlas and all the other people from MPA (and MPE/USM/TUM) whith whom I have shared this experience... and some WAWBeers! I also want to acknowledge the people from the Spanish 'Ghetto' for providing a Spanish-like relaxed environment in Munich. After so many years abroad, I am endebted to Agus, Edu, Hector, Laia, Lucas, Pau, Selena and Yessica, for staying by my side and always finding a gap in their agendas to share with me. And finally, I dedicate a line to my cats, Dagon and Psyche, for fournishing my life with loveliness and exhasperation in comparable amounts.

Nobody expects the Spanish Inquisition!

1. Introduction

On August 17, 2017 the first gravitational wave (GW) signal from the collision (or merger) of two neutron stars (NSs) was detected by the Advanced LIGO and Advanced Virgo GW detectors (Abbott et al., 2017f). In the aftermath of the event, numerous observatories and space telescopes detected electromagnetic (EM) emission in multiple wavelengths at the same sky location (Soares-Santos et al., 2017; Cowperthwaite et al., 2017; Nicholl et al., 2017; Chornock et al., 2017; Margutti et al., 2017; Alexander et al., 2017; Fong et al., 2017), opening the door to a new era of *multi-messenger astronomy* (Abbott et al., 2017a).

Numerical simulations are instrumental in understanding the merger process of the two NSs and their observable signals. They have consistently shown, as proposed by Lattimer and Schramm (1974), that some material gets unbound from the system during and after the merger, with the appropriate conditions to synthesize a large fraction of the neutron-rich trans-iron elements we observe in the Solar System. Many of these newly-formed elements are radioactive, and their decay can power the EM emission of the so-called *kilonova* (Li and Paczyński, 1998) observed after the NS merger GW event (Soares-Santos et al., 2017; Cowperthwaite et al., 2017; Nicholl et al., 2017; Chornock et al., 2017). However, amongst the most prominent uncertainties in the modelling of NS mergers, are those related to the treatment of neutrinos. Neutrinos, by their emission and absorption, change the ratio of protons to neutrons in the ejected material, hence favouring or prohibitig the production of neutron-rich elements. It is in this context that we introduce an Improved Leakage-Equilibration-Absorption Scheme (ILEAS), a new computationally efficient method to describe neutrino effects in NS merger simulations which is designed to satisfy all important physics constraints.

1.1. Neutron star mergers in the era of multi-messenger astronomy

1.1.1. Neutron star binaries and their inspiral phase

Neutron stars are born from the collapsing cores of a massive stars in supernova (SN) explosions (Bethe and Wilson, 1985; Bethe, 1990). They are extremely compact objects, with typical masses in the range of $1 - 2$ times the mass of the Sun and radii of the order of ~ 10 km, thus reaching densities in their cores beyond those of atomic nuclei ($\rho_{\rm NS} \gtrsim \rho_{\rm nuc} \simeq 2.7 \cdot 10^{14}$ g/cm^3). The extreme conditions in the interior of NSs cannot be reproduced in a laboratory, and hence the exact com-

position of NSs remains a mystery. Although originally assumed to be composed mainly of neutrons, more exotic particles such as hyperons and mesons or even free quarks could also be present. Nevertheless, several constraints have been derived from nuclear experiments as well as from astrophysical observations (see Lattimer 2012 and Özel and Freire 2016 for recent reviews), which combined with approximate descriptions of the particle interactions allow for the creation of reasonable equation of state (EoS) models describing the properties of NS matter, widely used in numerical simulations (e.g. Shen et al. 1998; Hempel and Schaffner-Bielich 2010).

Up to date, there are observations of nearly a dozen binary systems composed of two NSs orbiting each other in our galaxy (Lattimer, 2012; Swiggum et al., 2015; Özel and Freire, 2016) and even though they have not yet been observed, binaries hosting a NS and a black hole (BH) are also expected to occur (e.g. Mennekens and Vanbeveren 2014; Postnov and Yungelson 2014; Dominik et al. 2015; Belczynski et al. 2016). The two compact objects (COs) in a binary, either two NSs or a NS and a BH[1], radiate energy and angular momentum away in the form of GWs, shrinking their orbit and, eventually, leading to a coalescence. If at least one of the COs is magnetized, the interactions of its magnetosphere with the conducting companion could power an X-ray/radio precursor to the merger (Palenzuela et al., 2013). Figure 1.1 illustrates the different phases of the merger and its associated GW or EM signals, which we will discuss in the following text one by one.

GWs were predicted in 1915 by Albert Einstein (Einstein, 1915, 1918) in his theory of general relativity (GR). They are perturbations of the space-time which propagate at the speed of light and are produced by changes in the mass quadrupole moment of a system, Q_{ij}. The amplitude of GWs, h_{ij}, can be approximately written as (Blanchet and Damour, 1989),

$$h_{i,j} \;\approx\; \frac{2G}{c^4 r} P_{ijkm}(\boldsymbol{n}) \frac{\mathrm{d}^2 Q_{km}}{\mathrm{d}t^2}, \tag{1.1}$$

where r is the distance to the source, $\boldsymbol{n}$ the unit vector in the direction from the source to the observer and $P_{ijkm}(\boldsymbol{n})$ the projection tensor, defined as,

$$P_{ijkm}(\boldsymbol{n}) \;=\; (\delta_{ik} - n_i n_k)(\delta_{jm} - n_j n_m) - \frac{1}{2}(\delta_{ij} - n_i n_j)(\delta_{km} - n_k n_m). \tag{1.2}$$

The factor $2G/c^4 r$ in equation (1.1), where c is the speed of light and G the gravitational constant, is responsible for the weakness of GW radiation, and thus the great challenges of their detection.

The existence of GWs was indirectly proven by the long term observations of the Hulse-Taylor binary pulsar (PSR1913+16) discovered in 1975 (Hulse and Taylor, 1975), whose orbit is shrinking due to GW emission, as predicted by GR (Taylor and Weisberg, 1989; Weisberg and Taylor, 2005). Nevertheless, it was not until a

[1]Binary BHs do not eject any material, produce any neutrinos nor trigger any EM emission, except possibly in very rare circumstances, when matter is present in the close vicinity of the coalescing binary BHs. Therefore they are not relevant for the purpose of this work.

hundred years after Einstein's postulation that GW could be detected for the first time. In 2015, the two detectors LIGO-Livingston and LIGO-Hanford (both in the USA) registered the first GW signal produced by a binary BH merger (Abbott et al., 2016b).

The instruments employed for the detection of GWs are high-precision laser interferometers (bottom-left picture in figure 1.2), capable of detecting strains of up to $\sim 10^{-23}$ due to the passage of GWs (Martynov et al., 2016) (or equivalently, to detect changes in the distance traversed by the laser of $\sim 10^{-21}$ m LIGO). Besides the two LIGO GW detectors which detected the first GW signal from two merging BHs, a third GW detector in Italy, VIRGO, started observing in 2017, providing much better sky localization of observed events via triangulation. Up to date, GWs from several BH-BH binaries (Abbott et al., 2016b,c, 2017c,d,e) and one NS-NS binary (GW170817, bottom-right graphic in figure 1.2) (Abbott et al., 2017f) have been detected by the ground-based interferometers.

These detectors are most sensitive to GW frequencies between $\sim$ 10 and $\sim$ 10000 Hz (Martynov et al., 2016). At such frequencies, the inspiral of two COs in a binary prior to merger present one of the loudest GW sources in the local universe. For the interferometers, once operating at design sensitivity, NS-NS mergers will be detectable up to $\sim$ 200 Mpc while NS-BH mergers up to a distance $\sim 2-3$ times larger (Abadie et al., 2010). Based on the observational evidence on NS-NS binaries, the detection rate of NS-NS mergers is predicted to be $3-18$ events per year (Kim et al., 2015), while the NS-BH merger rate cannot be constrained empirically due to the lack of observations. Alternatively, population-synthesis calculations[2] predict a similar NS-NS merger detection rate of ~ 3 events per year, and a comparable rate for NS-BH mergers (see e.g. Dominik et al. 2015). However, both the observational and population synthesis predicted rates are subject to multiple uncertainties, such as the low number statistics of observed systems or the uncertainties in the modelling of binary stellar evolution (S.N. Shore 1992, see e.g. Tauris et al. 2015; Dominik et al. 2015), respectively.

The long delay time expected between the formation of the two NSs and their merger, leads to a reduction of the eccentricity in the orbit due to GW emission, becoming quasi circular at the time of the merger. All the presented rate estimates neglect the contributions from CO binaries evolving in dense stellar environments, such as globular clusters, where gravitational interactions with neighbouring stars can lead the system to merge with highly eccentric orbits. Although eccentric mergers are expected to be rare ($\sim$ 1 per cent of the total CO merger rate), they could be of relevance due to the large amount of material ejected during the merger (East et al., 2012; Samsing et al., 2014).

[2]Population synthesis calculations are simulations in which a population of stars, including binaries and their interactions, is evolved by means of simplified stellar evolution track models.

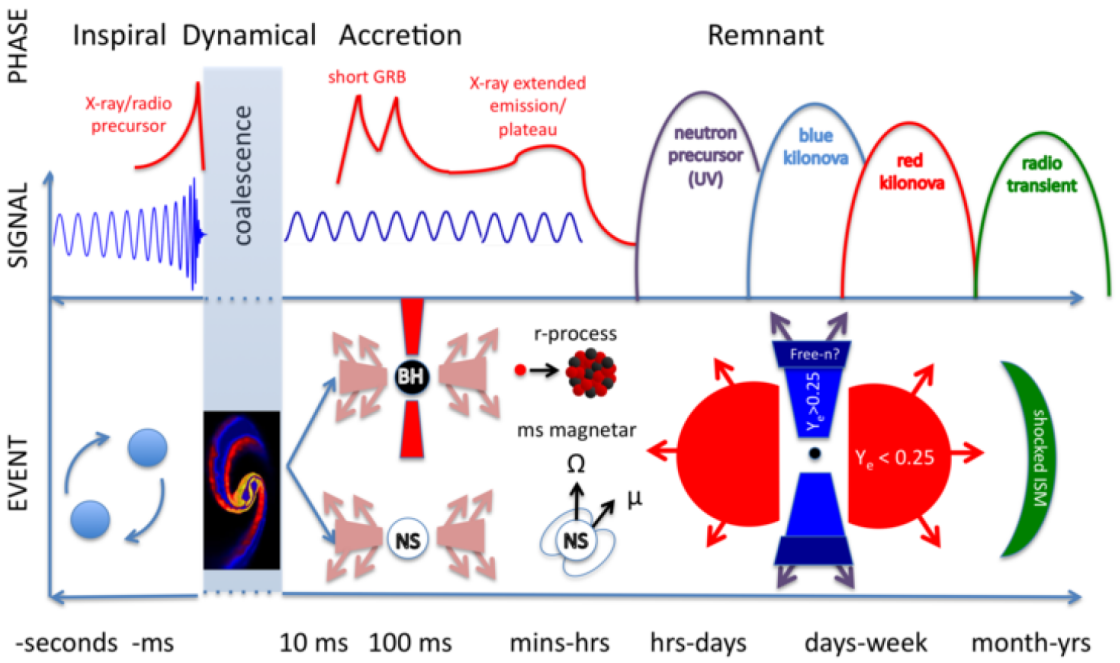

Figure 1.1.: Schematic illustration of the different phases of a neutron-star merger with its associated observable signals, either in gravitational waves or electromagnetic radiation. Credit: Fernández and Metzger (2016b), final version published in Fernández and Metzger (2016a).

1.1.2. The merger phase

Due to the extreme compactness of NSs (and BHs), the two COs in a binary evolve as gravitational point-sources until they reach very close orbits. Once in the tidal field of the companion, the dynamics are dominated by the mass ratio between the two COs (and the spin of the BH). In equal-mass (symmetric) NS-NS mergers on the one hand, the two NSs deform in tear-like shapes before merging in a violent collision, expelling material from the collision interface at high velocities, some of which later settles as a disc around the remnant. On the other hand, in asymmetric NS-NS binaries, the lighter NS is disrupted in the tidal field of its companion, expanding in a tidal tail which winds around the resulting central object like a spiral arm. Some of the material from this tail becomes unbound and the rest settles as an accretion disc around the merger remnant. The merger of two NSs can result in the direct collapse to a BH of the central object, the delayed collapse of a metastable hyper-massive NS (HMNS) or a stable NS (see section 4.1 for details). In NS-BH mergers, the NS is disrupted as in asymmetric NS-NS mergers if the masses are not too dissimilar or the BH is spinning rapidly. In the case of a slowly spinning BH or much higher BH mass, the NS is instead swallowed as a whole by the BH. In either case, the final remnant is always a BH, possibly surrounded for some time by a torus of NS matter

if the NS was disrupted (see e.g. Kyutoku et al. 2013; Bauswein et al. 2014a; Just et al. 2015a).

The fate of the central object in NS-NS mergers depends primarily on the EoS of NS matter and the total binary mass. Both thermal pressure and rotational support can delay the collapse of the HMNS, but ultimately if the total remnant mass is larger than the maximum NS mass allowed by the EoS, the star will collapse. The lifetime of the remnant is of special importance for the post-merger (*ringdown*) GW signal signal, produced mainly by quadrupolar oscillation modes excited in the HMNS. Furthermore, the fate of the central object will influence the remnant phase of the merger, as will be discussed below.

The amount of material unbound during the merger (also known as dynamical ejecta), as well as its origin, depends on the binary mass ratio and compactness (mass-radius ratio) of the NSs, determined by the EoS (see appendix E). Dynamical ejecta masses can range from 10^{-4} to 10^{-2} times the mass of the Sun ($M_\odot$) in NS-NS mergers, or up to some $\sim 0.1\ M_\odot$ in NS-BH mergers. In NS-NS mergers most of the ejecta originates from the collision interface, with larger contributions of tidally ejected material in asymmetric systems (see section 4.1). In NS-BH mergers all the dynamical ejecta comes from the expanding tidal tail. However, not all of the material ejected in the collision or in tidal tails gets unbound. Up to $\sim 0.3\ M_\odot$ of NS material settles in an accretion disc around the central object ~ 10 ms after the collision.

The dynamical ejecta from NS-NS/BH mergers reaches typical velocities ranging from 0.1 to 0.3 times the speed of light, regardless of its origin (shock or tidal). However, the exact composition of the ejecta remains a vivid topic of debate amongst astrophysicists. The electron fraction, Y_e, which is the number of electrons per nucleon (equivalent to the ratio of protons to nucleons in charge-neutral matter), is the main quantity determining the ejecta composition. As will be discussed below, Y_e governs the distribution of elements synthesized in the expanding ejecta.

At the high temperatures ($\sim 10^{11}$ K) and densities reached during a NS-NS merger, copious amounts of neutrinos are produced, amongst others, via β-interactions,

$$p + e^- \leftrightarrow n + \nu_e \tag{1.3}$$

$$n + e^+ \leftrightarrow p + \bar{\nu}_e \tag{1.4}$$

changing Y_e in the NS material. The shock-heated material ejected from the collision interface reaches higher temperatures than tidal ejecta, and hence is more influenced by the neutrino interactions, which scale with matter temperature. Due to the intrinsic low Y_e ($\sim 2 \cdot 10^{-2}$, which means high neutron content) of NSs, electron antineutrino ($\bar{\nu}_e$) emission dominates (equation 1.4), and the ejecta Y_e increases with respect to that of cold NS matter. Moreover, the exposure of the dynamical ejecta to the neutrino fluxes emitted by the merger remnant further influences the plasma composition. Because of the geometry of the merger remnant, material located in the polar directions is more strongly irradiated by neutrinos, thus tentatively raising its Y_e further (see *remnant* phase in figure 1.1). However, in NS-BH mergers the

temperature of the disrupted NS remains lower and the central object (BH) does not emit neutrinos, hence deeming the impact of neutrinos less important in comparison to NS-NS mergers.

As will be discussed below, the exact extent to which neutrino effects alter the composition of the dynamical ejecta remains a subject of study by the merger community, specifically in the context of numerical simulations (e.g. Wanajo et al. 2014; Foucart et al. 2016; Radice 2017).

1.1.3. The merger remnant: accretion phase and gamma ray bursts

On longer time-scales, from tens of milliseconds to seconds (see *Accretion* phase in figure 1.1), the hot matter that settled into the torus cools via neutrino emission and accretes onto the central object. The re-absorption of neutrinos emitted by the disc, helps unbind some amounts of torus material ($\lesssim 10^{-3}\ M_{\odot}$), especially in the cases where the central object is a HMNS, which also contributes to the neutrino flux (Perego et al., 2014b; Richers et al., 2015). However, a larger amount of mass is ejected in the post-merger phase due to the outward transport of angular momentum in the torus induced by magnetic viscosity, reaching amounts comparable to the dynamical ejecta (e.g. Fernández and Metzger 2013; Just et al. 2015a). As we mentioned earlier, the initial neutron richness of NS matter translates into a dominant emission of $\bar{\nu}_e$, thus pushing the mean Y_e of the ejecta to $\sim 0.2 - -0.3$.

Gamma ray bursts (GRB) are flashes of collimated γ-radiation of extra-galactic origin, amongst which astrophysics have identified two distinct populations, based on their duration and spectral properties. Those lasting more than 2 seconds with softer (less energetic, lower frequencies) spectra are long GRBs (lGRB) and have been associated with very energetic SNe (see Della Valle 2006 and references therein). In contrast, NS-NS/BH mergers have been suggested as the engine behind the shorter ones with harder spectra (sGRB) (Paczynski, 1986). The standard scenario describing sGRBs assumes the collapse of the central object into a BH surrounded by a torus of NS matter, which by its own energy release together with energy tapped from the BH would launch a collimated beam (jet) in the polar directions. Alternatively, the formation of an extremely strongly magnetized NS, known as magnetar, could also provide the necessary energy output by means of its magnetic field (e.g. Eichler et al. 1989; Blandford and Znajek 1977; Paschalidis et al. 2015; Just et al. 2016; Ruiz et al. 2016; Kiuchi et al. 2015).

In the case of evenet GW170817, a low intensity sGRB was observed 1.7 seconds after the GW detection of the NS merger at a coincident location (top panels of figure 1.2) (Margutti et al., 2017; Fong et al., 2017). Although this observation shows that NS mergers can trigger γ-ray emission, the interpretation of the signal remains disputed. The initial conclusion in the detection papers, argued that the low intensity of the burst was explained by an observation of the jet off-axis. However, other groups interpret the observation as a *chocked* jet, i.e. a jet that is not energetic

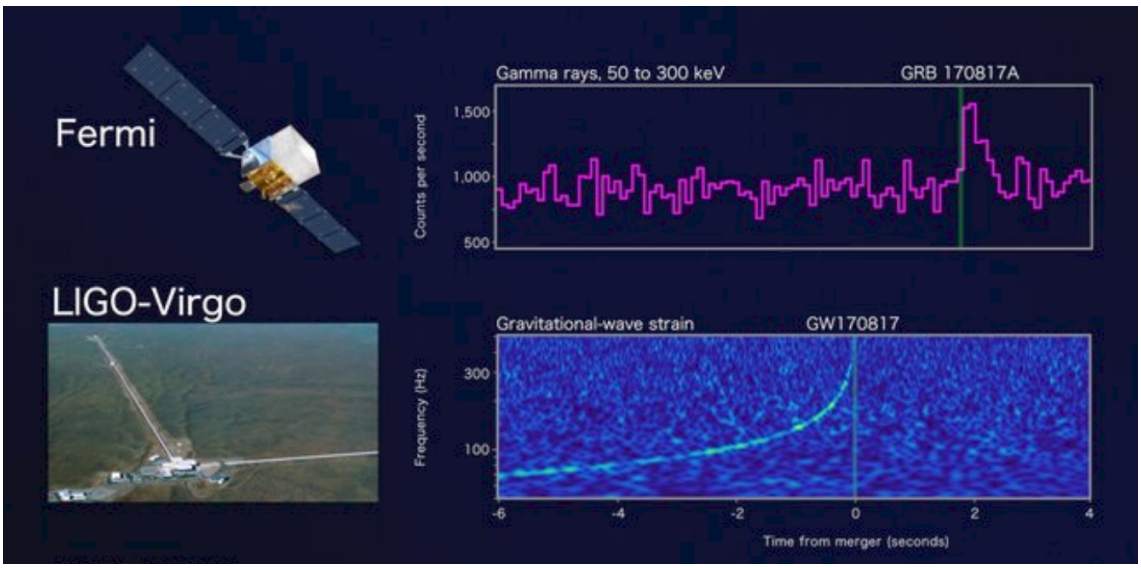

Figure 1.2.: *Top:* Picture of Fermi γ-ray space telescope and the detection of a short gamma ray burst ($\sim$ 1 s) shortly after the neutron-star merger event (GW170817) and compatible with the same sky location. *Bottom:* Picture of the VIRGO gravitational wave detector and the detection of gravitational waves from the neutron-star merger GW170817. The graphics shows the signal observed by the LIGO-Livingston gravitational wave detector, where one can clearly see the increase of the gravitational wave frequency as the neutron stars spiral towards each other. Credit: NASA's Goddard Space Flight Center, Caltech/MIT/LIGO Lab and ESA

enough to pierce through the material surrounding the central object (Kasliwal et al., 2017; Gottlieb et al., 2018). Future observations of sGRB associated with GW events will be necessary to understand the jet mechanism and to estimate the chances of the jet to break through the merger debris.

In a fair fraction of cases, extended X-ray emission has been observed following a sGRB for up to a few hours (Norris and Bonnell, 2006; Fong et al., 2015). Although its origin is not yet clear, the two leading explanations for the engine behind the signal are loosely bound material falling back onto the central object (e.g. Rosswog 2007; Lee et al. 2009) or a rapidly spinning magnetar as a merger remnant (Gompertz et al., 2013).

1.1.4. The unbound material: nucleosynthesis and electromagnetic emission

Neutron-rich elements heavier than Zinc (atomic number $Z = 30$) are expected to be synthesized by successive neutron captures by seed nuclei in fast-expanding

material with neutron excess (e.g. Sneden et al. 2008). Two distinct processes are differentiated depending on the comparatison of the neutron-capture rate ($R_{\rm n}$) and the β-decay rate (R_β): the slow neutron-capture process or *s-process* ($R_{\rm n} \ll R_\beta$), and the rapid neutron-capture process or *r-process* ($R_{\rm n} \gg R_\beta$) (Burbidge et al., 1957). The site of the s-process has been identified to be intermediate mass stars (1.3–8 $M_\odot$, e.g. Herwig 2005), but the source of r-process material has remained uncertain for long. The observation of solar-like r-process abundances in metal-poor[3] stars in the Milky Way (e.g. Sneden et al. 2008), favours the scenario of an r-process site with robust prediction of the heaviest elements.

SNe were the prime candidates for producing suitable conditions for the r-process, but more and more sophisticated multidimensional simulations have failed to demonstrate sufficiently neutron-rich environments in the SN ejecta (e.g. Hüdepohl et al. 2010; Roberts et al. 2012; Martínez-Pinedo et al. 2012). An alternative candidate was already proposed in the 1970's: provided NS-NS/BH binaries could unbind enough material during their merger, the intrinsic neutron richness of decompressed NS matter could provide ideal conditions for the r-process (Lattimer and Schramm, 1974).

Nucleosynthesis calculations[4] for the ejecta obtained by numerical simulations of NS-NS/BH mergers yield a robust solar abundance pattern for elements with atomic mass numbers $A \gtrsim 140$ (e.g. Goriely et al. 2011; Korobkin et al. 2012; Bauswein et al. 2013, 2014a; Just et al. 2015a, see left panel of figure 1.3). These abundances are rather insensitive to the binary parameters (NS masses, spins and EoS), partially due to *fission recycling*: the high neutron flux allows the formation of very massive isotopes which undergo nuclear fission, providing new seed nuclei to capture more neutrons, closing the cycle. Moreover, Just et al. (2015a) showed, that the material unbound during the post-merger phase contributes to the production of most of the lower-mass ($90 \lesssim A \lesssim 140$) r-process elements (see right panel of figure 1.3).

In general, material with $Y_e \lesssim 0.2$ produces heavy r-process elements ($A \gtrsim 140$), while in less neutron rich material, $0.2 \lesssim Y_e \lesssim 0.4$, lighter r-process nuclei are synthesized ($90 \lesssim A \lesssim 140$). As mentioned previously, neutrino interactions have a significant impact on the Y_e of the dynamical ejecta, changing the amount of available free neutrons, and hence the nucleosynthetic yields (Just et al., 2015a; Sekiguchi et al., 2015; Goriely et al., 2015; Radice et al., 2016; Wu et al., 2016; Lippuner et al., 2017; Martin et al., 2018). Some groups find almost complete solar r-process abundances ($A \gtrsim 90$) in the dynamical ejecta of NS-NS mergers when including neutrino effects (e.g. Wanajo et al. 2014; Sekiguchi et al. 2015), while others can only reproduce the heavy r-process distribution ($A \gtrsim 140$, e.g. Radice et al. 2016). These discrepancies are linked to the different treatments of neutrino physics employed in the different numerical codes, illustrating the need for improvement in this regard (see Thielemann et al. 2017 for a recent review on

[3]With low mass fraction of non-hydrogen, non-helium elements.

[4]Nucleosynthesis calculations compute the elements synthesized under defined thermodynamical conditions by employing a network of nuclear reactions.

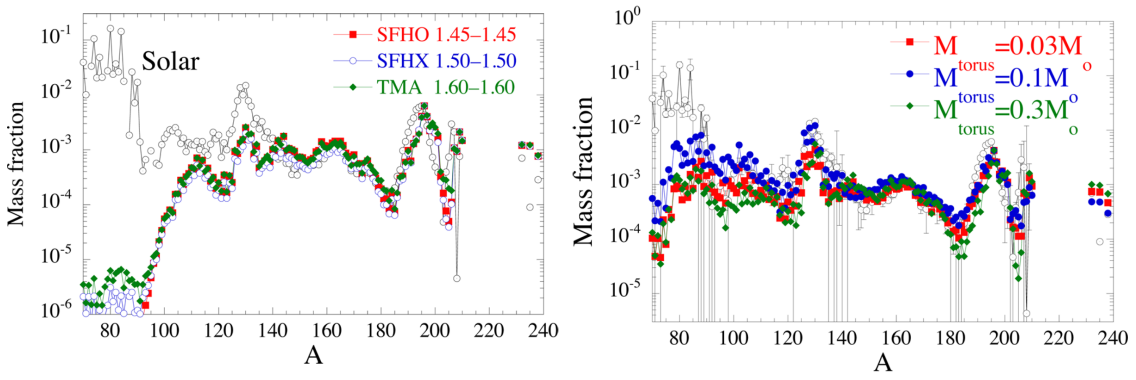

Figure 1.3.: *Left:* Mass fractions of the elements synthesised in the expanding material dynamically ejected from three equal-mass neutron-star merger simulations that employ different equations of state of neutron-star matter. The empty circles denote the element mass fractions observed in the Solar System. *Right:* Elemental yields formed in the combined ejecta from numerical simulations of neutron-star mergers and post-merger black hole-torus remnants with different disc masses. Both figures are originally from Just et al. (2015a) (figures 11 and 19 in the original publication).

r-process production in NS-NS/BH mergers).

The freshly synthesized elements in NS-NS/BH merger ejecta decay radioactively, powering an EM signal in the optical (wavelengths of 400–780 nm) and/or near infrared (780–1500 nm) bands (Li and Paczyński, 1998), known as kilonova[5] (Metzger et al., 2010). The colour and peak time, i.e. the time of maximum luminosity (brightness) when the expanding medium becomes transparent for radiation to escape, of the EM signal depend on the synthesized elements. Heavy r-process elements, particularly lanthanides ($58 \leq Z \leq 71$) and actinides ($89 \leq Z \leq 102$), are highly opaque to optical EM radiation due to their complex valence electron structure (open f-shell). The vast number of available electron bound-bound transitions effectively translates into the atom absorbing photons in a semi continuous energy range (e.g. Kasen et al. 2013). On the contrary, lighter r-process elements are more transparent to radiation of the same wavelengths.

If the ejecta are dominated by heavy r-process elements, these high lanthanide opacities[6] will delay the peak time of the kilonova up to $\sim$ 10 days after the merger, as the expanding neutron-rich material will only become transparent at low densities. Additionally, the temperature of the ejecta at such late peak time will be low ($\sim$ 1000 K), thus radiating in the near infrared. On the contrary, if some component of the merger ejecta has such an elevated Y_e that no significant amount of heavy r-process

[5]Or macronova.

[6]Opacities are defined as the inverse of the mean free path, which is the mean distance traversed by photons between interactions.

elements is synthesized, the kilonova signal could peak at times as early as a day after the merger. Conversely, this material would remain hotter at peak time, thus radiating in optical (*blue*) wavelengths (e.g. Kulkarni 2005; Metzger et al. 2010; Kasen et al. 2015; Fernández et al. 2017; Hotokezaka et al. 2016; Barnes et al. 2016; Tanaka et al. 2018). As figure 1.1 depicts, the material ejected in the polar directions in a NS-NS merger is more likely to be less neutron rich due to the neutrino irradiation by the torus and HMNS. Again, this highlights the need for a reliable treatment of the neutrino physiscs in NS-NS mergers to better understand the composition of the material ejected in different directions and for different binary configurations.

It has also been proposed that an ultraviolet ($10 \sim 400$ nm) signal could precede the kilonova, peaking a few hours after the merger and powered by the β-decay of fast expanding free neutrons, which avoid being captured by nuclei (Metzger et al., 2015). Finally, months or years after the merger, the expanding ejected material can collide with the surrounding interstellar medium, launching a shock wave and powering a radio ($>$ 1 dm) signal (Nakar and Piran, 2011). All the predicted EM signals associated with a NS-NS/BH merger are summarized in figure 1.1 (see Fernández and Metzger 2016a; Metzger 2017 for recent reviews).

In the aftermath of the NS merger GW event GW170817, several ground-based and space telescopes detected an associated EM signal in optical/infrared wavelengths (Abbott et al., 2017a; Soares-Santos et al., 2017; Cowperthwaite et al., 2017; Nicholl et al., 2017; Chornock et al., 2017; Alexander et al., 2017; Shappee et al., 2017; Abbott et al., 2017b) (see figure 1.4). Based on the observed colour, peak times and spectral features[7], this signal has been identified as a kilonova, thus providing strong evidence of the presence of r-process elements in the merger ejecta (Smartt et al., 2017; Chornock et al., 2017; Pian et al., 2017; Shappee et al., 2017). Analysis of the obtained data at different wavelengths suggests a total of 0.03-0.05 $M_{\odot}$ of rapidly-expanding ejecta, composed of neutron rich material. However, the exact distribution and elemental composition of the ejecta powering the kilonova has started a heated debate amongst astrophysicists. Some groups fit the observed EM signal assuming only one ejecta component (Smartt et al., 2017), while other groups have suggested the need of two (Cowperthwaite et al., 2017; Kasen et al., 2017) or even three (Perego et al., 2017) distinct ejecta components to explain the data. All these studies are based on simple models describing the evolution of the signal (like Arnett 1982). However, to understand all the details of the kilonova evolution, full radiative transfer simulations are required (Tanaka et al., 2017). Unfortunately, the opacities of r-process elements required for such calculations are poorly constrained due to the lack of experimental data (e.g. Tanaka et al. 2018), and the obtained results are sensitive to the initial ejecta conditions, which are quite uncertain. In order to improve the understanding of future detections, it is indispensable to rely on accurate numerical simulations with all the relevant physics, including neutrinos, taken into account and a complete survey of initial conditions.

[7]Emission lines due to electron bound-bound transitions.

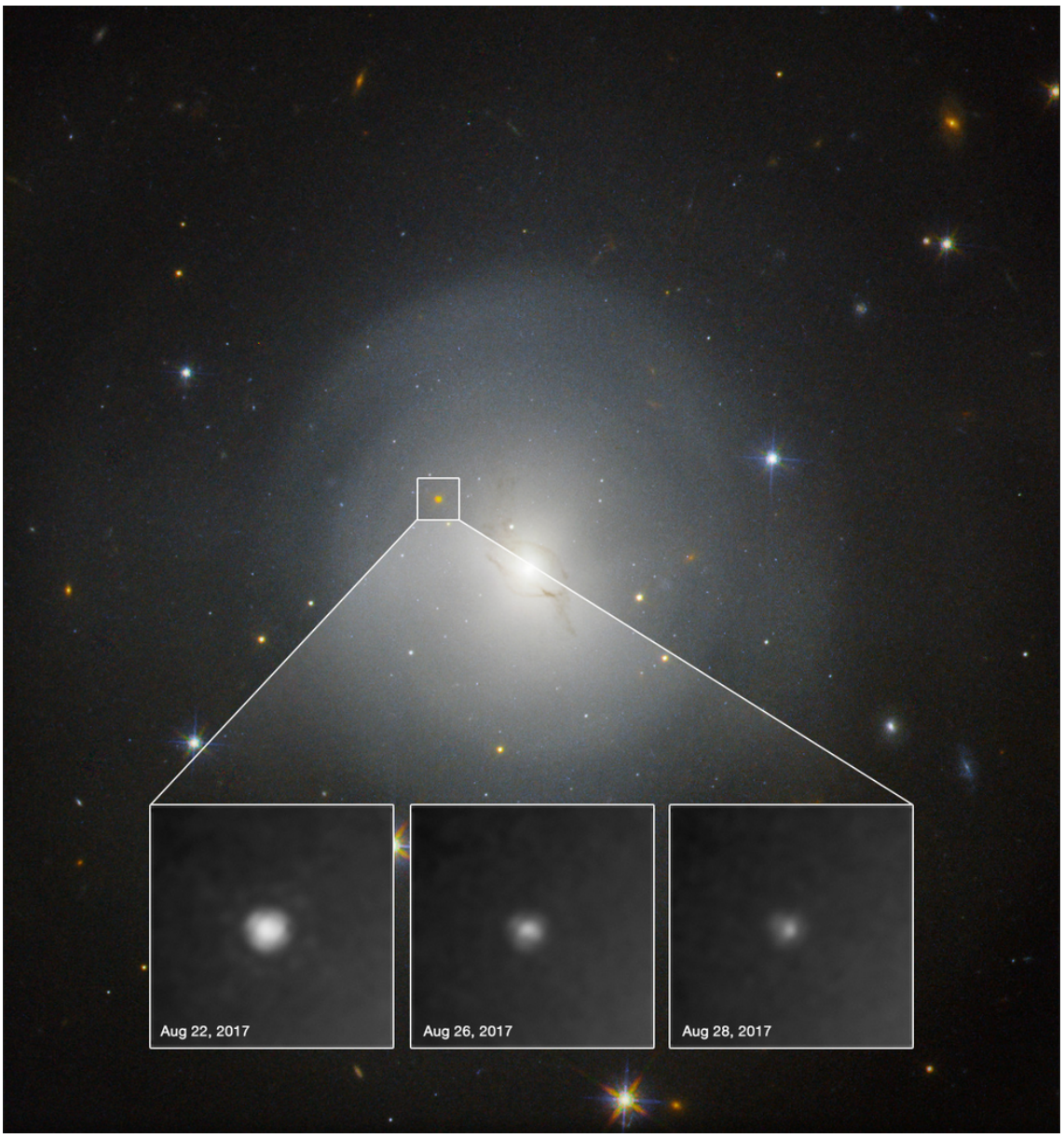

Figure 1.4.: Picture of the observed kilonova associated to the NS-NS merger GW detection in its host galaxy. The image was taken by Hubble Space Telescope and the three insets show three observations of the source at different times in the course of six days, showing its gradual fading. Credit: ESA/Hubble.

1.2. Numerical simulations of compact object mergers including neutrino effects

NS-NS/BH merger simulations have been successfully performed by different groups with varying degrees of accuracy and physics included, from (post-)Newtonian gravity[8] (e.g. Shibata et al. 1992; Xing et al. 1994; Rasio and Shapiro 1994; Davies et al. 1994; Ruffert et al. 1996) to GR (e.g. Faber et al. 2004; Bauswein et al. 2014b; Lehner et al. 2016a; Dietrich et al. 2017; Fernández et al. 2017; Radice 2017; Ciolfi et al. 2017; Kyutoku et al. 2018). The impact of NS or BH spins (Kastaun et al., 2013; Kastaun and Galeazzi, 2015; Dietrich et al., 2017), eccentric orbits (Radice et al., 2016), magnetic fields (Lehner et al., 2016a; Ciolfi et al., 2017), or neutrino interactions (Ruffert et al., 1996; Rosswog et al., 2013; Radice et al., 2016; Lehner et al., 2016a; Fernández et al., 2017; Kyutoku et al., 2018) have also been studied, constrained by the numerical resources available. For recent reviews on numerical simulations of NS-NS and NS-BH mergers, we refer the reader to Faber and Rasio (2012) and Rosswog (2015a); and Shibata and Taniguchi (2011), respectively.

As we have pointed out during this introduction, neutrinos are a crucial ingredient in NS-NS/BH merger simulations, especially in order to understand the nature of the matter outflows and their related observables. Although they are dynamically not of primary importance, neutrinos can have a noticeable impact on the amount of unbound material, both in the merger and post-merger phases. However, the most significant contribution of neutrinos is in shaping the composition of the NSs and of the ejected matter by governing the evolution of the neutron-to-proton ratio.

The neutrino phase-space distribution function evolves following the Boltzmann transport equation. This constitutes a six-dimensional (three spacial directions and three more in momentum space), time-dependent problem for each neutrino species, which is currently impossible to solve without some approximation to reduce its dimensionality (e.g. Lindquist 1966). Therefore, numerous schemes of varying complexity and accuracy have been developed to approximate the impact of neutrinos in numerical simulations.

In the context of NS mergers, truncated moment schemes are the most sophisticated approximations successfully used. In those schemes, the Boltzman transport equation is simplified by introducing a series of so-called moments, for which the neutrino phase-space distribution function multiplied with increasing powers of the unit vector in the neutrino momentum direction is integrated over two momentum components: the angles of neutrino propagation, thus reducing its dimensionality. This leaves an infinite set of equations which depend only on the three spatial directions and the neutrino energies. In order to approximately solve the system, the series of moments needs to be truncated at a certain order by closing the set of equations with a closure relation, which generally expresses the highest employed moment as a function of all the previous ones.

The so-called *M1* schemes (e.g. Shibata et al. 2011; O'Connor 2015) truncate

[8]Including higher order gravitational effects such as GWs.

the series of moments after the first-order, evolving the neutrino energy density (zeroth order) and the neutrino flux density (first order), and closing the system with an analytical relation between the two. Versions of these schemes exist in an energy dependent form (e.g. Just et al. 2015b), or in a *grey* form, where the energy dependence has been removed by employing energy integrated/averaged quantities in the evolution equations (e.g. Foucart et al. 2015). Despite their popularity for describing the transport of neutrinos, M1 schemes are computationally very expensive and cannot handle properly the evolution of two neutrino beams crossing each other because of the non-linearity of the closure relation. Instead of following their own trajectories, the two crossing beams merge and from a single beam in the average direction of propagation of the two initial beams. This undesirable effect can have a detrimental impact on the merger ejecta escaping in the polar directions, "artificially" altering its composition.

Leakage schemes are a very popular and computationally simple approximation for the treatment of neutrino effects in NS-NS/BH merger simulations. Instead of solving the Boltzman transport equation or its moment equations, these schemes compute local effective sources for neutrino energy and lepton-number losses by means of an interpolation between neutrino diffusion rates (in opaque, optically thick conditions) and neutrino production rates (in a transparent, optically thin medium).

Neutrino leakage schemes were introduced in the context of Newtonian NS-NS merger simulations by Ruffert et al. (1996, 1997); Ruffert and Janka (1999, 2001) and Rosswog and Liebendörfer (2003); Rosswog et al. (2003); Korobkin et al. (2012); Rosswog et al. (2013); Rosswog (2013). More recently, versions of such schemes including gravitational redshift effects (Sekiguchi, 2010; O'Connor and Ott, 2010; Galeazzi et al., 2013) have been used in many relativistic merger simulations (Sekiguchi et al., 2011a,b; Kiuchi et al., 2012; Deaton et al., 2013; Foucart et al., 2014, 2017; Neilsen et al., 2014; Palenzuela et al., 2015; Lehner et al., 2016b,a; Bernuzzi et al., 2016), as well as longer-term evolution calculations of post-merger remnants, including HMNSs (Metzger and Fernández, 2014; Lippuner et al., 2017) or BH-torus systems (Shibata et al., 2007; Fernández et al., 2015a,b).

Nevertheless, traditional leakage schemes only reproduce one aspect of neutrino transport, namely neutrino energy and lepton-number losses. Additionally, the "standard" descriptions of diffusion rely on a simple dimensional analysis which results in an overestimation of the production of neutrinos in the semi-transparent region, while at the same time failing to drain the interior of the star (see comparison in appendix A). Other relevant effects, such as the impact of neutrinos trapped and in equilibrium within the fluid in optically thick conditions or the re-absorption of neutrinos by semitransparent material, should be taken into account as well. Some more sophisticated leakage variants incorporate some of these elements by different means, albeit with some restrictions.

Perego et al. (2016) developed an Advanced Spectral (energy-dependent) Leakage (ASL) scheme which includes the impact of neutrinos in equilibrium with the medium parametrized using time-scale arguments. Additionally, they employ com-

plex propagation paths to re-map the local neutrino emission to the star's surface, from where neutrinos radiate isotropically and are re-absorbed by optically thin matter (see Perego et al. 2014a,b, 2016). This scheme was tested against a Boltzmann transport solver in one and two dimensional simulations of core-collapse SNe, reporting good agreement in the comparison (Perego et al., 2016). However, even though qualitative agreement is achieved, local discrepancies, reaching up to a factor two, can be observed in some cases. Furthermore, the ASL code relies on three parameters calibrated for the tested scenario (core-collapse SNe), with no guarantee of their performance on NS-NS/BH mergers. The current limitations in the understanding of the impact of neutrinos in NS-NS/BH mergers does not allow for a sensible calibration *a priori* of these parameters, thus rendering this approach unsatisfactory.

Other groups have tried to exploit the advantages of different neutrino treatments by employing hybrid methods between leakage and moment schemes. Radice et al. (2016); Radice (2017); Radice et al. (2017, 2018); Zappa et al. (2018) use a standard relativistic leakage method (Galeazzi et al., 2013) to treat local neutrino losses. In order to approximately calculate neutrino re-absorption, they evolve the zeroth moment equation (what they call *M0*) along radial rays using the leakage source term instead of the local production rate and assume freely streaming neutrinos, where the number flux density is equal to the neutrino number density times the speed of light. The M0 equation is solved on every hydrodynamical time-step, together with an evolution equation for the neutrino mean energy. This scheme does not take equilibration of neutrinos and matter into account.

Similarly, Sekiguchi et al. (2012, 2015, 2016); Fujibayashi et al. (2017); Shibata et al. (2017); Kyutoku et al. (2018) also calculate local neutrino losses by means of a leakage method (Sekiguchi, 2010; Sekiguchi et al., 2012) and use a moment scheme to estimate the neutrino re-absorption. However, instead of the M0 approach they evolve the zeroth and first moments of the Boltzmann equation with an analytical closure (M1), using the leakage source term instead of the local neutrino production as well[9]. Furthermore, they do assume a component of neutrinos trapped within the fluid in optically thick conditions, including an ansatz for neutrino equilibration with a β-equilibrium limiter (Sekiguchi, 2010; Sekiguchi et al., 2012). This limiter ensures that the local neutrino fraction does not exceed the one in β-equilibrium, and distinguishes the trapping from the free-streaming neutrino component.

There are only a few comparisons in the literature between different neutrino schemes. Foucart et al. (2015, 2016) reports considerable differences between the results obtained with their grey M1 code (SpEC) and with a "conventional" leakage scheme in the context of NS-NS merger and post-merger simulations. More precisely, they find a discrepancy of up to a factor two in the neutrino luminosities and the electron fraction of the ejected material, possibly due to the lack of neutrino re-

[9]This is our interpretation of the method loosely described in the original papers (Sekiguchi et al., 2016; Fujibayashi et al., 2017; Kyutoku et al., 2018), which agrees with the reading by Radice et al. (2016). We apologize for any misunderstanding of the actual approach.

absorption in the leakage model. In contrast, with the exception of ASL, there are no published test comparisons between any of the described hybrid leakage schemes and more sophisticated transport solutions. Therefore, it is not possible to ascertain the accuracy of such schemes.

1.3. Goals and structure of the thesis

The GW detection in 2017 of a NS-NS merger and its associated EM counterparts have highlighted the need to develop more sophisticated numerical models in order to understand these and also future observations. As discussed above, one of the most crucial ingredients in NS-NS/BH merger simulations is the description of neutrino interactions, which drive the chemical composition of the ejected material, and thus characterize the signal powered by the radioactive decay of heavy neutron-rich isotopes.

However, only a few computational approaches described in the literature include neutrino treatments, and they are either computationally expensive or treat the physics very approximately with a variety of shortcomings (see section 1.2). The chief aim of this work is to provide a code capable of treating neutrino physics in NS-NS/BH mergers at a moderate computational cost, yet capturing all the essential neutrino effects with sufficient accuracy. Such a code will allow for the calculation of large sets of merger simulations, needed to explore the big variety of initial conditions that describes NS-NS/BH binaries (system masses and mass ratios, spins, orbital parameters, EoS). Leakage schemes provide the perfect basis for such a project, with their algorithmic simplicity and efficient performance. Furthermore, the typically short dynamical time-scales of the merger phase, i.e. the fluid configuration evolving faster than the transport of neutrinos, render this approach a successful alternative to more sophisticated transport schemes.

With this in mind, and motivated by all the shortcomings of existing schemes described in section 1.2, I introduce a new implementation of an improved leakage method in the context of NS-NS/BH mergers: ILEAS (Improved Leakage-Equilibration-Absorption Scheme). In the first place, ILEAS includes a new formulation of the escape time-scale of neutrinos by using a diffusion description, which improves on the "conventional" leakage prescription. Additionally, the fact that neutrinos remain trapped and in β-equilibrium with the fluid in the optically thick regime is accounted for by our novel *equilibration* treatment. Finally, the effects of neutrino re-absorption in optically thin conditions are accounted for by a ray-tracing algorithm, reproducing transport results in the optically thin limit.

Each constituting block of our scheme is designed to mimic the physical behaviour of neutrino transport in different regimes, avoiding the use of *ad hoc* parameters when possible. In contrast to the intransparence of some hybrid schemes, where the physical notion of the different components is not clearly defined or demonstrated, we motivate our choices with physics-based arguments, which we back up with results obtained in relevant astrophysical test-scenarios. Unlike other improved

leakage schemes reported in the literature, ILEAS includes a description of neutrino interactions in optically thick conditions consistent with neutrino diffusion and trapping. Moreover, the raylike nature of our absorption scheme proves advantageous to trace the intrinsic three-dimensional geometry of NS-NS mergers.

We examine the performance of our new scheme in relevant astrophysical scenarios, such as newly born hot proto-NSs (PNS) and BH-torus systems, and compare the results to the ones obtained by more sophisticated neutrino transport treatments. This two scenarios allow us to probe all the range of possible environments for neutrino transport, from diffusion inside the optically thick PNS to neutrino irradiation and absorption in the optically thin torus. Although several neutrino schemes are employed by different groups in simulations of NS-NS/BH mergers, comparisons between different methods are scarce (Foucart et al., 2016; Perego et al., 2014b). In contrast, we provide a detailed comparison of the results obtained by ILEAS and the employed transport schemes, not only in the global neutrino properties, but also in their spatial dependence. Our comparisons show an agreement, locally and globally, to better than $\sim$15 per cent in the relevant neutrino-related quantities in all our tested scenarios.

To assess the importance of each of the modules which compose ILEAS (leakage, absorption and equilibration), we test them individually in NS-NS merger simulations with the same initial conditions, and show the consequences of neglecting some of these relevant effects.

Finally, we perform numerical simulations of NS-NS mergers with different NS masses, mass ratios and EoSs. We study the neutrino-related properties as well as the impact of neutrinos on the composition of the ejected material for the different initial configurations. Moreover, we compare the obtained results with those reported by other groups employing the same initial setups in NS-NS merger simulations with different codes. However, we point out that these comparisons face other challenges, such as the intrinsic differences in the handling of the hydrodynamical evolution of the merger, which have a considerable impact on the neutrino properties due to their high sensitivity on the matter temperature.

This thesis is organized as follows. In chapter 2 I describe the neutrino scheme developed for this work, summarize the NS merger code and explain how both are coupled. In chapter 3 I show the excellent performance of our leakage scheme by comparing our results to the ones obtained by more sophisticated treatments in the context of newly born proto-NSs (PNSs) and BH-torus systems. Chapter 4 is devoted to the impact of the neutrino physics included in our model on the merger ejecta. Additionally, I contrast our findings with similar results from other research groups. Finally, I summarize our work in chapter 5. There, the strengths of our method are also highlighted and I discuss the conclusions that can be drawn from the obtained results, concluding with the natural steps to follow in future work.

As a complimentary analysis, in appendix A I compare the performance of the leakage module of ILEAS to the "conventional" leakage schemes given in the literature. In appendix B the formulation of the neutrino interactions included in ILEAS are summarized. Then in appendix C I compare the two standard derivations of

the neutrino production rates, and how they affect the luminosity profile of a PNS. In appendix D the rendering of smoothed particle hydrodynamics (SPH) particles on a numerical grid is discussed. Ultimately, I provide some information about the different NS EoSs employed in this work in appendix E.

Throughout this thesis *cgs* units are used unless stated otherwise and in section 2.1 I use $G = c = 1$. The expression *CO merger* will be applied to refer to the merger of a NS with either a BH or a NS. Binary BH mergers produce no ejecta nor neutrino emission, and, therefore, they are irrelevant for the purpose of this work.

2. Computational model

2.1. Relativistic smoothed particle hydrodynamics in the conformal flatness approximation

To simulate the merger of two neutron stars we employ the relativistic code described in Oechslin et al. (2007); Bauswein (2010). Using a smoothed particle hydrodynamics (SPH) approach, it solves the relativistic Euler equations to calculate the hydrodynamical evolution of the system. The metric potentials are then computed on an overlaid grid by solving the Einstein equations in the conformal flatness condition. It is essential to simulate such events in the framework of general relativity, as for such extreme compactness as that of NSs, the deviations from classic Newtonian gravity are significant. Additionally, the Lagrangian formalism of SPH allows us to naturally track the evolution of the merger ejecta to arbitrary distances, without the need of tracer particles.

The SPH method was first described by Lucy (1977) and Gingold and Monaghan (1977), as a method to simulate particle ensembles, but it has been widely used in astrophysics since then. We refer to Rosswog (2015b) for a recent review on SPH, especially devoted to their application in the framework of CO mergers. The SPH formalism relies on the representation of a fluid as a set of particles of constant mass m_i, which carry their hydrodynamical properties along their trajectories. They are characterized by a kernel function, $W(|\boldsymbol{r}-\boldsymbol{r}_j|, h_j)$, which describes their spacial extent, peaking at the particle position, r_j, and modulated by the smoothing length, h. The kernel function must be normalized to unity, continuous and differentiable. We employ the commonly used spherically symmetric cubic spline kernel,

$$W(d=|\boldsymbol{r}-\boldsymbol{r}_j|, h_j) \;=\; \frac{1}{\pi h^3}\begin{cases} 1-\frac{3}{2}d^2+\frac{3}{4}d^3, & for\ 0\le d\le 1 \\ \frac{1}{4}(2-d)^3, & for\ 1<d\le 2 \\ 0, & for\ d>2 \end{cases} \tag{2.1}$$

By means of the kernel, any function A can be expressed as a smoothed average,

$$\langle A(\boldsymbol{r})\rangle \;=\; \int A(\boldsymbol{r_j}) W(|\boldsymbol{r}-\boldsymbol{r}_j|, h_j)\mathrm{d}^3 r_j. \tag{2.2}$$

Describing the fluid by means of SPH particles, the previous equation can be easily discretized as,

$$\langle A(\boldsymbol{r})\rangle \;\simeq\; \sum_j V_j A(\boldsymbol{r_j}) W(|\boldsymbol{r}-\boldsymbol{r}_j|, h_j). \tag{2.3}$$

where the particle volume, V_j, can be expressed as $V_j = m_j/\rho^*_j$, and the summation runs over neighbouring particles.

As in most hydrodynamic solvers, we define the conserved quantities: conserved rest-mass density, ρ^*, conserved specific momentum, $\hat{u}_i$, and conserved energy density, τ, as a function of their primitive counterparts, rest mass, ρ, velocity, v_i and specific internal energy, ε, via

$$\rho^* = \rho\alpha u^0\psi^6, \tag{2.4}$$

$$\hat{u}_i = Hu_i = H(v^i + \beta^i)\psi^4 u^0, \tag{2.5}$$

$$\tau = HW - \frac{P}{\rho W} - \sqrt{1 + \frac{\hat{u}_i\hat{u}_j\delta^{ij}}{\psi^4}}. \tag{2.6}$$

Here the Lorenz factor is defined as $W = \alpha u^0 = \sqrt{1 + \gamma^{ij}u_iu_j}$, with γ^{ij} being the spatial components of the metric, u^0 and u^i are the time and space components of the eigenvelocity, H represents the relativistic specific enthalpy, defined as $H = 1 + P/\rho + \varepsilon$, and δ^{ij} is the Kronecker delta. The metric potentials, α, β_i and ψ are described below (equation (2.10)). We then write the relativistic Euler equations, where we include the neutrino source terms defined in equation (2.15), $Q_{\rm tot}$, in the momentum and energy equations with the pertinent corrections, as

$$\frac{\mathrm{d}}{\mathrm{d}t}\rho^* = -\rho^*\partial_i v^i, \tag{2.7}$$

$$\begin{aligned}\frac{\mathrm{d}}{\mathrm{d}t}\hat{u}_i &= -\frac{1}{\rho^*}\alpha\psi^6\partial_i P - \alpha\hat{u}^0\partial_i\alpha + \hat{u}_j\partial_i\beta^j + \frac{2\hat{u}_k\hat{u}_k}{\psi^5\hat{u}^0}\partial_i\psi \\ &\quad + \frac{Q_{\rm tot}\alpha\hat{u}_i}{\rho HW},\end{aligned} \tag{2.8}$$

$$\begin{aligned}\frac{\mathrm{d}}{\mathrm{d}t}\tau &= -\frac{\psi^6}{\rho^*}(v^i+\beta^i)\left(1-\frac{HW}{\omega}\right)(\partial_i P) - \psi^6\frac{P}{\rho^*}\partial_i(v^i+\beta^i) \\ &\quad - 6\psi^5\frac{P}{\rho^*}(v^i+\beta^i)(\partial_i\psi) - \frac{\hat{u}_i}{\psi^4}\left(1-\frac{HW}{\omega}\right)(\partial_i\alpha) \\ &\quad + \frac{1}{\psi^4}\left(\frac{1}{HW}-\frac{1}{\omega}\right)\left[\hat{u}_i\hat{u}_j\partial_j\beta^i - \frac{1}{3}\hat{u}_i\hat{u}_i\partial_j\beta^j\right] \\ &\quad + \frac{Q_{\rm tot}\alpha}{\rho}\left[1-\frac{\hat{u}_i\hat{u}_j\delta^{ij}}{\psi^4 HW\omega}\right],\end{aligned} \tag{2.9}$$

where $\mathrm{d}/\mathrm{d}t = \partial_t + v^i\partial_i$ and $\omega = \sqrt{1 + (\hat{u}_i\hat{u}_j\delta^{ij}/\psi^4)}$. To close the system, one needs a microphysical equation of state (EoS) in the form of $f(\rho, \varepsilon, Y_e)$, representing the thermodynamics of the fluid. The Euler equations are then evolved forward in time using a 4th order Runge-Kutta (RK) integration scheme, and the primitive variables are recovered every time step by solving iteratively the definitions above. In the original version of the code, the electron fraction was simply advected with the fluid, as it included no microphysics that affected the matter composition. However, the inclusion of the neutrino leakage scheme introduces a source term for Y_e, and it

will be evolved in the RK cycle. See section 2.2 for details on the changes in the formulation due to the inclusion of weak interactions.

Adopting a 3+1 space-time decomposition and the CFC approximation for the spatial component (Wilson et al., 1996), the metric can be expressed as

$$\mathrm{d}s^2 \;=\; (-\alpha^2 \;+\; \beta_i\beta^i)\mathrm{d}t^2 \;+\; 2\beta_i\mathrm{d}x^i\mathrm{d}t \;+\; \psi^4\delta_{ij}\mathrm{d}x^i\mathrm{d}x^j, \tag{2.10}$$

where ψ is the so-called conformal factor and δ_{ij} the Kronecker delta. The metric potentials α and β, are the lapse function and the shift vector, respectively (Alcubierre, 2008). By adopting the *Maximal Slicing gauge condition*, $\partial_t K = K = 0$, the Einstein equations can be written as,

$$\triangle\psi \;=\; -2\pi\psi^5 E - \frac{1}{8}\psi^5 K_{ij}K^{ij}, \tag{2.11}$$

$$\triangle(\alpha\psi) \;=\; 2\pi\alpha\psi^5(E+2S) + \frac{7}{8}\alpha\psi^5 K_{ij}K^{ij}, \tag{2.12}$$

$$\triangle\beta^i + \frac{1}{3}\partial^i\partial_j\beta^j \;=\; 16\pi\alpha\rho W\hat{u}_i + 2\psi^{10}H^{ij}\partial_j\left(\frac{\alpha}{\psi^6}\right) \equiv S_\beta. \tag{2.13}$$

Here E and S are defined respectively as $E = \rho hW^2 - P$ and $S = \rho h(W^2-1)+3P$. The extrinsic curvature, K_{ij}, can be calculated from the metric potentials as,

$$K_{ij} \;=\; \frac{\psi^4}{2\alpha}\left(\delta_{il}\partial_j\beta^l + \delta_{jl}\partial_i\beta^l - \frac{2}{3}\delta_{ij}\partial_k\beta^k\right). \tag{2.14}$$

We discretize the Einstein equations on an overlaid 3D Cartesian grid spanning the size of the binary, and employ a multipole expansion up to second order as an outer boundary condition (Oechslin et al., 2002).

The advantage of our formulation in comparison to a full GR formulation, is that we just need to solve the initial value problem repeatedly, instead of dealing with the issues which arise from attempting to solve a set of hyperbolic evolution equations, while still capturing the essence of GR. The time evolution of the system is achieved by mapping the matter distribution evolved by the SPH module onto the grid at the end of each time-step, and then solving the elliptical metric equations (2.11,2.12 and 2.13), by iteration until convergence. The new metric potentials are subsequently mapped back to the SPH particles characterizing the space-time in which matter will evolve in the next RK step.

Since the CFC formulation does not take into account gravitational radiation, a gravitational wave back-reaction scheme needs to be included in order to be able to simulate the merger. It is done in a Post-Newtonian framework as described in Oechslin et al. (2007).

In order to obtain the initial data for our simulations, we first create two NS by solving the Tolman-Oppenheimer-Volkov (TOV) equations and put them on orbit around each other with a test angular velocity. We assume both stars to be irrotational on the basis that delay time since the last SN is enough for the NSs to

have spun down, so their angular velocity is negligible in comparison to the orbital velocity. The initial separation is chosen to ensure several orbits before the merger. We then relax the system by employing a version of our code which does not include the GW back-reaction, modifying the orbital angular velocities of the stars until a quasi-stable circular orbit is achieved. We also relax the SPH particles by means of a damping force.

The results shown in this work employed approximately 350000 particles to resolve the NS binary and 0.7 km resolution for the metric grid.

2.2. Neutrino interactions with ILEAS in CFC relativistic hydrodynamics

We present a novel neutrino leakage scheme, ILEAS, that is capable of reproducing/capturing the fundamental aspects of the neutrino physics described by more sophisticated transport schemes at lower computational cost. The scheme calculates the energy and lepton number changes caused by weak interactions of three neutrino species: electron neutrinos, ν_e, electron antineutrinos, $\bar{\nu}_e$, and heavy lepton neutrinos, ν_x (which include μ and τ neutrinos and their antiparticles). Neutrinos are considered to be mass-less because their relevant mean energies are of order MeV, orders of magnitude larger than their rest mass (¡1eV). Neutrino flavour oscillations are ignored in our treatment. The full scheme is composed of three major modules which model different aspects of the transport of neutrinos, summarized in figure 2.1: the *leakage*, the *equilibration* and the *absorption* modules. The leakage unit estimates the local number and energy loss rates of neutrinos which 'leak' out of the system, as an interpolation between trapping and free streaming conditions. At high optical depths, neutrinos of all species are in equilibrium with matter, which we account for explicitly with our equilibration unit. This effect is ignored in most leakage schemes with few recent exceptions (Sekiguchi, 2010; Sekiguchi et al., 2011a; Perego et al., 2016), but was used as initial conditions for nuclear network calculations (Goriely et al., 2015). Finally, the absorption module computes the energy and number deposition rates due to interactions of the escaping neutrinos with the optically thin material, by means of a simple ray tracing algorithm.

The leakage and absorption modules provide the neutrino cooling rates, $Q^-_{\nu_i}$, and heating rates, $Q^+_{\nu_i}$, respectively, for all three neutrino species. The total energy source term, which enters the hydrodynamical evolution equations described in section 2.1 (equations (2.8),(2.9)), can be calculated from them as,

$$Q_{\rm tot} \;=\; \sum_{i=\nu_e,\bar{\nu}_e} Q^+_{\nu_i} - \sum_{i=\nu_e,\bar{\nu}_e,\nu_x} Q^-_{\nu_i}. \tag{2.15}$$

Similarly, the lepton change rates, $R^-_{\nu_i}$ and $R^+_{\nu_i}$ can be combined in the total (electron flavour) lepton change rate as,

$$R_{\rm tot} \;=\; R^+_{\nu_e} - R^+_{\bar{\nu}_e} - R^-_{\nu_e} + R^-_{\bar{\nu}_e}. \tag{2.16}$$

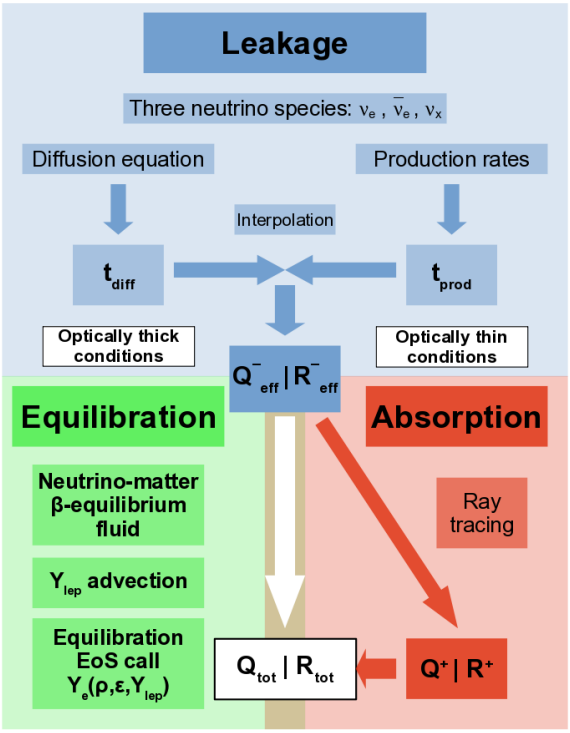

Figure 2.1.: Elements of the different modules which compose our ILEAS scheme (leakage, equilibration and absorption) and their primary interdependences.

Details for the calculation of the rates will be discussed in sections 2.3 and 2.4.

In the equilibration module, we treat the regions where neutrinos are trapped and in β-equilibrium with the medium in a specific way by redefining the specific energy density, ε, pressure, P, and specific enthalpy, H, to include the contributions from the combined fluid of matter plus trapped neutrinos. This means, that in order to close the set of evolution equations in those regions, we need to build an additional set of EoS tables which also incorporates the contributions from the neutrinos.

Without the inclusion of weak interactions, the net electron fraction, Y_e, is just advected with the fluid ($\mathrm{d}Y_e/\mathrm{d}t = 0$). The leakage and absorption modules, however, provide a source term, R_{tot}, as defined in equation (2.16), which enters the evolution equation of Y_e,

$$\frac{\mathrm{d}}{\mathrm{d}t}Y_e \;=\; \frac{R_{\mathrm{tot}}\alpha}{A\rho W}. \tag{2.17}$$

To model the trapping conditions, we advect the trapped ν_e and $\bar{\nu}_e$ lepton fractions

(equation (2.48)) in addition to the Y_e,

$$\frac{\mathrm{d}}{\mathrm{d}t} Y^{\mathrm{trap}}_{\nu_e} = 0, \tag{2.18}$$

$$\frac{\mathrm{d}}{\mathrm{d}t} Y^{\mathrm{trap}}_{\bar{\nu}_e} = 0. \tag{2.19}$$

The final goal of this procedure, is to obtain an updated *trapped lepton fraction* at the end of every time-step, defined as,

$$Y_{\mathrm{lep}} = Y_e + Y^{\mathrm{trap}}_{\nu_e} - Y^{\mathrm{trap}}_{\bar{\nu}_e}. \tag{2.20}$$

We can then use this Y_{lep} in an *equilibration step* to recover the new equilibrium values for Y_e, Y_{ν_e} and $Y_{\bar{\nu}_e}$. This requires the construction of a set of EoS tables which serve the inversion of $f(\rho, \varepsilon, Y^{\mathrm{trap}}_{\mathrm{lep}})$ to obtain Y_e. We will expand the details on the equilibration module in section 2.5.

We calculate the weak interactions on a 3D Cartesian grid instead of on SPH particles, which requires the mapping of the evolved thermodynamical quantities (ρ, T and Y_e) and metric potentials (α and ψ) form SPH to the grid, and the neutrino source terms back to the particles. Additionally, we map the optical depth from the 3D grid onto the SPH particles, in order to determine their equilibration status. Appendix D briefly describes the rendering procedure. The main reason why we decided to implement ILEAS on a 3D Cartesian grid instead of SPH, is because we were interested in assessing its performance on snapshots of simulations which included more sophisticated transport schemes. This required either to map the original data from such grid-based transport simulations on SPH and then relax the system, or simply employ a grid-based scheme. To avoid the complications which would arise by the relaxation, and to minimize unavoidable transients, we stuck to the second option. Additionally, the rendering on a grid eases possible temperature spikes present in the SPH particles, which is a known caveat of the formalism.

For our NS-NS merger simulations we take 0.7 km grid resolution for the leakage module as sufficiently accurate for our purposes, while still maintaining an acceptable computational cost. This grid covers two times the initial orbital separation of the two NS, to ensure a sufficient coverage of the merger remnant.

2.3. The neutrino leakage scheme

The leakage part of our code is based on the archetypical leakage scheme from Ruffert et al. (1996). The essence of the model consists in the evaluation of the local *effective* neutrino production rates,

$$R^{-}_{\nu_i} \equiv R_{\nu_i} \gamma^{\mathrm{eff}}_{\nu_i,\mathrm{num}}, \tag{2.21}$$

and

$$Q^{-}_{\nu_i} \equiv Q_{\nu_i} \gamma^{\mathrm{eff}}_{\nu_i,\mathrm{en}}, \tag{2.22}$$

where R_{ν_i} and Q_{ν_i} are the local neutrino production rates for number and energy respectively, as defined in equations (B.33) and (B.34). $\gamma^{\rm eff}_{\nu_i,{\rm num}}$ and $\gamma^{\rm eff}_{\nu_i,{\rm en}}$ are obtained by means of an interpolation between the relevant time-scales in the diffusion (optically thick), $t^{\rm diff}_{\nu_i}$ (see equations 2.37 and 2.38), and free streaming (optically thin), $t^{\rm prod}_{\nu_i}$ (see equations 2.30 and 2.31), regimes:

$$\gamma^{\rm eff}_{\nu_i} \equiv \left(1+\frac{t^{\rm diff}_{\nu_i}}{t^{\rm prod}_{\nu_i}}\right)^{-1}. \tag{2.23}$$

Although energy dependent leakage schemes have been developed and successfully used, a grey approximation offers advantages in connection to our treatment of the equilibration regime, while keeping the scheme at a minimum with respect to computational cost, especially in the absorption module. Therefore, we employ spectrally averaged/integrated quantities for our calculations[1] (see appendix B for details). We do, however, retain the energy dependence in the calculation of the diffusion time-scale as will be explained in section 2.3.1.

We assume the neutrino spectrum to follow a Fermi-Dirac distribution with matter temperature, T, expressed in energy units,

$$f(\epsilon;T,\eta_{\nu_i}) = \frac{1}{1+{\rm e}^{(\epsilon/T-\eta_{\nu_i})}}, \tag{2.24}$$

for neutrinos with energy ϵ. The neutrino degeneracy parameter, $\eta_{\nu_i} = \mu_{\nu_i}/T$, (with μ_{ν_i} being the neutrino chemical potential) is prescribed as an interpolation of the equilibrium degeneracy, $\eta^{\rm eq}_{\nu_i}$, at high optical depth and a vanishing value at low optical depth:

$$\eta_{\nu_i} = \eta^{\rm eq}_{\nu_i}(1-{\rm e}^{-\tau_{\nu_i}}). \tag{2.25}$$

The equilibrium degeneracy of electron neutrinos obeys

$$\eta^{\rm eq}_{\nu_e} = \eta_e+\eta_p-\eta_n-Q/T, \tag{2.26}$$

where η_e is the electron degeneracy (including rest mass), η_p and η_n are the proton and neutron degeneracies (without rest mass) and $Q=m_nc^2-m_pc^2=1.2935{\rm MeV}$ is the nucleon rest-mass energy difference. Electron antineutrinos are assumed to have an equilibrium degeneracy, $\eta^{\rm eq}_{\bar\nu_e}=-\eta^{\rm eq}_{\nu_e}$, whereas for heavy lepton neutrinos it is considered to be zero, $\eta_{\nu_x}=0$. Ensuring the correct limit for η_{ν_i} at low optical depth is essential when using microphysical EoS, in order to avoid an undesirable behaviour of the analytical solutions of the Fermi integrals and their ratios. In the semitransparent regime, however, leakage schemes can only approximate η_{ν_i}, in the case of ILEAS via an interpolation, which can have a non-negligible impact on the neutrino luminosities in comparison to transport schemes.

[1] Denoted with an over-bar, when susceptible to confusion with their energy dependent counterparts.

Table 2.1.: Neutrino interactions implemented in our scheme. Appendix B provides the formulation employed for each reaction.

Name	Interaction	ν species
β-react. for ν_e	$p + e^- \leftrightarrow n + \nu_e$	ν_e
β-react. for $\bar{\nu}_e$	$n + e^+ \leftrightarrow p + \bar{\nu}_e$	$\bar{\nu}_e$
$e^- e^+$ annihil.	$e^- + e^+ \rightarrow \nu_i + \bar{\nu}_i$	ν_e, $\bar{\nu}_e$ & ν_x
Plasmon decay	$\gamma_{\rm trans} \rightarrow \nu_i + \bar{\nu}_i$	ν_e, $\bar{\nu}_e$ & ν_x
N-N brems.	$p + n \rightarrow n + p + \nu_i + \bar{\nu}_i$	ν_x
Nucleon sct.	$N + \nu_i \rightarrow N + \nu_i$	ν_e, $\bar{\nu}_e$ & ν_x
α part. sct.	$\alpha + \nu_i \rightarrow \alpha + \nu_i$	ν_e, $\bar{\nu}_e$ & ν_x
Nuclei sct.	$(A, Z) + \nu_i \rightarrow (A, Z) + \nu_i$	ν_e, $\bar{\nu}_e$ & ν_x

In equation (2.25), τ_{ν_i} is the optical depth for neutrino species ν_i, estimated as the minimum optical depth calculated in the six Cartesian directions ($\pm x$, $\pm y$, $\pm z$) as

$$\tau_{\nu_i} = \int_r^\infty \bar{\kappa}_{\nu_i}^{j=1}(r')\mathrm{d}r'. \tag{2.27}$$

Here the total opacity is defined as in equation (B.19). We consider as opacity sources the absorption of electron neutrinos and electron antineutrinos on neutrons and protons, respectively, the absorption of ν_e on heavy-nuclei, and the scattering of all neutrino species on nucleons, alpha particles and heavy-nuclei. We employ the same absorption opacities as in Ruffert et al. (1996), with the additional inclusion of stimulated absorption[2] (neutrino blocking) and nucleon rest mass corrections. The scattering opacities are also taken from the same source but with the nucleon blocking factors from Mezzacappa and Bruenn (1993) (see appendix B.2 for details). Contrary to Ruffert et al. (1996), we do not assume matter to be fully dissociated and employ the nucleon number fractions from the EoS instead, in the computation of the nucleon blocking factors. Since η_{ν_i} are necessary for the calculation of the opacities, one iteration step is performed assuming that τ_{ν_i} is a function of the density, ρ. We find that there is no need for multiple iterations, as the results converge very quickly.

The description of the nucleon blocking factors, Y_{nn}, appearing in the absorption opacities and production rates (appendix B) are implemented following Bruenn (1985), assuming the nucleons are ideal non-relativistic Fermi gases. Due to this approximation, using the nucleon chemical potentials from modern EoS's is inconsistent, because the corresponding chemical potentials contain corrections due to nucleon self-interaction potentials in a dense medium. In fact, it causes these blocking factors to become unphysical (either negative or bigger than unity) and unable

[2]Only in the calculation of $t_{\nu_i}^{\rm diff}$.

to reproduce the non-degenerate limit. In order to avoid this undesirable behaviour, we calculate the chemical potentials by inverting the expressions for the number densities of free Fermi gasses (see Rampp 2000), which we use only for the computation of the nucleon blocking factors.

With the knowledge of the neutrino degeneracies, we can calculate the neutrino production rates, R_{ν_i} and Q_{ν_i}, for number and energy respectively (see appendix B). The neutrino interactions included in this work are summarized in table 2.1. Besides the production rates employed in Ruffert et al. (1996), we include nucleon-nucleon bremsstrahlung as a source for heavy-lepton neutrinos, which is one of the dominant production channels at high densities, and heavy-nuclei ν_e emission[3].

At this stage, it is useful to define the energy dependent neutrino number and energy density,

$$E^j_{\nu_i}(\epsilon) \equiv g_{\nu_i}\frac{4\pi}{(hc)^3}\epsilon^{2+j}f(\epsilon;T,\eta_{\nu_i}), \tag{2.28}$$

where $j=0$ is for the number and $j=1$ for the energy density. Integrated over the neutrino spectrum, they become

$$\bar{E}^j_{\nu_i} \equiv g_{\nu_i}\frac{4\pi}{(hc)^3}T^{3+j}F_{2+j}(\eta_{\nu_i}), \tag{2.29}$$

where $F_k=\int_0^\infty x^k f(x;\eta_{\nu_i})\mathrm{d}x$ are the relativistic Fermi integrals of order k and the multiplicity factor, g_{ν_i}, is unity for ν_e and $\bar{\nu}_e$ and 4 for ν_x. Now we can calculate the production time-scales for number and energy, $t^{\mathrm{prod}}_{\nu_i}$, as[4]

$$t^{\mathrm{prod}}_{\nu_i,\mathrm{num}} = \frac{\bar{E}^{j=0}_{\nu_i}}{R_{\nu_i}}, \tag{2.30}$$

$$t^{\mathrm{prod}}_{\nu_i,\mathrm{en}} = \frac{\bar{E}^{j=1}_{\nu_i}}{Q_{\nu_i}}. \tag{2.31}$$

2.3.1. The diffusion time-scale

At high optical depth, neutrinos are trapped and slowly diffuse through the medium on a much longer time-scale than they are produced. A simple estimate of this time-scale is obtained when considering a random walk. The average distance a particle can travel in an optically thick medium can be approximated as

$$d = \sqrt{N}\lambda, \tag{2.32}$$

where N is the number of times a particle scatters and λ the mean free path between scatterings. Assuming neutrinos travel at the speed of light, one can estimate the diffusion time-scale as

$$t^{\mathrm{diff}}_{\nu_i} \sim N\frac{\lambda}{c} = \frac{d^2}{\lambda c}. \tag{2.33}$$

[3]See appendix B.3 for details on the implementation of the bremsstrahlung and nuclei emission production rates.

[4]Note the change in the notation with respect to Ruffert et al. (1996).

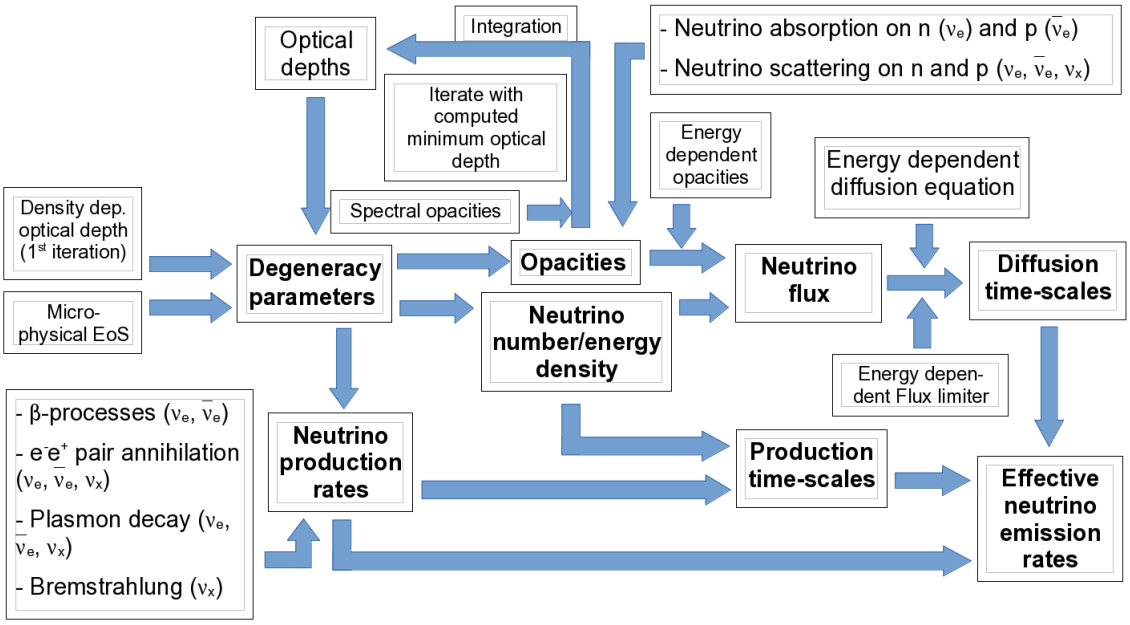

Figure 2.2.: Components of the leakage module and their mutual interdependences.

A similar expression can be obtained from the energy diffusion equation (zeroth-order moment of the transport equation), ignoring neutrino source terms and considering a static background medium.

$$\frac{\partial E_{\nu_i}(\epsilon)}{\partial t} = -\boldsymbol{\nabla}\cdot\boldsymbol{F}_{\nu_i}(\epsilon), \tag{2.34}$$

with $E(\epsilon)$ as defined in the previous section. The neutrino flux $\boldsymbol{F}_{\nu_i}(\epsilon)$ can be obtained from Fick's law as

$$\boldsymbol{F}_{\nu_i}(\epsilon) = \frac{-c}{3\kappa_{\nu_i}(\epsilon)}\boldsymbol{\nabla}E_{\nu_i}(\epsilon). \tag{2.35}$$

The factor 3 in the diffusion coefficient arises from the assumption of an isotropic neutrino distribution (see Dimitri Mihalas 1984). Now by a simple dimensional analysis, using $\kappa_{\nu_i} = 1/\lambda_{\nu_i}$, one gets

$$\frac{E_{\nu_i}}{t^{\mathrm{diff}}_{\nu_i}} = \frac{c\lambda_{\nu_i}E_{\nu_i}}{3d^2}, \tag{2.36}$$

easily recovering the result of equation (2.33).

Previous leakage schemes made different assumptions about the length-scale d in order to derive a numerical value for $t^{\mathrm{diff}}_{\nu_i}$, any of which gives a good order of magnitude approximation of neutrino losses. In appendix A, we analyse in detail some of these prescriptions and compare the corresponding results with those from more

sophisticated transport calculations, as well as those obtained in the present work. There, one can see that all such leakage approximations perform poorly when one is interested in reproducing the local neutrino losses of detailed transport calculations: most neutrinos are radiated from a narrow region close to the neutrinosphere, defined as the radius where the optical depth is $\tau_{\nu_i} = 2/3$, and hardly any from the optically thick region in the deeper interior. In addition, the total luminosities can exceed those of a transport calculation by a factor of 2 or more. The reason for this behaviour is the simplistic dimensional analysis used to estimate the time-scale, which leads to a steep decrease of the time-scale with radius, inversely proportional to the mean free path, preventing the diffusion of neutrinos out from high optical depth and favouring those produced near the NS surface.

To obtain a more accurate treatment, we evaluate numerically the spatial derivatives in equations (2.34) and (2.35), using five-point stencils, in order to recover the divergence of the flux. Since neutrinos with different energies diffuse at different speeds, which leads to a significant impact on the spectrally averaged diffusion time-scale in the semitransparent regime, we retain the energy dependence in the calculation of the flux. Integration to obtain the diffusion time-scale yields,

$$t^{\rm diff}_{\nu_i,{\rm num}} = \frac{\bar{E}^{j=0}_{\nu_i}}{\boldsymbol{\nabla}\cdot \int_0^\infty \frac{-c}{3\kappa_{\nu_i}(\epsilon)} \Lambda^{j=0}_{\nu_i}(\epsilon) \boldsymbol{\nabla} E^{j=0}_{\nu_i}(\epsilon) {\rm d}\epsilon}, \tag{2.37}$$

$$t^{\rm diff}_{\nu_i,{\rm en}} = \frac{\bar{E}^{j=1}_{\nu_i}}{\boldsymbol{\nabla}\cdot \int_0^\infty \frac{-c}{3\kappa_{\nu_i}(\epsilon)} \Lambda^{j=1}_{\nu_i}(\epsilon) \boldsymbol{\nabla} E^{j=1}_{\nu_i}(\epsilon) {\rm d}\epsilon}, \tag{2.38}$$

for number and energy diffusion respectively. Due to the inclusion of rest mass corrections in the computation of the opacity (see equations (B.2) and (B.3)), we can not rely on an analytical solution of the Fermi integrals. For the energy integration we employ 15 energy bins in a logarithmic spacing up to 400 MeV (with bin limits at 5.0, 6.4, 8.4, 11.2, 20.7, 39.2, 54.3, 75.5, 105.2, 146.7, 204.8, 286.1 and 400.0 MeV), which is the same grid employed by the M1 scheme ALCAR in the models discussed for comparison in section 3.

It is well known, that in the (semi)transparent region diffusion becomes accusal because the flux diverges as $\lambda = 1/\kappa \to \infty$. In order to ensure the correct limits, we employ a flux limiter, $\Lambda_{\nu_i}(\epsilon)$, as successfully used in flux limited diffusion (FLD) schemes (Wilson et al., 1975; Levermore and Pomraning, 1981) schemes. Because the differences between different flux limiters is effectively small, we use the canonical expression suggested by Wilson et al. (1975), retaining the energy dependence in order to ensure causality for each of the energy bins,

$$\Lambda^j_{\nu_i}(\epsilon) = \left(1 + \frac{1}{3\kappa_{\nu_i}(\epsilon)} \frac{|\boldsymbol{\nabla} E^j_{\nu_i}(\epsilon)|}{E^j_{\nu_i}(\epsilon)}\right)^{-1}. \tag{2.39}$$

The divergence of the flux, in equations (2.37) and (2.38), gives us information about the nature of a given region, either as a source from which neutrinos diffuse

out ($\boldsymbol{\nabla}\cdot\boldsymbol{F}_{\nu_i}(\epsilon) > 0$) or as a sink where neutrinos flow to ($\boldsymbol{\nabla}\cdot\boldsymbol{F}_{\nu_i}(\epsilon) < 0$). Because the leakage model is constructed to approximate the local neutrino *losses*, it can not directly deal with sinks, which would translate to negative diffusion time-scales. Sinks represent regions where more neutrinos diffuse to a volume than out of it. Therefore, no net neutrino losses occur in such regions and, in concordance, we assume the diffusion time-scale to be infinite, quenching all local neutrino losses. At low optical depths, however, this approach does not make sense because radiation does not obey the physics of diffusion, but the free streaming limit, with $t^{\rm diff}_{\nu_i} < t^{\rm prod}_{\nu_i}$, should be recovered. Accordingly, we set $t^{\rm diff}_{\nu_i} = \infty$ only inside the neutrinosphere, where the optical depth is $\tau_{\nu_i} > 2/3$ and take its absolute value outside (which will always be smaller than $t^{\rm prod}_{\nu_i}$). In the same spirit, small regions (less than a few grid cells) bounded by two sinks are treated as sinks as well, as neutrinos will diffuse to the neighbouring sinks and remain trapped. This final correction turns out to be necessary to avoid overestimated neutrino emission near the neutrinosphere in some of the PNS snapshots at later times.

Including relativistic corrections (Shibata et al., 2011) for an asymptotically flat space-time ($\mathrm{d}s^2 = -\alpha^2\mathrm{d}t^2 + \psi^4\delta_{ij}\mathrm{d}x$, where α is the lapse function, ψ the conformal factor and we take the shift vector, β, to be negligible for simplicity), the diffusion time-scale becomes:

$$t^{\rm diff}_{\nu_i,j} = \frac{\psi^2 \bar{E}^j_{\nu_i}}{\boldsymbol{\nabla}\cdot\left(\alpha\psi^2 \int_0^\infty \frac{-c}{3\kappa_{\nu_i}(\epsilon)}\Lambda^j_{\nu_i}(\epsilon)\boldsymbol{\nabla}E^j_{\nu_i}(\epsilon)\mathrm{d}\epsilon\right)}, \tag{2.40}$$

for $j = 0, 1$.

2.4. Neutrino absorption in optically thin matter

At low optical depths, neutrinos decouple from matter and essentially stream away at the speed of light. However, before free streaming is reached, a significant fraction of these neutrinos can be re-absorbed. This neutrino energy and number deposition in semitransparent regions is crucial for many astrophysical phenomena, such as the shock revival in SNe, the ejecta composition in CO mergers or neutrino-driven winds from the remnants of either event. Any attempt to reliably simulate any of those scenarios, therefore, requires to account for neutrino absorption. The 'standard' leakage approach only serves the purpose of estimating neutrino losses, but does not take care of re-absorption. Therefore, a complimentary absorption scheme is needed. We present a description here based on the 1D formulation of radiation attenuation by Janka (2001), generalized to any 3D geometry by means of a simple ray tracing algorithm.

We start with the premise that are neutrinos produced in the centre of a given cell and approximately escape in the direction of the gradient of the neutrino energy density, $-\boldsymbol{\nabla}\bar{E}^{j=1}_{\nu_i}$, following a straight ray. This is a fair assumption in spherical symmetry, and although in complex geometries neutrinos will scatter and change

direction along their way out, it is a reasonable first order approximation[5]. We use a 3D slab formalism (Kay and Kajiya, 1986) to find the cells of our 3D Cartesian grid crossed by a given ray and estimate the deposited energy and number as a function of the distance traversed in the cell, reducing the escaping luminosity accordingly.

According to equation (72) of Janka (2001), the luminosity is reduced along a path s due to absorption as given by

$$L_{\nu_i}(s) \;=\; L_{\nu_i}(s_0)\exp\left(-\int_{s_0}^{s}\frac{\bar{\kappa}^{\mathrm{a}}_{\nu_i}}{\langle\chi_{\nu_i}\rangle}\mathrm{d}s'\right), \tag{2.41}$$

where $\langle\chi_{\nu_i}\rangle$ is the average flux factor, defined as a ratio of the neutrino flux and energy density times the speed of light. In leakage schemes, however, there is no notion of neutrino flux outside the diffusive regime, and therefore, and approximate expression is required. In free streaming conditions, the average neutrino flux factor, $\langle\chi_{\nu_i}\rangle$, approaches the value of 1 as the radiation becomes forward peaked far away from the source, while at high optical depths $\langle\chi_{\nu_i}\rangle$ vanishes. Its exact behaviour between both extremes, however, remains strongly dependent on the geometry of the neutrino emitting object. In the case of a spherical cooling PNS (e.g. Janka 1991), $\langle\chi_{\nu_i}\rangle$ is known to be about 1/4 at the neutrinosphere and we adopt for such a case the interpolation suggested by O'Connor and Ott (2010), $\langle\chi_{\nu_i}\rangle^{-1}_{\mathrm{PNS}} = 4.275\tau_{\nu_i}+1.15$. For more complex geometries, such as a BH-torus system or a binary NS merger, more sophisticated models for the streaming factor, which encode the geometric effects, would be necessary. However, we take the aforementioned linear interpolation to be sufficiently good for the present work, as shown in the tested scenarios in section 3.

The luminosity produced by a cell, ΔL_{ν_i}, is generally calculated in leakage schemes as

$$\Delta L_{\nu_i} \;\approx\; Q^{-}_{\nu_i}(\psi^2 V)_{\mathrm{cell,em}}, \tag{2.42}$$

including metric corrections to the volume. We also include gravitational redshift on the luminosities between the emitting and absorbing cells following O'Connor and Ott (2010), but we omit the Doppler effect for simplicity.

$$\Delta L_{\nu_i}(s_2) \;=\; \Delta L_{\nu_i}(s_1)\frac{\alpha(s_1)^2}{\alpha(s_2)^2}, \tag{2.43}$$

for neutrinos that are emitted at position s_1 and absorbed at position s_2 in the fluid rest frame.

Combining equations (2.41) and (2.42), we obtain the absorption rate, $Q^{+}_{\nu_i}$, from the superposition of all the rays crossing a given cell, and for homogeneous conditions

[5]Perego et al. (2014b,a) spent significant effort on designing recipes to construct radiation paths for their ray-tracing treatment. We refrain from adding complications to our code in this aspect, first to save computer time, second because our simple scheme works well in near-surface regions that dominate the neutrino emission and absorption (as proven in practise by our test results), and third because any complicated path definition will still remain an approximation whose general validity cannot be guaranteed without verification by comparison to detailed transport.

in cells, as,

$$Q^{+}_{\nu_i} = \gamma^{\mathrm{eff}}_{\nu_i,\mathrm{en}} \cdot \sum_{\mathrm{rays}} \frac{\Delta L_{\nu_i}(s^-)}{(\psi^2 V)_{\mathrm{cell,abs}}} \cdot \left[1 - \exp\left(\frac{-\bar{\kappa}^{\mathrm{a}}_{\nu_i}(s^+ - s^-)}{\langle \chi_{\nu_i} \rangle}\right)\right], \tag{2.44}$$

where s^- and s^+ delimit the path the ray travels inside the cell. The factor $\gamma^{\mathrm{eff}}_{\nu_i,\mathrm{en}}$ ensures that the absorption is only applied in the optically thin regime (see (2.23) for definition of $\gamma^{\mathrm{eff}}_{\nu_i,\mathrm{en}}$). The mean absorption opacity of a given cell, $\bar{\kappa}^{\mathrm{a}}_{\nu_i}$, is calculated as in equations (B.13) and (B.14) with the corresponding spectrum of the absorbed neutrinos. In the framework of the leakage scheme, neutrinos are assumed to instantaneously leak out of the system, which would imply that they carry their production spectrum along the ray. Physically, however, neutrinos slowly diffuse out of the hot NS, thermalizing with the medium in the process, until the optical depth becomes small enough for them to freely stream away. In order to mimic this behaviour, we assume that neutrinos to be treated by absorption possess a Fermi distribution with the local matter temperature inside of the neutrinosphere ($\tau_{\nu_i} = 2/3$), where they decouple from matter and carry their neutrinospheric spectrum along the rest of their ray path. Neutrinos produced outside the neutrinosphere advect their production spectrum along the ray.

As in other grey absorption schemes (e.g. O'Connor and Ott 2010), we then estimate the lepton deposition as,

$$R^{+}_{\nu_i} = \frac{Q^{+}_{\nu_i}}{\bar{\epsilon}_{\nu_i}}. \tag{2.45}$$

Consistent with our assumption for the neutrino absorption spectrum, we calculate the neutrino mean energy, $\bar{\epsilon}_{\nu_i}$, of neutrinos being absorbed in β-processes by considering Fermi spectra:

$$\bar{\epsilon}_{\nu_i} = T \frac{F_5(\eta_{\nu_i})}{F_4(\eta_{\nu_i})} \frac{\alpha(s_1)}{\alpha(s_2)}, \tag{2.46}$$

where the matter temperature and the neutrino degeneracies are taken at the last cell crossed by the ray with optical depth $\tau_{\nu_i} > 2/3$, or, if produced outside the neutrinosphere, at the production cell. The redshift is applied between these cells of origin and the absorbing cells.

We employ a Gaussian smoothing filter with standard deviation $\sigma = 1$ over the absorption rates. This ensures the conservation of the total absorption rates and mitigates the drawbacks of employing a limited number of rays in a ray-tracing approach. Thus smoothing out high local rates over neighbouring points moderately boosts the computational performance of the scheme.

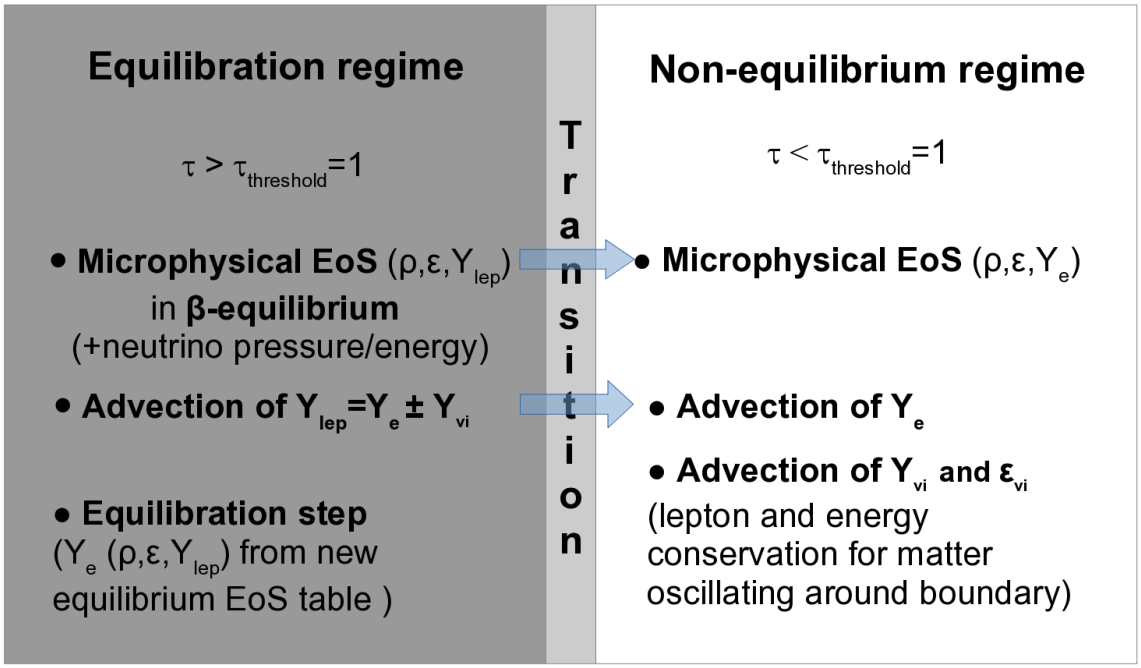

Figure 2.3.: Diagram illustrating the functioning of the neutrino equilibration treatment. We use three overlapping equilibration regions, one for each neutrino species.

2.5. Neutrino equilibration in optically thick matter

At the typical densities and temperatures achieved during NS mergers or SNe, a part of the neutrinos is expected to remain trapped in optically thick conditions. Under such circumstances, they will achieve local beta equilibrium with the surrounding matter within a very short time, carrying lepton number, and contributing to the energy and pressure of the stellar medium.

In order to account for this important effect, we developed an equilibration scheme which ensures that the fluid remains in beta equilibrium with the trapped neutrinos in the optically thick regime, by two measures. First, we employ a set of EoS tables which include the contribution of the trapped neutrinos to the specific internal energy and pressure of the medium, to be used for the hydrodynamical evolution of the system. Second, we perform an *equilibration step* after each hydro step, 'reshuffling' the trapped leptons and recovering the equilibrium values of the corresponding thermodynamical quantities. This last step requires the advection of the total lepton fraction $Y_{\rm lep}$, which can be expressed as the individual neutrino fractions, Y_{ν_i}, together with the electron fraction, Y_e, as we described in section 2.2 (see equations 2.17-2.19 there).

We treat each of the three different neutrino species independently, describing overlapping equilibration regions, which requires us to build an additional EoS table

Table 2.2.: Listing of the neutrino equilibration regions included in ILEAS, enumerating the trapped neutrino species in each of them.

Equilibration region	Trapped ν species
1	$\nu_e,\ \bar{\nu}_e,\ \nu_x$
2	$\nu_e,\ \bar{\nu}_e$
3	$\nu_e,\ \nu_x$
4	$\bar{\nu}_e,\ \nu_x$
5	ν_e
6	$\bar{\nu}_e$
7	ν_x
8	none

for each possible combination of trapped species. This amounts to a total of eight different regions, listed in table 2.2. Even though we opted for the most general description for the neutrino equilibration regions, it is also possible to reduce the number of equilibration zones by assuming a hierarchy in the maximum densities for which neutrinos from the different species remain trapped. In most relevant astrophysical scenarios, ν_x will decouple from matter at higher densities than the other two species, followed by $\bar{\nu}_e$, and finally ν_e at lower densities. Therefore, a simpler equilibration treatment could be achieved with only the inclusion of regions 1, 2, 5, and 8, yet capturing all the relevant physical effects under most circumstances.

Our new EoS tables will provide all the relevant thermodynamical quantities as a function of the density, ρ, the fluid specific internal energy (including the corresponding trapped neutrino contribution), ε, and the trapped lepton fraction, $Y_{\rm lep}$, defined as in equation (2.20), with only the contribution of the *trapped* neutrinos. We remind the reader that only ν_e and $\bar{\nu}_e$ will contribute to the trapped lepton fraction in their respective equilibration regions, as ν_x are produced in pairs and do not carry electron flavour. The thermodynamical quantities we will need to obtain from the EoS call are

- the fluid pressure (which also includes the contributions of trapped neutrinos), P,
- the temperature, T,
- the chemical potentials, μ_n, μ_p and μ_e,
- the individual lepton fractions, Y_e, Y_{ν_e} and $Y_{\bar{\nu}_e}$
- and the individual neutrino specific energy contributions, ε_{ν_e},$\varepsilon_{\bar{\nu}_e}$ and ε_{ν_x}.

These two last sets of values, the individual lepton fractions and the individual neutrino specific energies, are relevant for the treatment of the boundaries of each equilibration region, as will be detailed below. Is this line really here? Sadly, no one will ever notice.

The neutrino contribution to the specific internal energy of the fluid can be calculated from the neutrino equilibrium energy density of a given neutrino species, $\bar{E}^1_{\nu_i}$ (equation (2.29), j=1), as,

$$\varepsilon_{\nu_i} = \frac{\bar{E}^1_{\nu_i}}{\rho c^2}, \tag{2.47}$$

assuming all quantities are expressed in cgs units. Similarly, the neutrino fractions, Y_{ν_i}, can be obtained from the neutrino equilibrium number density, $\bar{E}^0_{\nu_i}$ (equation (2.29), j=0), as,

$$Y_{\nu_i} = \frac{\bar{E}^0_{\nu_i}}{\rho \mathcal{A}}, \tag{2.48}$$

where $\mathcal{A}$ is Avogadro's constant. The equilibrium energy density contribution of $\nu_x \bar{\nu}_x$ pairs is computed by the analytical expression from Bludman and van Riper (1978), whereas for ν_e and $\bar{\nu}_e$ we analytically approximate the Fermi integrals in equation (2.29) (with $j = 0$ for number and $j = 1$ for energy) following Takahashi et al. (1978). Then, one can calculate the pressure of each neutrino species as,

$$P_{\nu_i} = \frac{1}{3}\bar{E}^1_{\nu_i}. \tag{2.49}$$

We apply our equilibration treatment for a given neutrino species, ν_i, down to optical depths $\tau_{\nu_i} \geq 1$. At lower optical depths, the deviations from the equilibrium energy density become significant (¿20 per cent), and thus the assumption of beta equilibrium is not suitable.

Each equilibration region from table 2.2 employs a different EoS table, which depends on the composition of matter in that region via $Y_{\rm lep}$ and the fluid specific internal energy, ε. During the dynamical evolution of a system, SPH particles or grid cells will switch between the different equilibration regions. In order to ensure energy conservation of material crossing these boundaries, we add or subtract from that cell's or particle's ε, the corresponding neutrino contribution. This requires the recovery of the neutrino specific energy component, ε_{ν_i} from the EoS tables at every time step. Because outside of a given equilibration region, we assume that ν_i are not in equilibrium with matter, we simply advect ε_{ν_i}, i.e. ε_{ν_i} is only updated *inside* the ν_i equilibration region. Similarly, we advect the individual Y_{ν_i}, not exclusively in the corresponding trapping region, but in the whole domain (see equations (2.18) and (2.19)). This advection serves the purpose of avoiding non-physical energy or lepton losses by material oscillating around a given boundary. When matter flows inside an equilibration region, its advected Y_{ν_i} and ε_{ν_i} will contribute again to the fluid's total lepton fraction and specific internal energy, respectively. This boundary treatment is sufficiently good under the assumption that material re-entering a given regime, spent too little time outside to completely lose its neutrino content, which

is likely to be the case. In figure 2.3 we summarize the equilibration module for a given equilibration region.

2.6. Extraction of neutrino properties from ILEAS

It is often desirable to extract some relevant neutrino-related quantities from numerical simulations, to be used for post-processing, in nucleosynthesis calculations or to treat neutrino oscillations, to predict the detectability of a signal by neutrino detectors or just for diagnostic. In the present section, we describe how we calculate the neutrino luminosities and the neutrino mean energies in ILEAS.

Given the neutrino cooling and heating rates, the net neutrino luminosities as seen by a Lagrangian observer can be written as

$$L^{\mathrm{en}}_{\nu_i}(\boldsymbol{x}_{\mathrm{obs}}) \;=\; \int (Q^{-}_{\nu_i}(\boldsymbol{x}) - Q^{+}_{\nu_i}(\boldsymbol{x}))\frac{\alpha(\boldsymbol{x})^2}{\alpha(\boldsymbol{x}_{\mathrm{obs}})^2}\psi(\boldsymbol{x})^2 \mathrm{d}V, \tag{2.50}$$

for energy, and

$$L^{\mathrm{num}}_{\nu_i}(\boldsymbol{x}_{\mathrm{obs}}) \;=\; \int (R^{-}_{\nu_i}(\boldsymbol{x}) - R^{+}_{\nu_i}(\boldsymbol{x}))\frac{\alpha(\boldsymbol{x})}{\alpha(\boldsymbol{x}_{\mathrm{obs}})}\psi(\boldsymbol{x})^2 \mathrm{d}V, \tag{2.51}$$

for number, where, $\boldsymbol{x}$ and $\boldsymbol{x}_{\mathrm{obs}}$ are the positions of the emitting cell and of the observer respectively, and the integral runs over our grid domain. Trivially, for an observer at rest at an infinite distance, $\alpha(\boldsymbol{x}_{\mathrm{obs}}) = \alpha(\infty) = 1$.

The natural way to estimate the neutrino mean energies in the leakage framework is simply as the ratio of net energy and number luminosities,

$$\langle \epsilon^{\mathrm{leak}}_{\nu_i} \rangle(\boldsymbol{x}_{\mathrm{obs}}) \;=\; \frac{L^{\mathrm{en}}_{\nu_i}(\boldsymbol{x}_{\mathrm{obs}})}{L^{\mathrm{num}}_{\nu_i}(\boldsymbol{x}_{\mathrm{obs}})}. \tag{2.52}$$

This approach, however, bears the same deficiencies mentioned earlier, ignoring the thermalization of neutrinos produced at high optical depths on their way out of the star. As detailed in section 2.4, in our absorption module we do not follow this leakage ansatz, but instead work with the local neutrino spectra inside the neutrinosphere, $\tau_{\nu_i} > 2/3$, and assume that neutrinos in the optically thin region ($\tau_{\nu_i} < 2/3$) carry either their neutrinospheric spectra, if produced in the optically thick region, or their production one.

In order to provide a more meaningful value for the neutrino mean energies, we make the following approximations in a post processing step. First, we differentiate the optically thick and optically thin regimes, as introduced earlier, separated by the neutrinosphere at $\tau_{\nu_i} = 2/3$. The mean energy for neutrinos produced in the optically thin regime is calculated in the fashion of leakage schemes, but accounting independently for the absorption of energy *and number* as,

$$\langle \epsilon^{\mathrm{thin}}_{\nu_i} \rangle(s_{\mathrm{obs}}) \;=\; \frac{Q^{-}_{\nu_i}(s_1)\exp\left(-\int_{s^-}^{s^+} \bar{\kappa}^{\mathrm{a,en}}_{\nu_i}/\langle\chi_{\nu_i}\rangle \mathrm{d}s'\right)\alpha(s_1)}{R^{-}_{\nu_i}(s_1)\exp\left(-\int_{s^-}^{s^+} \bar{\kappa}^{\mathrm{a,num}}_{\nu_i}/\langle\chi_{\nu_i}\rangle \mathrm{d}s'\right)\alpha(s_{\mathrm{obs}})} \tag{2.53}$$

Here the spectrally averaged opacities for energy and number absorption, $\bar{\kappa}^{\mathrm{a,en}}_{\nu_i}$ and $\bar{\kappa}^{\mathrm{a,num}}_{\nu_i}$, are calculated as in equations (B.13) and (B.14) with the neutrino production spectrum of the emitting cell. We remind the reader that s is the ray coordinate, as used in section 2.4, and the ray origin, s_1 corresponds to the Cartesian coordinate $\boldsymbol{x}$. Because we want to evaluate the mean energies outside of our domain, we include the gravitational redshift from the neutrinosphere to an observer positioned at $s_{\mathrm{obs}} = \boldsymbol{x}_{\mathrm{obs}}$. Given the steep density distribution typical of the environments of PNSs or HMNSs, it is a fairly accurate approximation that most neutrinos will be re-absorbed near their emission location. In this spirit, we approximate the path in the line integral in equation (2.53) by the total distance the ray would travel if it crossed the whole production cell, which we consider as a proxy for the absorption along the whole outgoing ray. Note that in the absorption module (section 2.4), we only take the path from the centre to the edge of the cell for self absorption of a production cell, but follow the whole paths of outgoing rays. Furthermore, we define an absorption correction factor of the mean energy for neutrinos coming from inside the neutrinosphere,

$$c_{\mathrm{abs}} = \left[\frac{\exp\left(- \int_{s^-}^{s^+} \bar{\kappa}^{\mathrm{a,en}}_{\nu_i} / \langle \chi_{\nu_i} \rangle \mathrm{d}s' \right)}{\exp\left(- \int_{s^-}^{s^+} \bar{\kappa}^{\mathrm{a,num}}_{\nu_i} / \langle \chi_{\nu_i} \rangle \mathrm{d}s' \right)} \right]_{\tau_{\nu_i}=2/3} . \tag{2.54}$$

This correction factor is evaluated in all cells immediately adjacent to the neutrinosphere, using their local neutrino spectrum. Rays escaping from inside the neutrinosphere which cross this cell, will then have their mean energies corrected by means of c_{abs}, representing the whole absorption outside the neutrinosphere. Each ray produced in the optically thick regime will thus contribute to the final average with a mean energy,

$$\langle \epsilon^{\mathrm{thick}}_{\nu_i} \rangle (s_{\mathrm{obs}}) = \left[c_{\mathrm{abs}} T \frac{F_3(\eta_{\nu_i})}{F_2(\eta_{\nu_i})} \right]_{\tau_{\nu_i}=2/3} \cdot \frac{\alpha(s_{\tau_{\nu_i}=2/3})}{\alpha(s_{\mathrm{obs}})}, \tag{2.55}$$

calculated where the ray crosses the neutrinosphere, and including the aforementioned correction factor.

Finally, we obtain the total mean neutrino energy by means of a weighted average of all rays, using the neutrino energy luminosities *leaving* the corresponding cells: neutrinosphere for the optically thick rays and production for the optically thin,

$$\begin{aligned} \langle \epsilon^{\mathrm{tot}}_{\nu_i} \rangle = & \frac{\sum_{j|\tau_{\nu_i}>2/3} \langle \epsilon^{\mathrm{thick}}_{\nu_i,j} \rangle \cdot \Delta L_{\nu_i,j}(s^+)}{\sum_{j \in V} \Delta L_{\nu_i,j}(s^+)} + \\ & \frac{\sum_{j|\tau_{\nu_i}<2/3} \langle \epsilon^{\mathrm{thin}}_{\nu_i,j} \rangle \cdot \Delta L_{\nu_i,j}(s^+)}{\sum_{j \in V} \Delta L_{\nu_i,j}(s^+)} \end{aligned} \tag{2.56}$$

Here the summations in the numerator go over all rays j which are emitted from cells inside ($\tau_{\nu_i} > 2/3$) or outside ($\tau_{\nu_i} < 2/3$) the neutrinosphere, and the one in the denominator over the whole volume.

3. Astrophysical test applications: cooling PNS & BH-torus systems

3.1. Snapshot calculations of a cooling proto-neutron star

In order to asses the quality of our new ILEAS code, we need to test it against more sophisticated transport schemes and in different regimes. Given that our ultimate goal is the application of ILEAS in the context of NS mergers, cooling PNS's present a relevant test scenario. At the explosion of a massive star in a SN, its core contracts to high densities and temperatures, giving birth to a young NS. The hot, dense interior of the newly formed PNS is a perfect representation of an optically thick regime where the diffusion treatment can be tested. Additionally, the star is surrounded by a less dense envelope, where absorption of the neutrinos emitted from the NS's surface will apply. In between, the transition region around the neutrinosphere poses the most challenging conditions for treatments based on an interpolation of diffusive and free streaming regimes, such as in our ILEAS method.

We apply our scheme to several snapshots from a hydrodynamical simulation performed by Hüdepohl et al. (2010), who used the 1D PROMETHEUS-VERTEX code[1]. We take the hydrodynamical and thermodynamical data at different times post bounce from the model labelled Sr (reduced opacities), and map it to our 3D Cartesian grid. The motivation behind the chosen model is the similarity of our opacities and production reactions with the ones included in the original setup. Figure 3.1 shows the density, temperature and electron fraction profiles of the corresponding snapshots.

For the sake of more detailed comparisons, we also employed the M1 scheme ALCAR (Just et al., 2015b) to calculate the neutrino luminosities from one of the snapshots (0.5 s). Starting the evolution from a previous timestep (0.4 s post-bounce) of the VERTEX simulation and evolving it for 0.1 s, ALCAR was able to reproduce the results of VERTEX with remarkable accuracy. We use this evolved ALCAR background (at 0.5 s post-bounce) as well for our direct, detailed comparison of the results obtained by ILEAS and ALCAR. The neutrino interactions employed by both schemes for the tests are summarized in table 3.1. We must point out, that the prescriptions for ν_x production rates (pair processes and bremsstrahlung) differ between both codes, so a bigger disagreement is to be expected in the luminosities

[1]This cooling PNS is the remnant of a 8.8 $M_\odot$(ZAMS) electron capture SN.

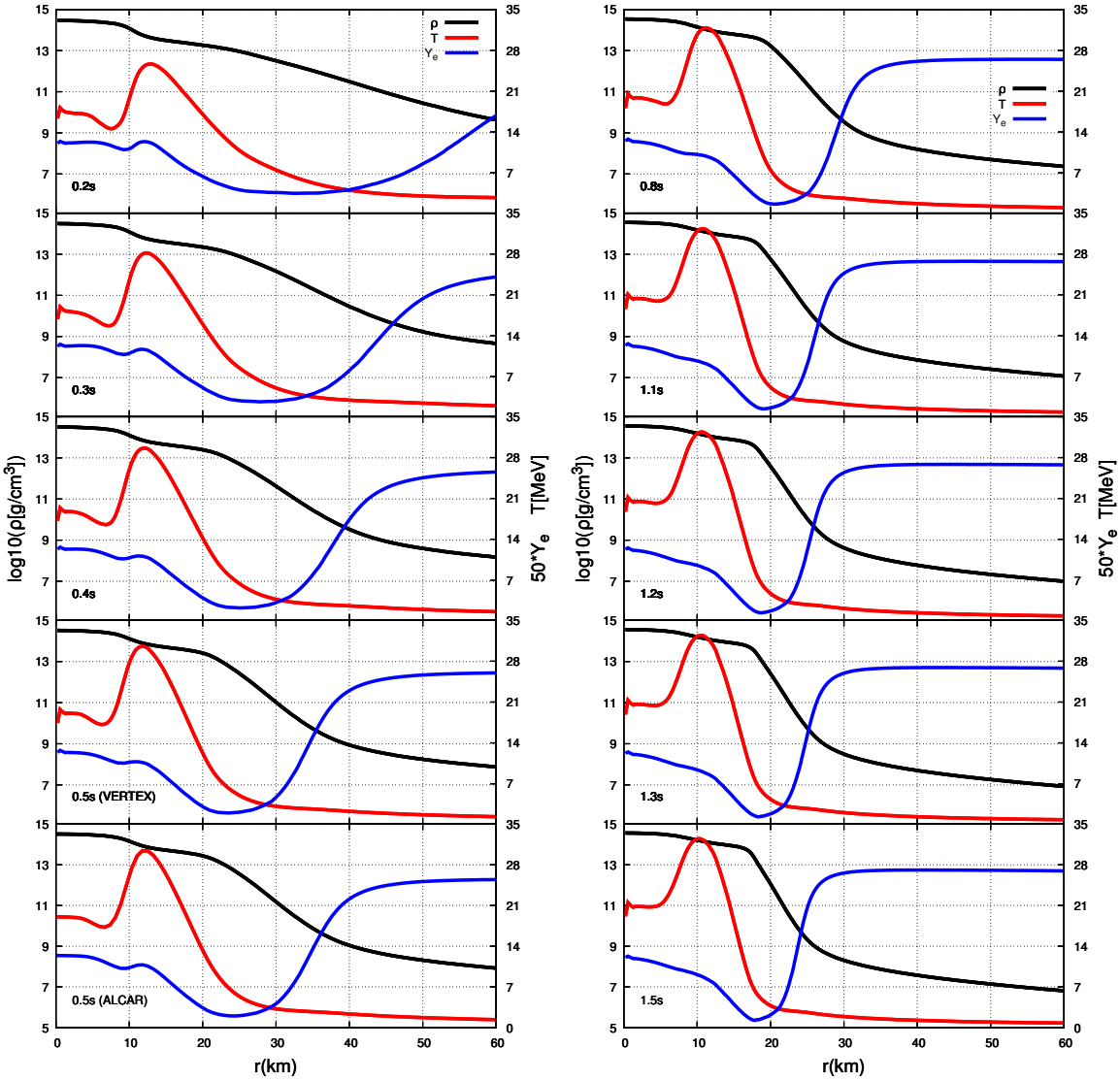

Figure 3.1.: Hydrodynamical/thermodynamical profiles (density black, temperature red and electron fraction blue) of the different PNS snapshots employed in section 3.1. Post-bounce times of the profiles are specified in the left lower corner of the panels.

Table 3.1.: Neutrino interactions employed in section 3 for our tests with the ILEAS code in comparison to ALCAR calculations.

Name	Interaction	ν species
β-react. for ν_e	$p + e^- \leftrightarrow n + \nu_e$	ν_e
β-react. for $\bar{\nu}_e$	$n + e^+ \leftrightarrow p + \bar{\nu}_e$	$\bar{\nu}_e$
$e^- e^+$ annihil.	$e^- + e^+ \rightarrow \nu_i + \bar{\nu}_i$	ν_x
N-N brems.	$p + n \rightarrow n + p + \nu_i + \bar{\nu}_i$	ν_x
Nucleon sct.	$N + \nu_i \rightarrow N + \nu_i$	ν_e, $\bar{\nu}_e$ & ν_x

of these heavy-lepton neutrinos (see Rampp and Janka 2002 and appendix B for the exact definitions of the rates employed by ALCAR and ILEAS, respectively). Finally, some differences will unavoidably arise from the fact that ILEAS is in essence a grey scheme while ALCAR is fully energy dependent.

As a foreword to the comparison, it is important to note that there are still some essential differences between ALCAR and the standard formulation of ILEAS in the derivation of the neutrino production rates. The former calculates the rates for β-production of ν_e and $\bar{\nu}_e$ from a formulation that ensures detailed balance, based on blocking corrected absorption opacities, κ^*, defined in equations (B.2) and (B.3), following Rampp and Janka (2002). On the other hand, ILEAS employs the emissivity, j_{ν_i}, defined as in equations (C.4) and (C.6) (Bruenn, 1985), to compute the rates. In appendix C we show the derivation of the rates in both schemes, and provide a detailed comparison of the effects of each prescription on the neutrino luminosities. In order to show a more accurate comparison, ILEAS employs the prescription of the β-production rates from ALCAR in the results shown in this section, with the same energy binning described in section 2.3.1.

Figures 3.2 and 3.3 show the luminosity profiles of each neutrino species obtained by ILEAS for the selected time snapshots from the VERTEX simulation, in comparison to the original transport results. In the bottom panels of figure 3.2 we present the results obtained on the background evolved with ALCAR, where the results obtained by both transport codes are also plotted for comparison. Note that in this panel, for a better comparison with ALCAR, we do not include redshift in the calculations with ILEAS. In order to obtain these results, we have relaxed the background using ILEAS to adjust the temperature and electron fraction to their new steady-state values. After a brief transient of a few ms, all quantities settle into a quasi-stationary state. We will discuss the details of the scheme employed for relaxation as well as the longer time evolution of one of these snapshots in section 3.3.

In all the tested snapshots, from 0.2 s to 1.5 s post bounce, ILEAS is able to reproduce the transport results for ν_i and $\bar{\nu}_i$ with better than 10 per cent accuracy.

The slightly bigger discrepancies for ν_x are very likely associated with the different prescriptions of nucleon bremsstrahlung employed by the different codes.

The performance of ILEAS in the optically thick region is remarkable, especially for the ALCAR background, in which both codes use exactly the same opacities. The good agreement arises from the prescription of our diffusion time-scale, which is derived from an energy integration of the zeroth-order moment of the transport equation. This effectively translates in a local source term calculated as $Q^-_{\nu_i} \simeq -\int_0^\infty \boldsymbol{\nabla}\cdot\boldsymbol{F}_{\nu_i}\mathrm{d}\epsilon$, which, in the case of quasi-stationarity, $\partial E_{\nu_i}(\epsilon)/\partial t \sim 0$, is essentially the same result as with ALCAR. As we approach the semitransparent region, however, the results start to differ slightly due to the deviations from β-equilibrium of the neutrino spectrum, which we approximated by our interpolation of the neutrino degeneracies (equation 2.25). This is one of the most delicate regimes for our scheme, as the diffusion time-scale depends strongly on the neutrino spectrum, which cannot be properly determined by a leakage method. Finally, in the optically thin regime, our 3D absorption model successfully captures the essential features of energy and lepton deposition in the PNS envelope. This is visible from a very good agreement of the $Y_e(r)$ profiles obtained with ILEAS and ALCAR/VERTEX, respectively (figure 3.4). In section 3.2 we will discuss in further detail the features of our 3D absorption scheme, in the context of a BH-torus system.

In the profiles of $\bar{\nu}_i$ and ν_x, negative luminosities can be observed at around 10 km for the transport schemes. They are the result of a net neutrino flux directed towards the centre of the PNS, i.e. neutrinos in this region diffuse inward. Because ILEAS is unable to reproduce such an effect by construction, the diffusion time-scale in those regions, which would become negative, is set to infinity, preventing any leak of neutrinos out of the star[2].

It is interesting to note the small differences in the relaxed electron fraction profile. Figure 3.4 shows the original profile from the 0.5 s PNS snapshot evolved by VERTEX in comparison with the profiles obtained by ALCAR, and the one further relaxed using ILEAS. It catches the eye that there is a consistent shift of the low Y_e region, corresponding to the PNS surface, to slightly larger radii for the ILEAS model. In fact, this effect is generic because of the inability of any leakage scheme to accurately model the semitransparent regime, regardless of the absorption or equilibration parts, as can be seen by our test results obtained with other definitions of the diffusion time-scale, summarized in appendix A. Tentatively, a better handle on the neutrino spectrum out of equilibrium could mitigate this effect. However, we emphasize that our implementation of ILEAS with its novel definition of the diffusion timescale is performing extremely well compared to results shown from other schemes used in the literature (Perego et al., 2016).

Table 3.2 lists a summary of the luminosities and mean energies of the three neutrino species, as seen by a local observer in the rest frame of the neutrino source at the edge of our grid, $\sim$ 100km, obtained by ILEAS for all our tested conditions, in comparison to the original results obtained by the corresponding transport codes.

[2]See section 2.3.1 for details on the treatment of negative time-scales.

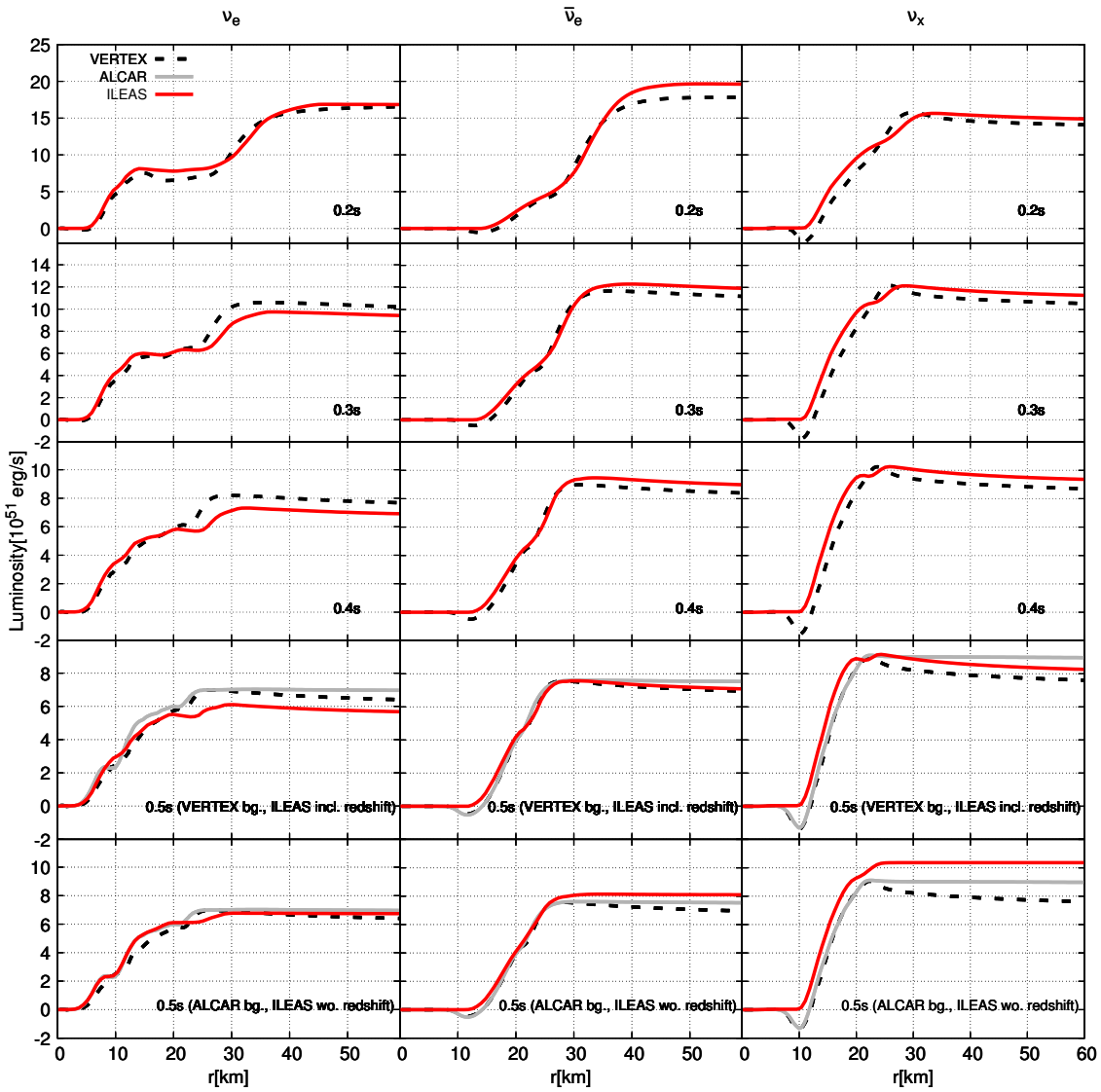

Figure 3.2.: Integrated neutrino luminosity profiles obtained by ILEAS on a stationary background for ν_e, $\bar{\nu}_e$ and ν_x, as measured in the local frame at each radius r, compared to the results of more sophisticated transport schemes. Snapshots are taken from the results of PNS cooling simulations by Hüdepohl et al. (2010) at different post-bounce times, which are noted in the lower right corner of each panel. The temperature and Y_e profiles were relaxed for 5 ms with ILEAS to obtain stationary results. The 'transport (VERTEX)' results shown are the original luminosities from the source model, and for the case at 0.5 s, we also show the results obtained by the moment scheme ALCAR (Just et al., 2015b) on the same snapshot. The bottom row of plots shows the results of ILEAS obtained on the background adopted from ALCAR instead of directly using the output of the VERTEX simulation. We caution the reader that the ALCAR luminosities, as well as the ones obtained by ILEAS on the ALCAR background (bottom row), do not include gravitational redshift.

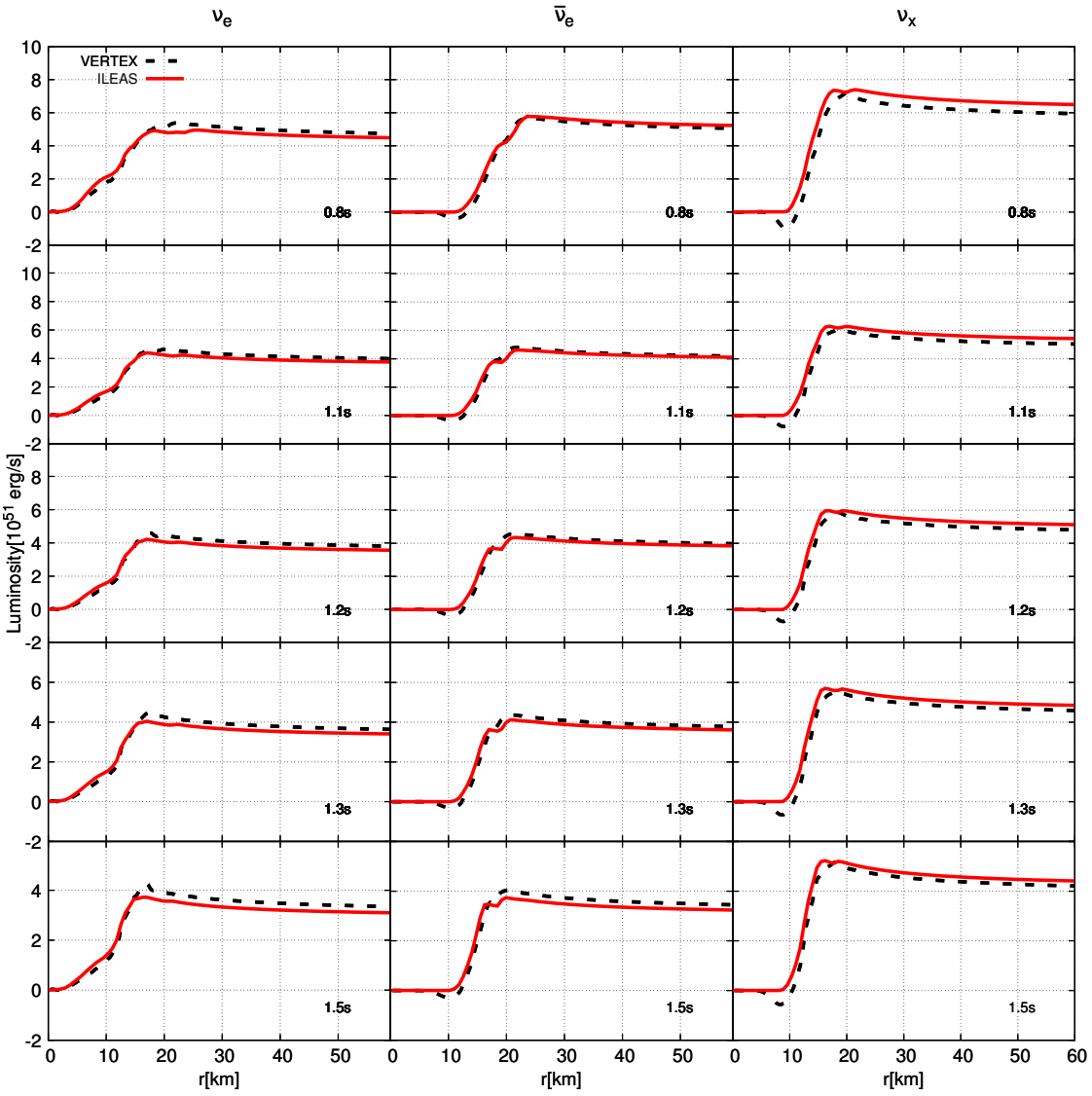

Figure 3.3.: Integrated neutrino luminosity profiles obtained by ILEAS on a stationary background for ν_e, $\bar{\nu}_e$ and ν_x, as measured in the local frame at each radius r, compared to the results of more sophisticated transport schemes. Snapshots are taken from the results of PNS cooling simulations by Hüdepohl et al. (2010) at different post-bounce times, which are noted in the lower right corner of each panel. The temperature and Y_e profiles were relaxed for 5 ms with ILEAS to obtain stationary results. The 'transport (VERTEX)' results shown are the original luminosities from the source model.

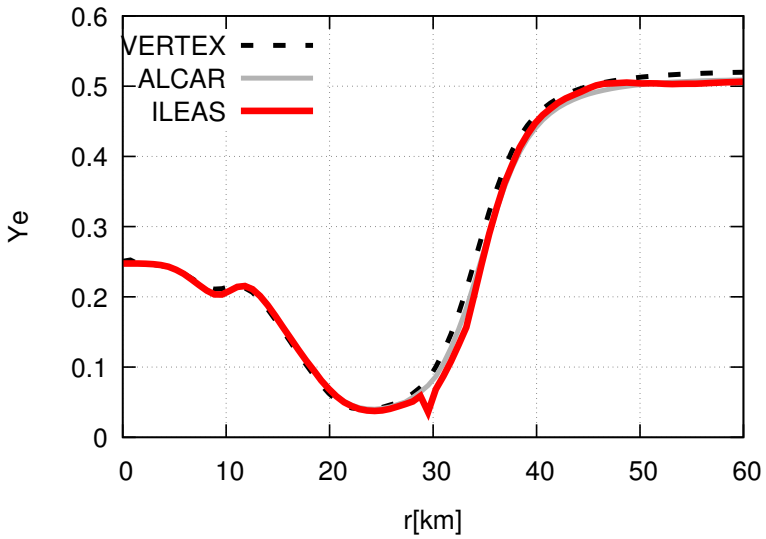

Figure 3.4.: Electron fraction profile after 5 ms of relaxation obtained by ILEAS applied to the 0.5 s PNS snapshot from ALCAR. We show for comparison also, the Y_e profiles of the VERTEX and ALCAR simulations.

All ILEAS results are extracted after a few milliseconds of relaxation, employing the formulations described in section 2.6. As mentioned earlier, the neutrino luminosities obtained by ILEAS for all tested PNS snapshots provide a very good approximation of the luminosities obtained by the transport calculations. The mean neutrino energies calculated in the leakage approach, however, exhibit a greater disagreement with the transport results, especially for the ν_e case. As we already pointed out in section 2.6, this is a natural consequence of the leakage ansatz (equation 2.52), which ignores the thermalization of neutrinos produced at high optical depths on their diffusive propagation to the neutrinosphere. Considering the neutrino luminosity profiles in figures 3.2 and 3.3, it is easy to understand that ν_e, which are emitted from deeper inside the PNS, will be most affected by this shortcoming. To ease this deficiency, we provide the approximate diagnostic mean energies defined by equation (2.56). We find that, as expected, these post-processed energies dramatically improve our mean energy estimates for ν_e, with just moderate corrections for $\bar{\nu}_e$, providing an agreement below typically ~ 15 per cent (~ 1.5 MeV difference in the worst case). The larger differences observed in the ν_x mean neutrino energies stem from the different prescription of bremsstrahlung employed by ILEAS,ALCAR and VERTEX.

3.2. Snapshot calculations: black hole-torus system

In order to assess the performance of our scheme on a possible remnant of a CO merger, we calculate the neutrino luminosities for two different BH-torus systems

evolved previously using the ALCAR code (Just et al., 2015b). The neutrino reactions employed for the BH-torus systems are the same as for the PNS (table 3.1), except for heavy lepton neutrinos, which are switched off in both calculations.

In table 3.2 we also include the neutrino luminosities and mean energies for each neutrino species as obtained by ILEAS, applied to two BH-torus systems. Because tori are optically thinner than PNS's, their cooling time-scale is much shorter, and the temperature can change considerably during the relaxation of the background. We took that into account by providing the results of both ALCAR and ILEAS after 3 ms, with respect to the original snapshots. Even though we also provide the mean energies calculated as equation (2.56), the ones obtained by the leakage approximation by equation (2.52) should be more accurate in the case of BH-torus systems, for two simple reasons. First, in the BH-torus models considered in this work, matter becomes optically thin during the relaxation (the optical depth is $\tau_{\nu_i} < 2/3$ almost everywhere after a few milliseconds of evolution) or it encloses a very small volume, so the leakage ansatz, namely that neutrinos stream away carrying their production spectrum, is a reasonable approximation. Second, the gradients in the hydrodynamical and thermodynamical quantities are considerably softer than the PNS case. Therefore, the reasoning that most absorption occurs in the production cell, which is employed to estimate the mean energies in equation (2.56), is a less accurate approximation. Because the leakage mean energies employ a more accurate description of absorption in the optically thin region, which are the absolutely dominant conditions in the tori, we advise the reader to consider the leakage mean energies for any diagnostic analysis or comparison.

Figure 3.5 shows the performance of our absorption scheme on the snapshot of a torus of $0.3M_\odot$ around a $3M_\odot$ BH. Despite the effects caused by the ray tracing approach, the qualitative resemblance between ALCAR (left) and ILEAS (right) is remarkable. M1 schemes are known to perform poorly in regions where flows cross paths, so we can draw no meaningful conclusions of the comparison in the z-axis region.

It must be noted that ILEAS assumes the flux factor to follow the simple interpolation $\langle \chi_{\nu_i} \rangle^{-1}_{\mathrm{PNS}} = 4.275\tau_{\nu_i} + 1.15$, suggested by O'Connor and Ott (2010). This is an acceptable approximation for the case of a cooling PNS, but fails to capture the geometry of the BH-torus system. More sophisticated prescriptions of the flux factor, which account for geometric effects, would certainly improve the accuracy of the absorption scheme in the area around the inner edge of the torus. However, such improvement is beyond the scope of this work, and we consider the obtained results with the presented approximations as satisfactory.

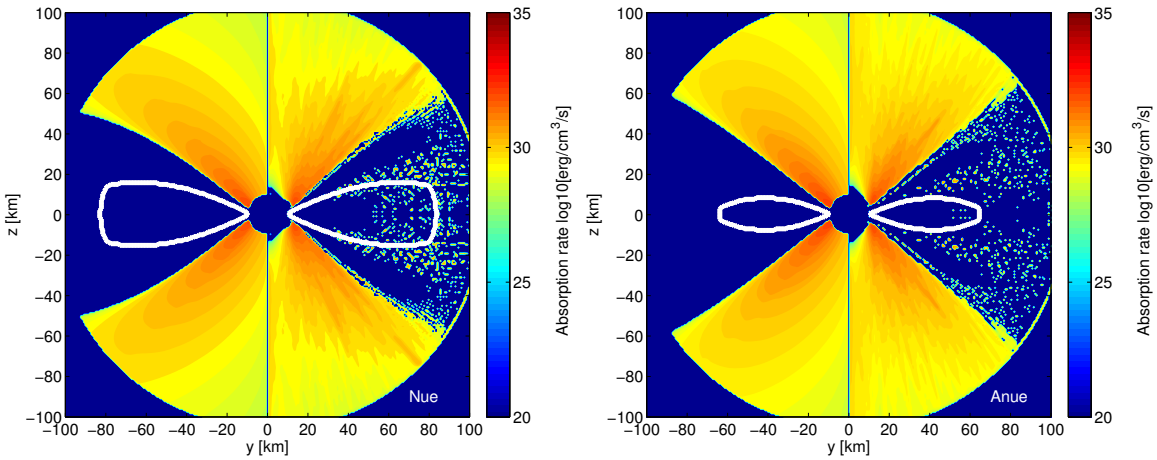

Figure 3.5.: Results of our neutrino absorption scheme for an $0.3M_{\odot}$torus around a $3M_{\odot}$ BH, left: for ν_e, right: for $\bar{\nu}_e$. Colour coding displays the absorption dominated region, where the net neutrino rate $Q_{\nu_i,\mathrm{tot}} = Q^{+}_{\nu_i} - Q^{-}_{\nu_i}$ is positive. The left half of each panel shows the results obtained by the ALCAR scheme, while the right ones are the results with ILEAS. The white contour depicts the neutrino surface, where $\tau_{\nu_i} = 2/3$.

Table 3.2.: Neutrino luminosities and mean energies obtained by ILEAS applied to several snapshots of a PNS cooling simulation at different times and two BH-torus models, in comparison to the results from transport calculations with different codes. All leakage quantities are computed as described in section 2.6. *Leakage mean energies* provide the mean energies calculated by equation (2.52), while *mean energies for diagnostics* are obtained via equation (2.56). All values are taken for a local observer in the rest frame of the source at the edge of the grid (100 km). ν_x luminosities refer to *each* of all four species.

Model	ν-species	Transport luminosity (10^{52} erg·s^{-1})	Leakage luminosity (10^{52} erg·s^{-1})	Transport mean energy (MeV)	Leakage mean energy (MeV)	Mean energy for diagnostics (MeV)	Transport code
PNS 0.2 s	ν_e	1.62	1.64	9.72	7.85	11.04	VERTEX
PNS 0.2 s	$\bar{\nu}_e$	1.73	1.91	12.42	12.43	12.72	VERTEX
PNS 0.2 s	ν_x	1.37	1.45	14.32	21.38	-	VERTEX
PNS 0.3 s	ν_e	0.98	0.91	9.43	7.20	10.65	VERTEX
PNS 0.3 s	$\bar{\nu}_e$	1.08	1.15	12.18	11.98	12.27	VERTEX
PNS 0.3 s	ν_x	1.02	1.10	13.80	20.14	-	VERTEX
PNS 0.4 s	ν_e	0.74	0.67	9.31	6.96	10.52	VERTEX
PNS 0.4 s	$\bar{\nu}_e$	0.81	0.87	12.00	11.88	12.30	VERTEX
PNS 0.4 s	ν_x	0.84	0.91	13.51	19.19	-	VERTEX
PNS 0.5 s	ν_e	0.62	0.55	9.26	7.11	10.58	VERTEX
PNS 0.5 s	$\bar{\nu}_e$	0.67	0.69	11.86	11.32	12.28	VERTEX
PNS 0.5 s	ν_x	0.73	0.80	13.33	18.75	-	VERTEX
PNS 0.5 s	ν_e	0.70	0.67	9.93	7.95	11.43	ALCAR
PNS 0.5 s	$\bar{\nu}_e$	0.76	0.81	13.32	12.62	13.08	ALCAR
PNS 0.5 s	ν_x	0.90	1.04	15.67	21.46	-	ALCAR
PNS 0.8 s	ν_e	0.46	0.44	9.24	7.42	10.44	VERTEX
PNS 0.8 s	$\bar{\nu}_e$	0.49	0.51	11.64	11.39	12.45	VERTEX
PNS 0.8 s	ν_x	0.57	0.63	13.02	18.07	-	VERTEX
PNS 1.1 s	ν_e	0.38	0.36	9.24	6.56	10.10	VERTEX
PNS 1.1 s	$\bar{\nu}_e$	0.40	0.40	11.45	12.54	12.64	VERTEX
PNS 1.1 s	ν_x	0.49	0.53	12.76	17.48	-	VERTEX
PNS 1.2 s	ν_e	0.37	0.35	9.24	6.16	10.02	VERTEX
PNS 1.2 s	$\bar{\nu}_e$	0.38	0.37	11.43	12.98	12.73	VERTEX
PNS 1.2 s	ν_x	0.47	0.50	12.69	17.17	-	VERTEX
PNS 1.3 s	ν_e	0.35	0.33	9.24	5.79	10.08	VERTEX
PNS 1.3 s	$\bar{\nu}_e$	0.36	0.35	11.38	13.46	12.85	VERTEX
PNS 1.3 s	ν_x	0.44	0.47	12.61	16.89	-	VERTEX
PNS 1.5 s	ν_e	0.32	0.30	9.22	5.18	10.01	VERTEX
PNS 1.5 s	$\bar{\nu}_e$	0.33	0.32	11.27	14.26	12.88	VERTEX
PNS 1.5 s	ν_x	0.41	0.43	12.43	16.46	-	VERTEX
BH-torus 0.3 $M_\odot$	ν_e	2.33	2.15	12.13	12.66	13.76	ALCAR
BH-torus 0.3 $M_\odot$	$\bar{\nu}_e$	1.84	1.67	14.97	15.89	16.56	ALCAR
BH-torus 0.1 $M_\odot$	ν_e	0.65	0.65	12.02	12.69	13.65	ALCAR
BH-torus 0.1 $M_\odot$	$\bar{\nu}_e$	0.52	0.48	14.20	14.50	14.79	ALCAR

3.3. Time evolution of a proto-neutron star and two black hole-torus systems

In order to test the performance of our scheme in evolving systems and to relax the thermodynamical background we have attached ILEAS to a simple time evolution scheme. As we want to focus on the radiation field, we only evolve the temperature (via the fluid energy density, $E_{\rm fluid}$) and the electron fraction, keeping the matter density fixed and ignoring the velocity terms[3].

We can calculate the changes in the electron fraction from the advection equation as,

$$\left(\frac{\mathrm{d}Y_e}{\mathrm{d}t}\right)_{\rm source} = \frac{R_{\rm tot}}{A\rho}, \tag{3.1}$$

where $R_{\rm tot}$ is given in equation (2.16) and A is the Avogadro constant. For the fluid energy density, following the first law of thermodynamics for a quasi-static system with fixed density, we can express its evolution equation as,

$$\left(\frac{\mathrm{d}E_{\rm fluid}}{\mathrm{d}t}\right)_{\rm source} = Q_{\rm tot}, \tag{3.2}$$

where $Q_{\rm tot}$ is given in equation (2.15). We solve these simple equations explicitly with a forward integration, allowing for changes on either quantity of up to 2 per cent in a single timestep. Then, we only need to call the EoS to obtain the temperature from the energy, density and Y_e (via bisection) and then the chemical potentials, which we use in the next leakage step. We also include equilibration as described in this paper.

We initialize the system by computing the fluid energy density and chemical potentials from the EoS using the density, temperature and electron fraction from the initial snapshot, then calculating the equilibration surfaces and initializing the lepton fractions in their pertinent regime. The results obtained by ALCAR shown in this section were obtained by evolving only the temperature and the electron fraction in a similar fashion.

Figure 3.6 displays the time evolution of the neutrino luminosities for the PNS snapshot relaxed by ALCAR (0.5 s post bounce). The time axis starts at the time of the original snapshot, where the evolution is started. After a brief transient of a few milliseconds, the electron fraction and the temperature relax to their equilibrium values, and the system slowly evolves in a quasi steady state. The results listed in table 3.2 correspond thus to the results of the plot at 5 ms. ILEAS is capable of reproducing the results obtained by ALCAR with ~ 10 per cent accuracy throughout the 50 ms simulated.

It is important to note that, in the BH-torus models, the unavoidable transient which occurs when switching on ILEAS, proceeds to swiftly cool the optically thin

[3]Which are anyway small for the tested scenarios.

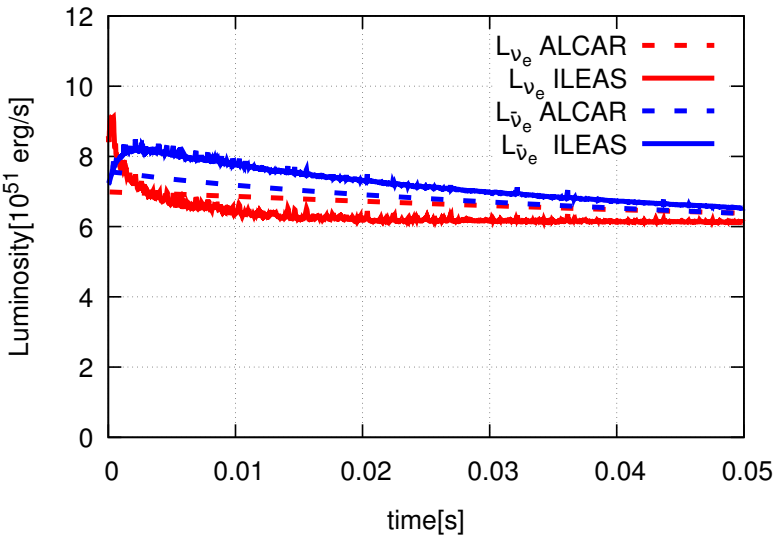

Figure 3.6.: Time evolution of the neutrino luminosities obtained by ILEAS and ALCAR as seen by a local observer in the rest frame of the neutrino source at the edge of our grid (100 km), produced by a cooling PNS with fixed density background, but evolved T and Y_e profiles. The starting time corresponds to the relaxed ALCAR snapshot discussed in section 3.1 (0.5 s post bounce).

disk before a stationary state can be reached. The natural consequence is, therefore, that the ILEAS luminosities become smaller than those obtained by ALCAR, whose background remains hotter. Nevertheless, the results obtained by ILEAS agree to less than 10 per cent with the ones obtained by ALCAR, as can be seen in figure 3.7. Note that these plots start at the time of the original snapshots from where the time evolution is started. Therefore, the results listed in table 3.2 correspond to the results of the plots at 3 ms.

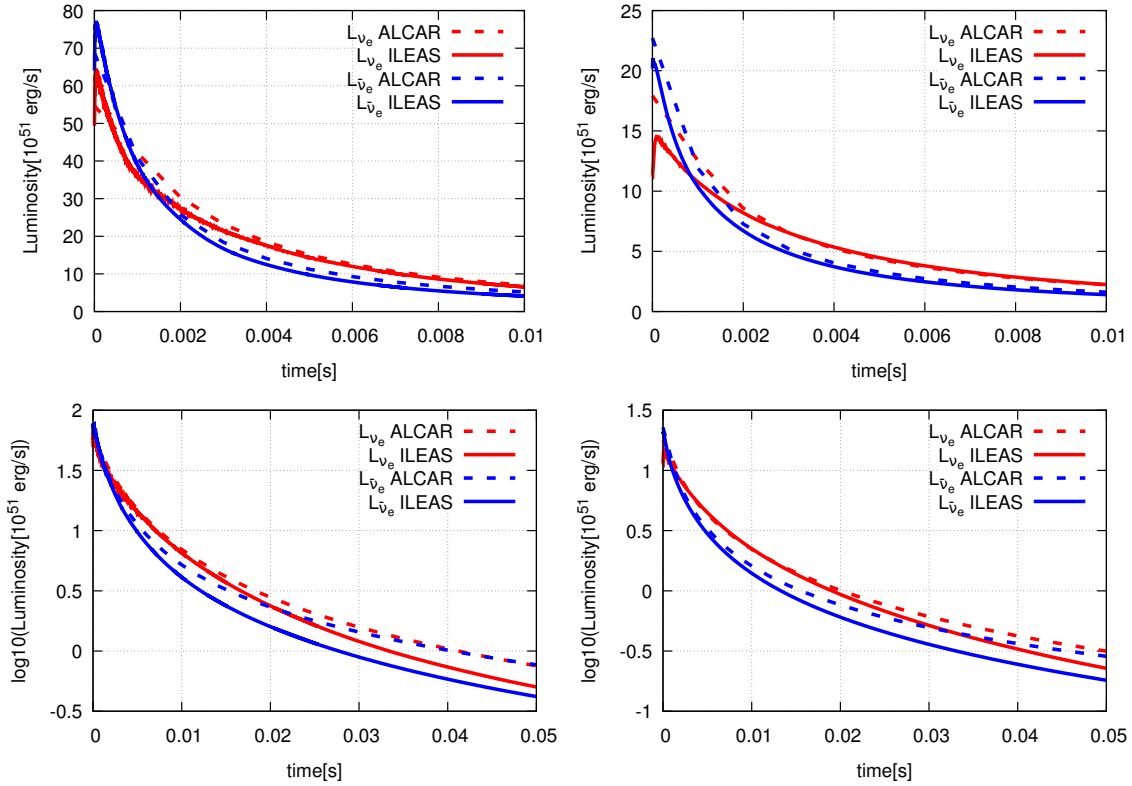

Figure 3.7.: Time evolution of the neutrino luminosities obtained by ILEAS and ALCAR as seen by a local observer in the rest frame of the neutrino source at the edge of our grid (100 km), produced by a thick ($0.3M_\odot$, left) and thin ($0.1M_\odot$, right) BH-torus around a $3M_\odot$ BH. The top panels show the first 10 ms of evolution, while the bottom ones show the full duration of the simulation on a logarithmic scale for better visibility.

4. Binary neutron-star mergers

4.1. Systematics of merger dynamics, the remnant and the ejecta

NSs in a binary system interact as gravitational point sources, slowly radiating away orbital momentum in the form of GWs and inspiraling closer together. It is not until the last few orbits before merger, that the tidal forces between both stars begin to have an impact on the evolution of the system. In the standard scenario, at this stage the orbit is quasi-circular due to the GW emission and long delay time between the formation of a NS binary and the final merger. Furthermore, the NS spin frequencies prior to merger are expected to be low compared to the orbital velocity[1] (Bildsten and Cutler, 1992; Kochanek, 1992). The details of the merger dynamics are, then, determined mainly by the EoS of NS matter and the masses of both COs.

Out of the ~ 10 known NS binaries, all have been measured to have a total mass of $\sim 2.7 \pm 1\ M_\odot$ and most of them a mass ratio, $q = M^1_{\rm NS}/M^2_{\rm NS}$, of approximately unity (Lattimer, 2012; Lattimer). This bias towards symmetric systems of such mass has puzzled scientists for some time, and there is no clear conclusion about the possible existence of a *natural selection effect*. However, some years ago, the masses of an asymmetric system were precisely measured, proving that asymmetric binaries are still a significant fraction of NS binaries (Martinez et al., 2015). As can be seen in figure 4.1, mass asymmetry has a strong impact on the dynamics of the merger, and thus on the ejecta and torus masses. The panels on the left column show different stages of the numerical simulation of a symmetric merger, where both NS have a mass of $M_{\rm NS} = 1.35\ M_\odot$, while the ones on the right display an asymmetric merger of a $M_{\rm NS} = 1.20\ M_\odot$ and a $M_{\rm NS} = 1.60\ M_\odot$ NSs. In both simulations the same EoS (DD2) was employed. In symmetric mergers (left), the two NSs deform in a tear-like shape in the tidal field of their companion, until their tips collide violently, and the two stars merge. Material is squeezed out from the collision interface, becoming unbound or settling in an accretion disk around the newly formed central object. Some of this material joins the expanding outer regions of the tidally deformed NSs, creating two small spiral arms that wind around the central object. In contrast, in the asymmetric merger case (right) the lighter NS gets disrupted by the tidal field of the heavier companion, building an elongated tidal tail which ends up as a massive

[1] However, in globular clusters the high degree of interaction between stars likely contributes to form binaries with rapidly spinning NSs, as well as mergers wit an eccentric orbit (e.g. Grindlay et al. 2006).

torus surrounding the HMNS. Albeit the two NSs still collide violently as in the symmetric scenario, the redistribution of angular momentum along the tail also aids the release of more tidal ejecta than in the symmetric case. Note that in figures 4.1 and 4.3 we define the time of the merger (0 ms) at the moment when the lapse (the metric function α, see section 2.1) reaches its minimum value, which is a common approach in the NS merger simulation community.

For the most favored configurations[2], the remnant of a NS merger is expected to be a differentially rotating HMNS surrounded by a thin torus of NS material. However, the lifetime of this central HMNS is highly dependent on the binary properties and the EoS of NS matter, ranging from the direct collapse to a BH to a long-lived super massive NS (SMNS) or even a stable one (see below). During the merger, some material also becomes unbound, ejected from the collision interface and the tidal tails of the deformed NSs, referred to as *dynamical ejecta*. In a longer timescale, neutrino driven winds and viscosity driven ejecta can also arise from a long lived remnant and the surrounding torus, which we dub *torus ejecta*.

The EoS determines which is the maximum mass a stable NS can sustain, $M_{\rm max}$, before the nuclear pressure cannot counterbalance the gravitational pull, and the star collapses to a BH. For a given EoS, the total mass of the system decides, thus, the final fate of the merger remnant. However, right after merger, the newly formed HMNS will retain the angular momentum from the progenitor NS binary, and the centrifugal forces can temporarily prevent the collapse, even with a remnant mass above $M_{\rm max}$. Hydrodynamic instabilities, magnetic fields and GWs, redistribute and radiate away angular momentum from the differentially rotating HMNS, eventually reaching a stage of rigid rotation, known as super massive NS (SMNS). During all this process, the centrifugal forces gradually reduce, and the star will collapse if they are not strong enough to aid the nuclear pressure against gravity. For very low mass NS binaries, it is in principle possible to form a stable NS as merger remnant, if the final remnant mass is below $M_{\rm max}$. Figure 4.2 shows these evolution paths in a schematic way.

During the merger, an accretion disc is formed around the central remnant, originated from the tidal tails of the deformed NSs as well as some of the material squeezed out from the collision interface. Consequently, the amount of mass comprised in this accretion disc depends on the size of these tidal tails, which are related to the deformability of the NSs. They key quantity which determines the amount of deformation a NS of a given mass suffers in the tidal field of its companion is the compactness, $C_{\rm NS}$, which relates to the NS radius and mass by

$$C_{\rm NS} \;=\; M_{\rm NS}/r_{\rm NS}, \tag{4.1}$$

and is characteristic of a given EoS. Soft[3] EoS, yield more compact NSs, which are more resilient to tidal deformation, while larger NSs are the product of stiffer EoS,

[2]Based on theoretical and observational considerations

[3]The terms *soft* and *stiff* in the context of EoS on NS matter, make reference to the slope of the pessure as a function of the matter density, $p(\rho)$. In softer EoS, pressure builds up slower with increasing density, thus producing more compact stars, and viceversa.

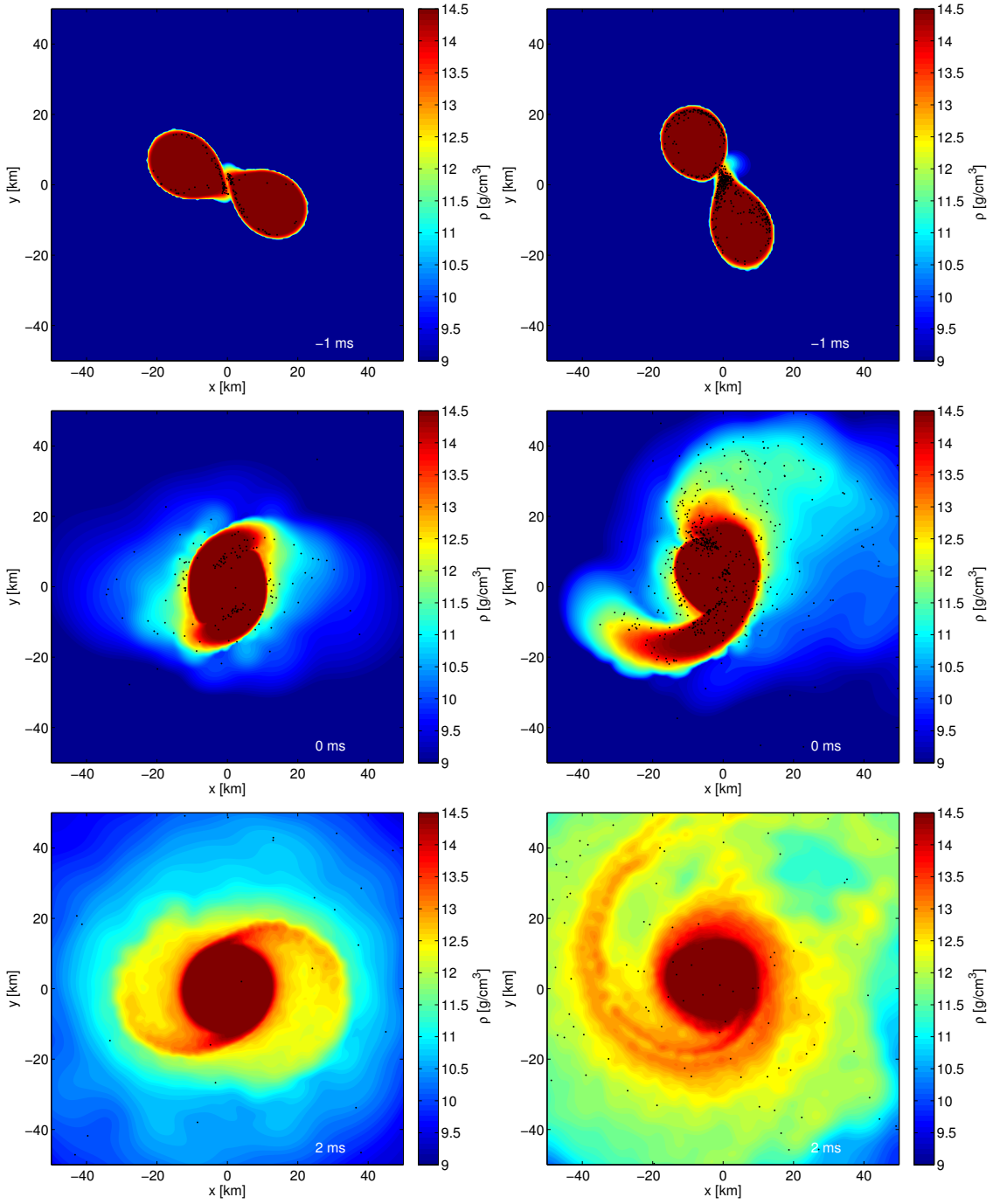

Figure 4.1.: Dynamics of the merger of two symmetric NSs of $M_{\rm NS} = 1.35\ M_\odot$ (left) and two asymmetric NSs of $M_{\rm NS} = 1.20\ M_\odot$ and $M_{\rm NS} = 1.60\ M_\odot$ (right), both employing the DD2 EoS. From top to bottom, each panel represents: the instant of first contact of the two stars (~ 1 ms), the moment of the minimum lapse (0 ms) and 2 ms after the merger. The time which is plotted in the lower right corner of every picture, is normalized to the merger time, when the lapse reaches its minimum value. Color-coded, the logarithm of the rest-mass density is plotted (in g/cm^3). The black dots represent some of the particles that will eventually be ejected, tracing the origin of the ejected material. The visualization tool SPLASH was used to convert SPH data to grid data (Price, 2007).

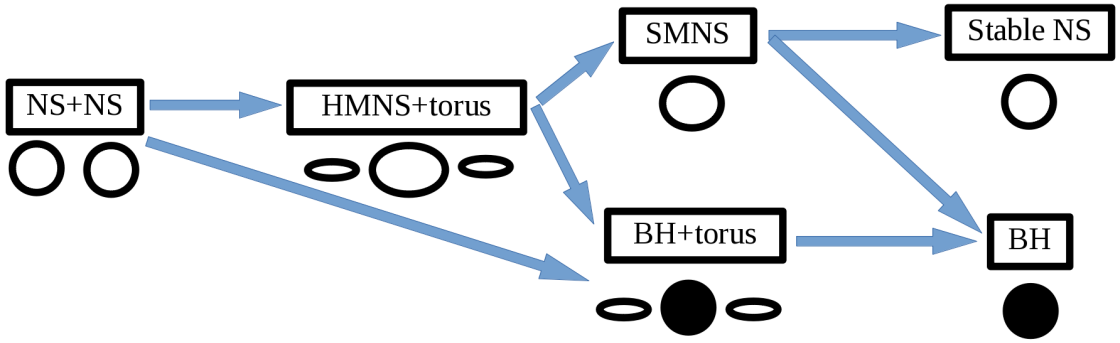

Figure 4.2.: Evolution paths for a binary NS merger. Picture inspired by the one found in Just et al. (2015a)

more prone to be deformed by strong tidal fields. Therefore, more massive tori are expected to form for low compactness (stiffer) EoS.

The compactness of a NS also determines the amount of material dynamically ejected during the merger. Soft EoS provide more compact stars, which are able to inspiral to closer orbits, producing more violent collisions and ejecting more material. Their tidal tails however, are small, and the ejecta contribution from this source is negligible. Stiff EoS, on the contrary, yield larger NSs which can get severely deformed before collision. As a consequence, more material is stripped from the tidal tails, albeit the ejecta component from the collision interface is still the dominant one. Because most of the material is ejected from the collision interface between the merging NSs regardless of the compactness, soft EoS produce, overall, a larger amount of ejecta. Figure 4.3 illustrates this dependency on the EoS with two symmetric mergers of two NSs with a mass $M_{\rm NS} = 1.35\ M_\odot$ employing a soft EoS (SFHo, left) and a stiffer one (TM1, right). In appendix (E) we show the mass-radius relations of the EoS employed in this work.

4.2. Neutrinos in binary neutron-star mergers

4.2.1. Impact of ILEAS' modules on the composition of neutron-star merger's ejecta

As we described in section 2, ILEAS is composed of three modules which reproduce different aspects of neutrino interactions with matter. In this section, we want to demonstrate the importance of including all these effects for the correct reproduction of neutrino transport physics in NS mergers, focusing on how each module individually impacts the electron fraction of the ejected material. For this purpose, we set up several numerical simulations of symmetric $M_{\rm NS} = 1.35\ M_\odot$ NS mergers

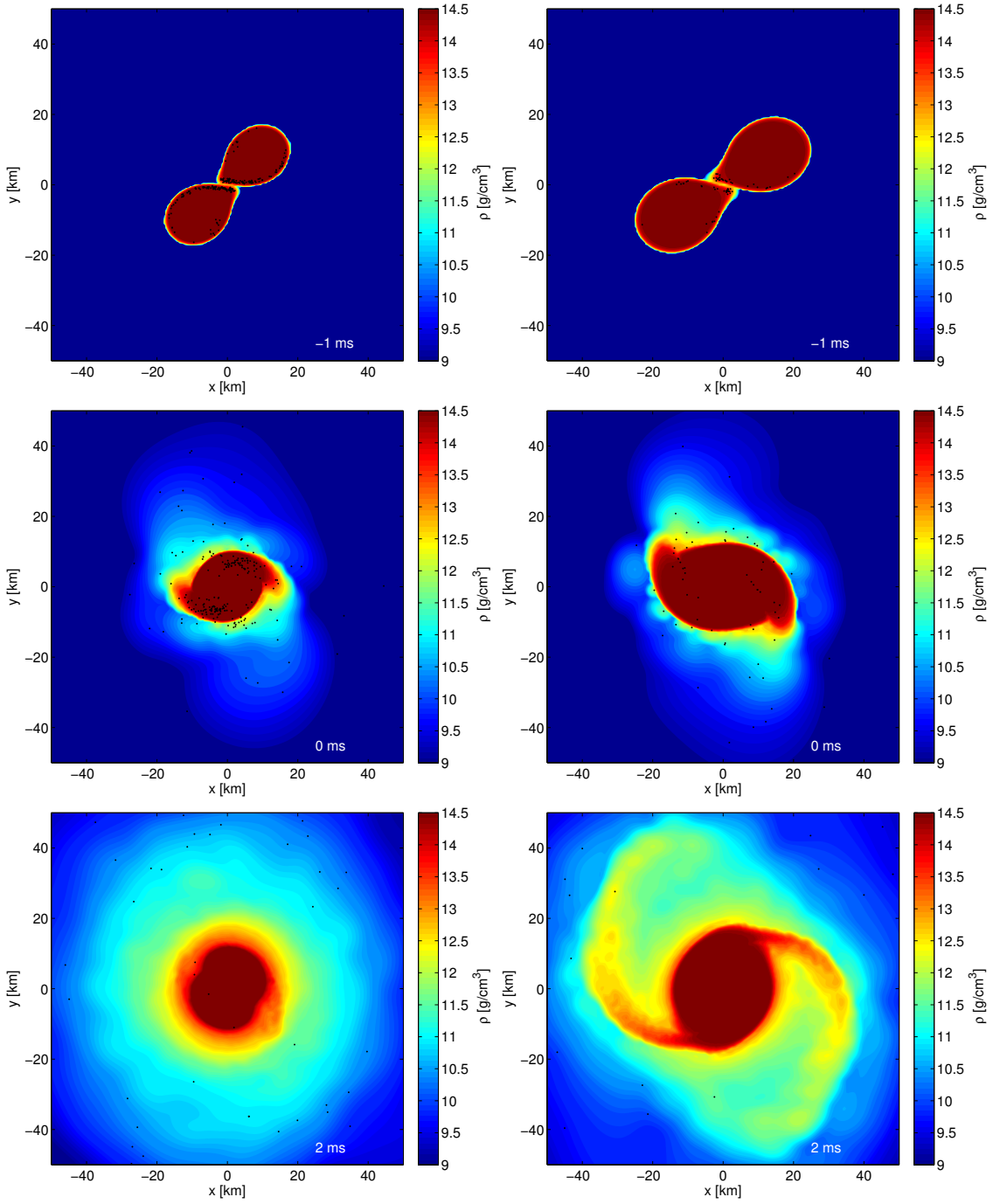

Figure 4.3.: Dynamics of the merger of two NSs of $M_{\rm NS} = 1.35\ M_\odot$ with the DD2 (left) and SFHo (right) EoS. From top to bottom, each panel represents: the instant of first contact of the two stars (~ 1 ms), the moment of the minimum lapse (0 ms) and 2 ms after the merger. The time which is plotted in the lower right corner of every picture, is normalized to the merger time, when the lapse reaches its minimum value. Color-coded, the logarithm of the rest-mass density is plotted (in g/cm^3). The black dots represent some of the particles that will eventually be ejected, tracing the origin of the ejected material. The visualization tool SPLASH was used to convert SPH data to grid data (Price, 2007).

Table 4.1.: List of numerical simulations of NS mergers performed to test the impact of the different ILEAS' modules. Each entry indicates the modules included for that simulation (*Equil* stands for Equilibration, *Leak* for leakage and *Abs* for absorption) and displays the properties of the ejected material (mass and $\langle Y_e \rangle$) extracted at 5 ms post-merger. All simulations employ the DD2 EoS and two symmetric NSs of $M_{\rm NS} = 1.35\ M_\odot$.

Merger Model	Modules included	Ejecta mass ($10^{-3}\ M_\odot$)	Ejecta $\langle Y_e \rangle$
DD2_135(noν)	No ν	2.6	0.03
DD2_135(L)	Leak	1.6	0.21
DD2_135(E)	Equil	1.9	0.18
DD2_135(LA)	Leak+Abs	2.0	0.17
DD2_135(LE)	Leak+Equil	1.5	0.21
DD2_135(LEA)	Leak+Equil+Abs	1.9	0.21

with the DD2 EoS, in which we enable different combinations of ILEAS' modules[4]. The tested cases are listed in table 4.1, together with the ejecta masses and average electron fractions obtained in those simulations at 5 ms after merger.

The first feature which is worth pointing out are the relevant differences in the amount of material ejected during the merger for the different setups. On the one hand, the inclusion of the effects of weak interactions, either in the form of equilibration in optically thick conditions or neutrino energy and lepton losses by means of a leakage treatment, reduces the amount of unbound material by up to $\sim 25 - -40$ per cent, from $M_{\rm ej} = 2.6\ M_\odot$ (without neutrino interactions included) to $M_{\rm ej} = 1.5{\cdot}10^{-3} - 1.9{\cdot}10^{-3}\ M_\odot$. This is due to the energy loss caused by neutrino emission, which is also implicitly present in the boundary treatment of the equilibration module (see section 2.5 for details). On the other hand, neutrino reabsorption helps unbind some material by depositing energy in the optically thin region, reducing the negative impact of neutrinos on the ejecta mass to < 25 per cent ($M_{\rm ej} = 1.9{\cdot}10^{-3} - 2.0{\cdot}10^{-3}\ M_\odot$).

A quick glance at table 4.1 shows that the equilibration and leakage modules both contribute to raising the average Y_e of the ejecta, increasing it even further if they are employed together. On the contrary, the impact of the absorption is not clear from the average Y_e, since it either reduces it o does not *seem* to produce any effect at all (see below).

For a more precise understanding of the impact of ILEAS' modules on the ejecta composition, we provide in figure 4.4 histograms of the Y_e distribution of the ejected

[4]Trivially, we omit the cases which imply including neutrino re-absorption without emission

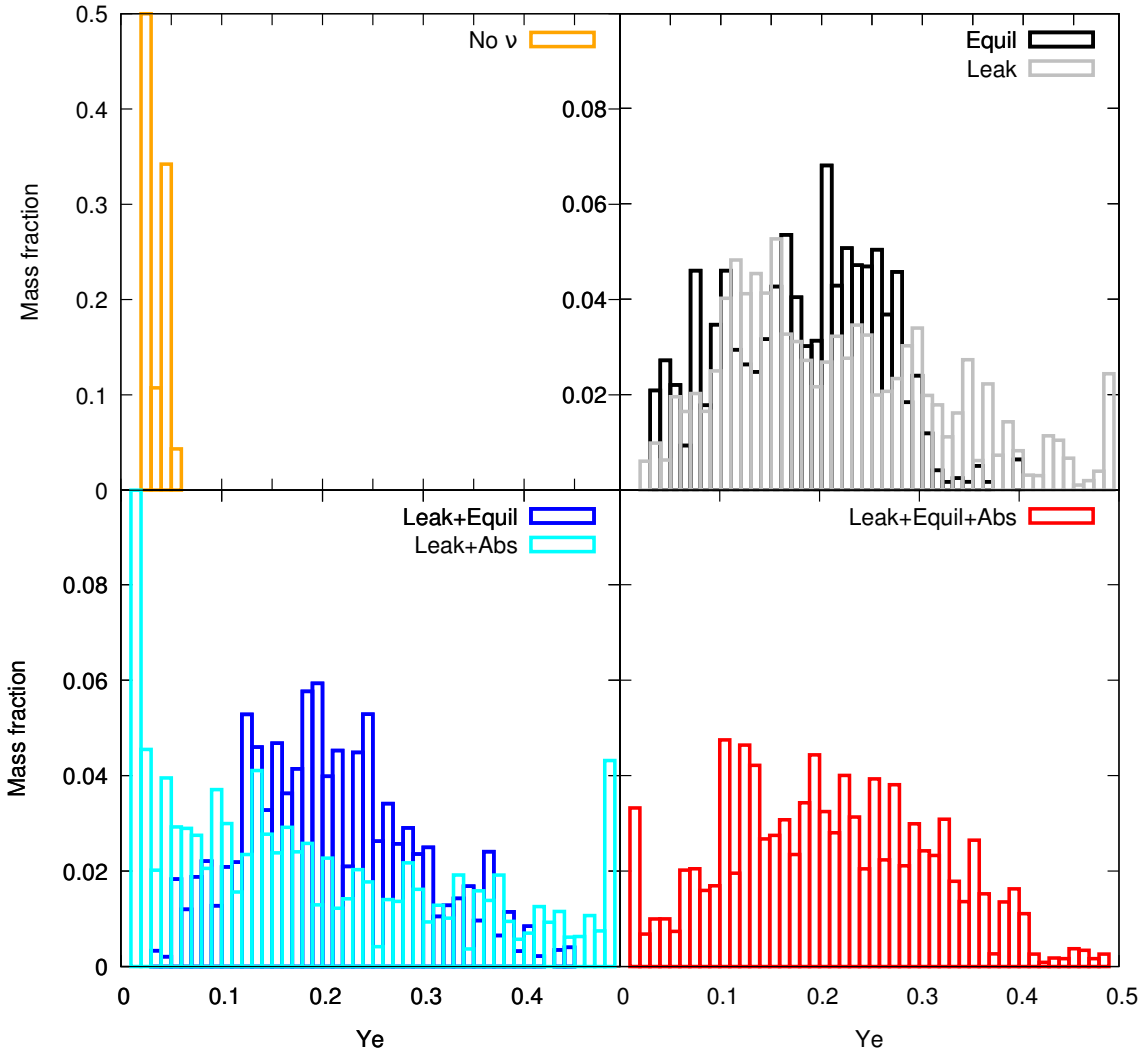

Figure 4.4.: Histograms showing the electron fraction (vs. mass fraction) of the material ejected in a symmetric merger of two NSs of $M_{\rm NS} = 1.35\ M_{\odot}$ employing the DD2 EoS. Each panel displays the ejecta obtained by a simulation of the same binary setup, but including different combinations of the ILEAS' modules to treat neutrino interactions. The top-left panel shows the results without any neutrino scheme (note the different y-axis range with respect to the other panels); the top-right panel shows the results including *only* equilibration in optically thick conditions (section 2.5) and *only* neutrino losses via leakage (section 2.3); the bottom-left panel shows both, the results with only leakage+absorption (section 2.4), where we switched off the equilibration module, and the results with only leakage+equilibration, ignoring the effects of neutrino re-absorption; and finally, the bottom-right panel shows the results including the full ILEAS scheme (leakage+absorption+equilibration).

material, normalized to the total ejecta mass. The *top-left* panel shows the ejecta Y_e distribution of a merger without weak interactions (note the different y-axis range with respect to the other panels). There, the initial cold NS matter composition is advected during the merger and, therefore, with no neutrino interactions to alter its composition, all the unbound material remains neutron rich ($Y_e < 0.05$). This configuration which ignores the impact of neutrinos leads to the synthesis of a Solar-like distribution of heavy r-process elements ($A \gtrsim 140$) in the ejecta (e.g. Bauswein et al. 2013). On the contrary, the *bottom-right* panel displays the ejecta Y_e distribution of the same setup, but includes neutrino interactions using the full ILEAS scheme. The differences are notorious, with the ejecta Y_e distributed in a *Gaussian-like* shape around the average value $Y_e = 0.21$, with some material reaching values as high as 0.5. This broad distribution of Y_e in the ejecta suggests that light r-process elements ($A \gtrsim 90$) are likely to be synthesized as well (e.g. Wanajo et al. 2014).

The *top-right* panel shows the results of the merger simulation including only the equilibration module, which, by ensuring β-equilibrium in the optically thick conditions, drives the composition of hot NS matter to less neutron rich values. On the same panel, we include the Y_e distribution of the ejecta obtained by the simulation which includes only the leakage module. As expected, the Y_e increases due to the dominant emission of $\bar{\nu}_e$ from neutron rich NS matter (equation 1.4). The two effects, equilibration and neutrino emission, produce a similar impact on the Y_e, albeit the leakage results present a tail spreading to higher Y_e values, while the inclusion of equilibration clusters more matter near intermediate values of the electron fraction ($Y_e \approx 0.2$).

Finally, the *bottom-left* panel displays the ejecta Y_e distribution for the cases where we use equilibration plus leakage (no absorption); and leakage plus absorption (no equilibration). The combination of leakage and equilibration modules shows the tail of unbound material with higher Y_e also present in the model including only the leakage in the top-right panel, but the bulk of matter seems more concentrated around $Y_e = 0.2$, combining the two effects described in the top-right panel. Contrariwise, the re-absorption of neutrinos emitted by the remnant spreads the Y_e distribution of the material, increasing the neutron richness of some of the ejecta, while raising the Y_e of another smaller component. However, the exact impact of the absorption is very direction-dependent and a more accurate analysis of the geometry of the ejecta is left for future work.

4.2.2. Dependence on the neutron-star masses and the equation of state

As discussed in section 4.1, the properties of NS merger ejecta are highly dependent on the EoS and the NS masses. In order to probe the parameter space of initial conditions, we performed numerical simulations with different EoSs, total masses and mass ratios. We narrowed down the array of possibilities by choosing the initial configurations of NS merger simulations published in the literature which include

Table 4.2.: List of NS merger models presented in this work, with their initial setup (NS masses and EoS) and the properties of the ejected material (mass and $\langle Y_e \rangle$) extracted at 5 ms post-merger.

Merger Model	EoS	NS masses ($M_\odot$)	Ejecta mass ($10^{-3}\ M_\odot$)	Ejecta $\langle Y_e \rangle$
DD2_135	DD2	1.35-1.35	1.9	0.21
DD2_130	DD2	1.30-1.30	1.6	0.20
DD2_120_160	DD2	1.20-1.60	7.5	0.21
SFHo_135	SFHo	1.35-1.35	2.8	0.23
SFHo_130	SFHo	1.30-1.30	2.0	0.20
TM1_135	TM1	1.35-1.35	1.1	0.14

neutrino interactions. This allows us to compare our results to those published by other groups using different schemes, which we analyze in detail in section 4.2.3. To further motivate our choice, we have selected the total mass to be approximately the one measured in the GW event, which is also the one measured in most known binary NS systems, and for the asymmetric systems, we took the most extreme mass ratio compatible with the event estimates[5] (Abbott et al., 2017f).

The EoSs we employ are SFHo, a soft EoS, DD2, a moderately stiff EoS, and TM1, a stiff EoS, all microphysical EoS which together cover the span of expected NS radii (see appendix E for a glimpse at the mass-radius relations of the EoS employed in this work). For the symmetric mergers we took the canonical mass of NSs, 1.35 $M_\odot$, and a mass of 1.30 $M_\odot$, inspired by the simulations performed in Palenzuela et al. (2015); Sekiguchi et al. (2016) and Foucart et al. (2016). Finally, to test the effects of an asymmetric mass ratio we took $q = 1.33$ (as defined in section 4.1) with NS masses of 1.6 $M_\odot$ and 1.2 $M_\odot$. Table 4.2 summarizes the initial conditions employed in the simulations presented in this work, as well as the resulting ejecta properties[6].

In section 4.1, we described how the amount of ejecta depends on the initial configuration. These trends are clearly visible in the results reported in table 4.2. In a nutshell, NS mergers with softer EoS produce more ejecta than mergers with stiffer ones, as more compact stars collide more violently. With a similar argument, a small decrease in the NS masses has a noticeable reduction on the amount of ejected material in the merger and, in asymmetric mergers, the tidal disruption of the lighter NS produces much more ejecta than in the symmetric case (see figures

[5]Under the assumption of irrotational NSs

[6]The merger model name is composed of the EoS name (DD2, SFHo or TM1) the mass of the lighter star (in 100$\cdot\ M_\odot$) and the mass of the heavier star (if absent, both stars have the same mass).

4.1 and 4.3 for a glimpse at the merger dynamics of some of the listed models).

However, the manner in which the average electron fraction depends on the initial configuration appears to be less trivial. The top panels in figure 4.5 compare the Y_e distribution of the ejected material for merger simulations employing different NS masses, with the DD2 (top-left) and SFHo (top-right) EoS. For the SFHo cases, we can observe a small shift in the distribution towards higher Y_e for the more massive NSs. This behaviour can be explained by the higher temperatures reached during the merger, due to the increased violence of the collision by a stronger gravitational pull and a similar NS compactness. Higher temperatures translate into increased neutrino luminosities (see middle panels in figure 4.6) and because neutrons are much more abundant than protons ($Y_e \ll 0.5$), $\bar{\nu}_e$ emission pushes the ejecta Y_e to higher values (equation 1.4). Nevertheless, the same trend cannot be appreciated for the models with the DD2 EoS, where all three distributions seem undistinguishable. A more carefull and direction-dependent analysis and a more detailed exploration of the parameter space would be necessary to understand the origin of these differences, as well as the exact impact of neutrino re-absorption.

The bottom panel of figure 4.5 shows a clear dependency of the ejecta Y_e on the EoS, which is also evident in table 4.2. The same argument we used to explain the differences between the two symmetric mergers with different masses and the SFHo Eos, applies in this case as well. Softer EoS produce more compact stars, which can inspiral to closer orbits, thus reaching higher velocities and colliding more violently. More $\bar{\nu}_e$ are produced due to the higher temperatures and abundance of neutrons, thus increasing the Y_e of the NS matter. Figure E.2 in the appendix E, shows the mass-radius relations of the employed EoS, helping interpret the differences in the ejecta masses and Y_e distributions.

In table 4.3 we list the neutrino luminosities and mean energies, measured at 5 ms post-merger, from the models described in table 4.2. The neutrino mean energies of all species, calculated with the two approaches described in equations (2.52) and (2.56), are almost independent of the merger initial configuration. Heavy lepton neutrinos are the most energetic of all three species, followed by $\bar{\nu}_e$ and ν_e. Because the neutrino luminosities depend strongly on the matter temperature, systems with more compact and massive NSs will produce a higher flux of neutrinos of all species. Given the high neutron richness of NS matter, $\bar{\nu}_e$ emission dominates over the other individual ν_i species[7]. Figure 4.6 shows the time evolution of the luminosities of all three neutrino species for all the models presented in table 4.2. At 5 ms, when we extracted the data presented in tables 4.2 and 4.3, the ν_e luminosity is still increasing, while $\bar{\nu}_e$ and ν_x luminosities remain approximately constant.

In some of the models, especially in those employing the SFHo EoS, a bright $\bar{\nu}_e$ (and to a lesser extent ν_e) flash appears shortly after merger. It is not clear if this effect has any physical meaning or is a numerical artifact caused by leakage schemes, as it is also present in the simulations performed by Palenzuela et al. (2015) and Sekiguchi et al. (2015), which used the same EoS, but a "conventional" leakage

[7]The luminosity of all ν_x species together, still dominates the $\bar{\nu}_e$ ones in all cases.

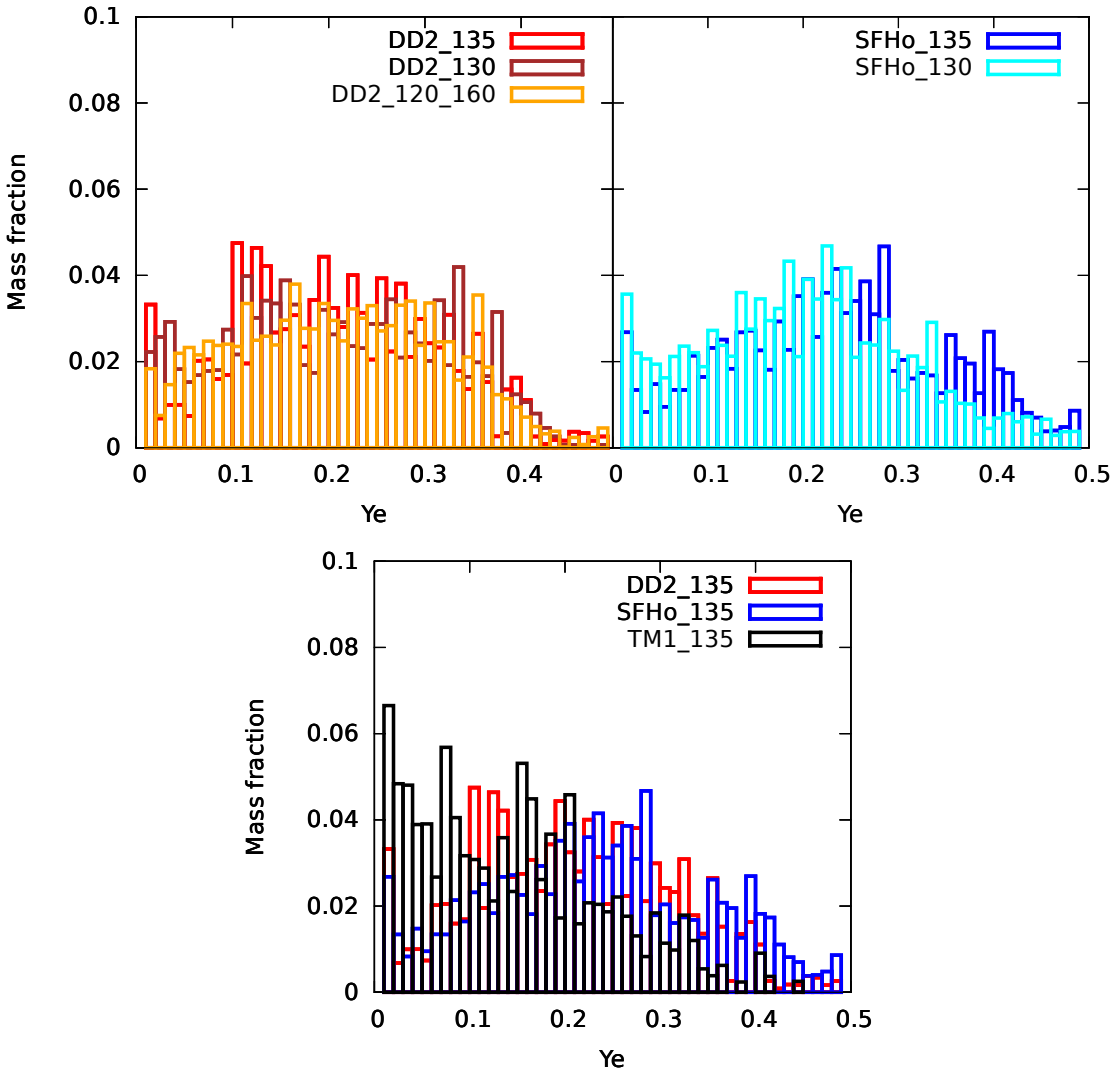

Figure 4.5.: Histograms showing the electron fraction (vs. mass fraction) of the material ejected in the NS merger models introduced in table 4.2. The top-left panel shows the results of the simulations which employ the DD2 EoS with different initial NS masses: $1.35 - 1.35\ M_{\odot}$, $1.30 - 1.30\ M_{\odot}$ and $1.20 - 1.60\ M_{\odot}$. The top-right panel displays also the models with different initial NS masses, $1.35 - 1.35\ M_{\odot}$ and $1.30 - 1.30\ M_{\odot}$, but for the simulations employing the SFHo EoS. The bottom panel displays the results of the symmetric NS merger models with masses $1.35\ M_{\odot}$ employing three different EoS: DD2, SFHo and TM1.

scheme and a leakage-M1 hybrid, respectively. In contrast, the results reported by Foucart et al. (2016) employing both, a leakage and a grey M1 scheme do not show this feature.

Table 4.3.: Luminosities and mean energies (calculated as equations (2.52) and (2.56)) of all three neutrino species obtained from the NS merger models listed in table 4.2. All quantities are taken as seen by an observer at infinity, extracted at 5 ms post-merger. Heavy lepton neutrino luminosities are displayed for each ν_x species.

Merger Model	L_{ν_e} (10^{52}erg/s)	$L_{\bar{\nu}_e}$ (10^{52}erg/s)	L_{ν_x} (10^{52}erg/s)	$\langle\epsilon^{\text{leak}}_{\nu_e}\rangle$ (MeV)	$\langle\epsilon^{\text{tot}}_{\nu_e}\rangle$ (MeV)	$\langle\epsilon^{\text{leak}}_{\bar{\nu}_e}\rangle$ (MeV)	$\langle\epsilon^{\text{tot}}_{\bar{\nu}_e}\rangle$ (MeV)	$\langle\epsilon^{\text{leak}}_{\nu_x}\rangle$ (MeV)
DD2_135	3.3	5.1	1.9	9.0	15.3	11.5	18.6	24.7
DD2_130	2.8	4.3	1.6	9.4	15.2	11.8	18.5	25.0
DD2_120_160	4.6	7.4	3.3	9.0	14.7	11.4	17.9	25.2
SFHo_135	4.0	6.1	3.0	9.5	15.4	11.1	18.5	24.6
SFHo_130	3.3	4.9	2.4	9.1	15.1	10.7	18.3	24.6
TM1_135	2.0	3.5	1.1	8.6	13.7	11.3	17.6	24.5

4.2.3. Comparison of the results obtained by ILEAS with those given in the literature

As mentioned in section 4.2.2, the initial conditions (NS masses and EoS) of the presented NS-NS merger models were chosen to match the ones employed by other NS-NS merger simulations discussed in the literature in which the effects of neutrinos were also included. In this section we contrast the original results reported by three different numerical approaches, Sekiguchi et al. (2015, 2016) (referred as *Kyoto code* hereafter), Foucart et al. (2016) (referred as *SpEC*) and Palenzuela et al. (2015) (referred as *US code*), with the ones obtained by our ILEAS+SPH-CFC code for the same NS binary setups.

We must caution the reader that important differences can arise in some neutrino-related quantities due to the different treatment of the hydrodynamic evolution of the systems. Although general agreement is observed amongst the different approaches, neutrino interactions depend on multiple powers of the temperature (see appendix B), and hence small differences in the profiles can be severely amplified. In particular, while our merger code relies on a SPH discretization of the hydrodynamic equations with a CFC approximation for the description of GR (see section 2.1), the Kyoto code, SpEC and the US code rely on grid-based hydro-solvers with different formulations of GR (see Sekiguchi et al. 2012, Duez et al. 2008 and Neilsen et al. 2014, respectively). Therefore, only qualitative agreement between the different numerical approaches can be expected.

Neutrino physics are treated differently in the thee numerical approaches as well. On the one hand, the Kyoto code employs a relativistic leakage scheme (Sekiguchi, 2010; Sekiguchi et al., 2012) to estimate the neutrino losses and provide the production source terms for the M1 moment equations (Shibata et al., 2011), which are then used to evolve a free-streaming component of the neutrinos. This approach accounts for neutrino re-absorption besides leakage losses (Kyutoku et al., 2018). Finally, neutrinos are assumed to be trapped and in equilibrium within the fluid in optically thick conditions, defined by a β-equilibrium limiter (Sekiguchi, 2010; Sekiguchi et al., 2012) (see also section 1.2). On the other hand, both SpEC (Deaton et al., 2013; Foucart et al., 2014) and the US code (Neilsen et al., 2014) model the neutrino interactions by means of a "conventional" lakage scheme (Rosswog and Liebendörfer, 2003; O'Connor and Ott, 2010). In Foucart et al. (2015) they also employed an energy-averaged M1 scheme for one of their models and compared the results with the ones obtained by SpEC. Unfortunately, we cannot currently reproduce the initial NS-NS binary configuration of such a model because we do not have the necessary EoS implemented. However, we can use the information provided for a qualitative assessment of ILEAS' results, especially in comparison with "conventional" lakage schemes.

In table 4.4 we list the initial configuration of the relevant models described in the abovementioned papers, as well as the reported ejecta properties (analogous to table 4.2). For a comfortable comparison, we also include the results of the simulations performed in this work, with the ejecta properties measured at the same times post-

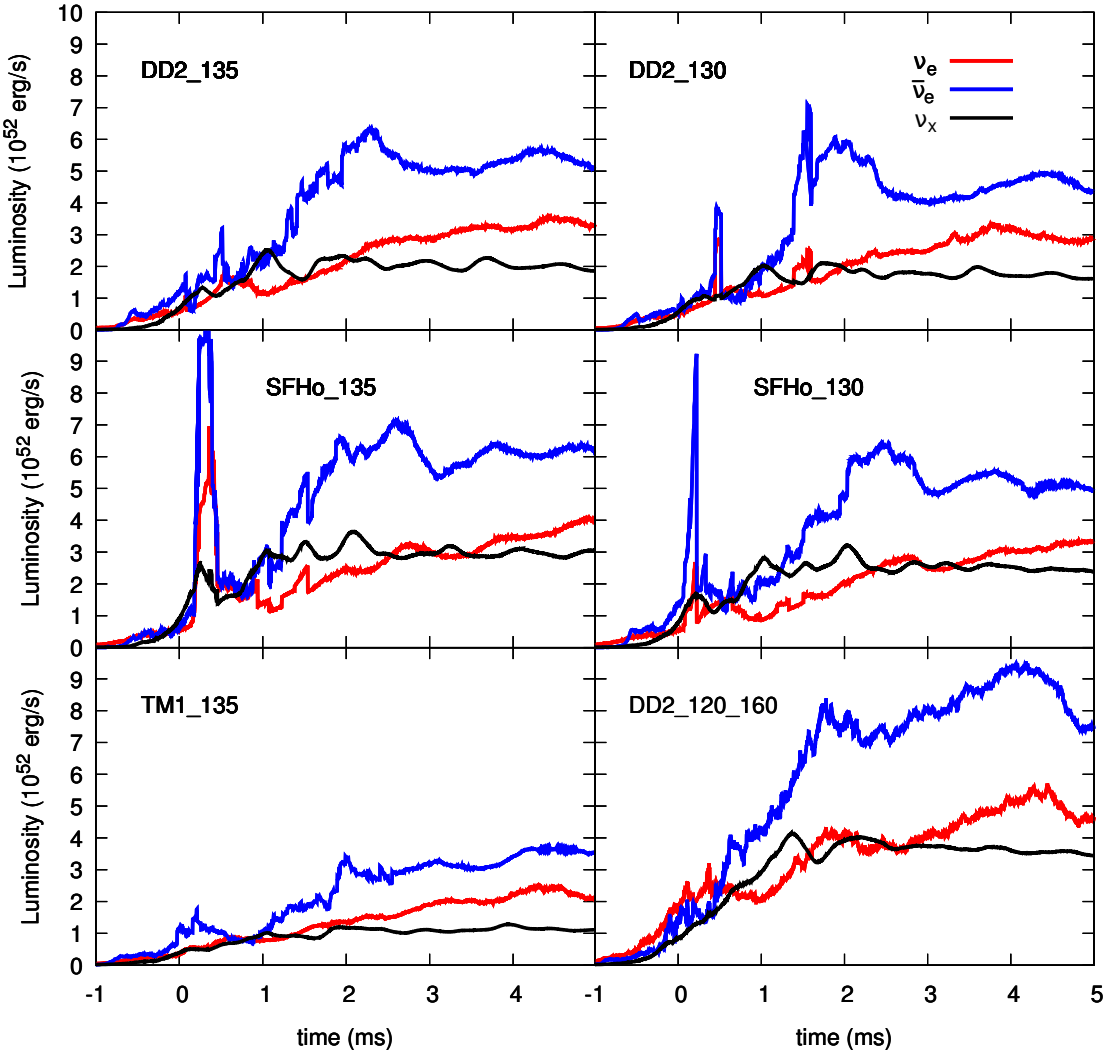

Figure 4.6.: Time evolution of the ν_e, $\bar{\nu}_e$ and ν_x (each) luminosities obtained from the NS merger models listed in tables 4.2 and 4.3, as seen by an observer at infinity.

merger as the literature models. Overall, we find qualitatively good agreement in the ejecta masses and to some extent quantitatively (~ 30 per cent) for most of the models. Some exceptions are the SFHo simulation from the Kyoto group, which exhibits an unusually large amount of ejecta, even for a soft EoS, and the SpEC model also employing SFHo, which displays a ridiculosly small amount of ejecta mass, exactly the opposite as one would expect for such compact NSs. Nevertheless, it must be noted that in Foucart et al. (2016) the autors describe their ejecta masses as "unreliable", as simulations with different resolutions yield different amounts of unbound material, about an order of magnitude appart. In general, grid-based codes rely on a low density environment (athmosphere or floor value) in which the object of the simulation evolves. This residual density interacts with the outflows, causing possible artificial behaviour of the ejecta. For this same reason, the US group reports the ejecta properties only at 3 ms post-merger, in order to minimize the athmospheric pollution of later, slower outflows (Palenzuela et al., 2015).

As we already pointed out in section 1, there is no consensus on the $\langle Y_e \rangle$ of ejected material obtained by different groups and different neutrino schemes. The models from the Kyoto group show (for two out of three cases) higher average Y_e than our presented simulations and a clear dependence of $\langle Y_e \rangle$ on the EoS, specially for the SFHo case, which has has a $\langle Y_e \rangle = 0.31$. This extra high $\langle Y_e \rangle$ together with the extra high ejecta mass they report are probably related to extreme temperatures reached during the collision. In Sekiguchi et al. (2015), the authors plot the Y_e distribution of the ejecta for the three discussed models (TM1_135(K), DD2_135(K), SFHo_135(K)), in which most of the material clusters around the average value of the electron fraction[8]. This behaviour is a bit different to what we observe in our simulations, where the ejecta is distributed more homogeneously between $Y_e = 0.001$ and $Y_e = 0.4$ (see figure 4.4). In spite of all these small differences, we find a good qualitative agreement between ILEAS' results and those obtained by the Kyoto group, particularly in the dependency of the ejecta masses and electron fractions on the EoS.

On the contrary, the results from SpEC show a lower average Y_e, insensitive to the EoS of NS matter ($\langle Y_e \rangle = 0.11$). This lower Y_e is probably associated with the lack of neutrino re-absorption, as suggested in Foucart et al. (2016), when comparing it to the higher electron fraction, $\langle Y_e \rangle = 0.2$, obtained by their model employing M1 (which implicitly includes neutrino re-absorption). This M1 $\langle Y_e \rangle$ is perfectly compatible with the one we observe in the ILEAS model using the DD2 EoS, which has a *similar* mass-radius relation as the one employed in Foucart et al. (2016).

In contrast, the US models show a disconcertingly high $\langle Y_e \rangle$ for a leakage scheme, but as the SpEC results, no dependence on the EoS is observed. Interestingly, this leakage scheme is virtually the same as the one employed in SpEC (with some small modifications), so more similar results between the two groups would have been expected. The differences in the NS masses used for the initial binary setups simulated by both groups are not prominent enough to justify the disagreement, as

[8]Beware the logatihmic axis in the plot.

demonstrated by the small differences we observe in the results presented in this work between merger models with different NS masses (see table 4.3).

In spite of the huge discrepancies between the ejecta average Y_e obtained by the Kyoto code and SpEC, there is a strikingly good agreement in their ν_e and $\bar{\nu}_e$ luminosities. This is even more surprising, if one has in mind that the Kyoto models do include neutrino re-absorption, while SpEC does not. In fact, in Foucart et al. (2016) the authors show how in the results obtained with their M1 scheme, the ν_e luminosities are reduced by a factor two with respect to the leakage case due to re-absorption of neutrinos in the torus surrounding the HMNS (with no obvious changes in $\bar{\nu}_e$). Therefore, one would expect a similar reduction of the luminosities in other neutrino schemes with absorption. In contrast, the results obtained by the US code show discrepancies with the Kyoto and SpEC simulations ranging from ten per cent to a factor two.

Regardless of the quantitative differences, in all numerical approaches higher luminosities of all neutrino flavours are reported for more compact EoS, and in general following the hierarchy $L_{\bar{\nu}_e} > L_{\nu_e} > L_{\nu_x}$. In most models we observe a prevailing $\bar{\nu}_e/\nu_e$ luminosity ratio of ~ 1.5, as reported by Foucart et al. (2016), except for one of the SFHo simulations. Finally, the mean energies reported by SpEC are in good agreement with the ones obtained by ILEAS (equation 2.56), although the ones reported by the other groups are a few MeV lower.

To summarize, we find overall good qualitative agreement between our results and those reported in the literature which employ more sophisticated neutrino treatments, such as Sekiguchi et al. (2015). The presented results help thus validate the trends in the ejecta composition previously published by some other groups, with respect to its dependence on the NS masses and the EoS. The systematically higher $\langle Y_e \rangle$ we observe in comparison with numerical approaches relying on "conventional" leakage schemes (Palenzuela et al., 2015; Foucart et al., 2016) highlights the need to include transport effects, such as β-equilibration and neutrino re-absorption, in order to describe the evolution of the ejecta composition to sufficient accuracy.

Table 4.4.: List of NS merger models used for the comparisons in section 4.2.3, including the literature source from where the data is extracted, the initial setup (NS masses and EoS), the properties of the ejected material (mass and $\langle Y_e \rangle$) and the time post-merger at which they are extracted. Additionally, we include the models simulated in this work, with the ejecta quantities measured at the same time post-merger as the literature models.

Merger Model	Source	EoS	NS masses ($M_\odot$)	Ejecta mass ($10^3\ M_\odot$)	Ejecta $\langle Y_e \rangle$	Measurement time (ms)
DD2_135(K)	Sekiguchi et al. (2015)	DD2	1.35-1.35	2.0†	0.23†	10
DD2_135	This work	DD2	1.35-1.35	2.2	0.23	10
DD2_135(US)	Palenzuela et al. (2015)	DD2	1.35-1.35	0.43	$\sim 0.18^\downarrow$	3
DD2_135	This work	DD2	1.35-1.35	1.8	0.20	3
DD2_130(SpEC)	Foucart et al. (2016)	DD2	1.30-1.30	1.3	0.11	10
DD2_130	This work	DD2	1.30-1.30	1.9	0.22	10
SFHo_135(K)	Sekiguchi et al. (2015)	SFHo	1.35-1.35	10.0†	0.31†	10
SFHo_135	This work	SFHo	1.35-1.35	3.2	0.25	10
SFHo_135(US)	Palenzuela et al. (2015)	SFHo	1.35-1.35	3.2	$\sim 0.18^\downarrow$	3
SFHo_135	This work	SFHo	1.35-1.35	2.4	0.22	3
SFHo_130(SpEC)	Foucart et al. (2016)	SFHo	1.30-1.30	0.5	0.11	10
SFHo_130	This work	SFHo	1.30-1.30	2.2	0.21	10
TM1_135(K)	Sekiguchi et al. (2015)	TM1	1.35-1.35	1.0†	0.22†	10
TM1_135	This work	TM1	1.35-1.35	1.2	0.16	10

† Data extracted from the corresponding plots at the chosen time.

$^\downarrow$ Data extracted from a histogram.

5. Summary and conclusions

In this thesis, we have introduced ILEAS (Improved Leakage-Equilibration-Absorption Scheme), an improved leakage method which accounts for the basic physical effects of neutrino transport at moderate computational costs. ILEAS is ideal for exploring wide parameter spaces in three dimensions, where ~ 10 per cent of accuracy is enough to capture the essential impact of neutrino physics.

Original leakage models (Ruffert et al., 1996; Rosswog and Liebendörfer, 2003) describe the local neutrino losses (but not transport) by means of an interpolation between the diffusion and free-streaming limits. However, not only do they omit important aspects of neutrino transport, such as neutrino-matter β-equilibrium in optically thick conditions or neutrino re-absorption in the optically thin regime, but also generally misrepresent the neutrino losses by diffusion due to their simplistic ansatz based on a dimensional analysis for the diffusion timescale. Truncated moment schemes provide a more sophisticated alternative to leakage schemes for the modelling of neutrino transport. Nevertheless, they require substantially larger computational resources and face serious difficulties when modelling crossing beams of neutrino radiation, casting doubt on their reliability in determining the correct composition of polar outflows in NS-NS mergers. Additionally, another potential problem of such schemes may be the lack of accuracy in following neutrinos in fast (~ 0.3 times the speed of light) moving material due to limitations in numerical resolution. Unfortunately, such tests are not available in the literature.

With this in mind, ILEAS builds upon the leakage ansatz, greatly improving its description of neutrino transport effects while retaining computational efficiency and simplicity. In the first place, the crude description of diffusion typical of "conventional" leakage schemes is replaced by a more accurate formulation of the escape time-scale based on the flux-limited diffusion equation, which provides a much better estimate of the neutrino losses in optically thick regions. Furthermore, neutrinos trapped and in β-equilibrium with the moving fluid contribute to the matter pressure and energy density, and the recovery of the correct electron and neutrino fractions in the β-equilibrium regime is ensured by our equilibration step. Finally, we employ a three-dimensional ray-tracing algorithm to account for the re-absorption in optically thin conditions of the neutrinos that are radiated away from the system. We resorted to a grey approximation for ILEAS in order to keep the ray-tracing for the absorption module at a reasonable computational cost. Nevertheless, we account for the detailed dependence on the neutrino spectra both in the calculation of the diffusion time-scales, approximately capturing the energy dependent decoupling of neutrinos from matter, and along the rays in the absorption module.

Comparisons between different neutrino treatments in the literature are scarce

(Foucart et al., 2016; Perego et al., 2016), and tests demonstrating the accuracy of many widely employed schemes are not available. In contrast, we provided detailed comparisons of the performance of ILEAS with more sophisticated neutrino transport schemes in relevant astrophysical scenarios. Because our final goal is the application of ILEAS in the context of NS mergers, we selected simulations which reproduce the typical conditions achieved during such events. Therefore, we chose the dense, hot environment of PNSs as reasonably similar to that of a HMNS remnant, allowing us to test the new description of the diffusion time-scale, the equilibration treatment, the decoupling of neutrinos from matter in the semitransparent regime and their subsequent partial re-absorption by the optically thin material surrounding the PNS. We presented the results obtained by ILEAS applied on 3D mappings of several PNS cooling snapshots from the 1D simulation (Sr) performed by Hüdepohl et al. (2010), where the authors employed the neutrino transport code VERTEX. After a short relaxation of the initial conditions, ILEAS was able to reproduce the VERTEX results in all tested cases, ranging from 0.2 s until 1.5 s post-bounce, with ~ 10 per cent of accuracy. Not only did ILEAS show such good agreement in the total neutrino luminosities, but also in the complete radial luminosity profiles. For a time-dependent comparison, we evolved the medium temperature and Y_e of one of the snapshots (keeping the density fixed) for 50 ms using both an M1 neutrino transport code, ALCAR (Just et al., 2015b), and ILEAS. We found that the good agreement (~ 10 per cent) was maintained throughout the simulation.

One of the most innovative upgrades of ILEAS is its treatment of neutrino reabsorption. In order to verify the performance of this treatment, we tested ILEAS in the context of BH-torus systems, natural representations of highly asymmetric mass distributions with a nearly transparent conditions to neutrinos. Snapshot calculations of thick ($0.3\ M_\odot$) and thin ($0.1\ M_\odot$) tori around BHs demonstrated a good qualitative and quantitative agreement between ALCAR and ILEAS in the characterization of neutrino re-absorption, also of its geometry. As with the PNS case, we evolved the temperature and Y_e of both BH-torus models for 50 ms using ALCAR and ILEAS, and reported also an agreement of ~ 10 per cent preserved during the whole simulation.

We concluded that, despite the approximative nature of the treatment, ILEAS is sufficiently good to reproduce the results of more sophisticated transport schemes on the level of ~ 10 per cent, locally and globally and i their time dependence.

The next logical step after assessing the capability of ILEAS to reproduce transport results, was its application on NS-NS merger calculations. We coupled ILEAS to our relativistic smoothed particle hydrodynamics (SPH) NS-NS merger code and performed a variety of numerical simulations. In the first place, choosing a "standard" initial configuration (a symmetric $1.35\ M_\odot$ binary NS and a moderately stiff EoS, DD2), we tested the impact of the individual modules which compose our ILEAS scheme on the properties of material ejected during the merger. We described how the neutrino losses caused by the leakage module and the energy loss of SPH particles leaving the β-equilibrium region consistently reduce the amount of ejected mass by up to $\sim 25-40$ per cent compared to the case without neutrino in-

teractions, from $M_{\rm ej} = 2.6{\cdot}10^{-3}\ M_{\odot}$ to $M_{\rm ej} = 1.5{\cdot}10^{-3} - 1.9{\cdot}10^{-3}\ M_{\odot}$. In contrast, energy deposition by neutrino re-absorption on loosely bound SPH particles pushes this reduction to < 25 per cent ($M_{\rm ej} = 1.9{\cdot}10^{-3} - 2.0{\cdot}10^{-3}\ M_{\odot}$). As expected, the impact of the different aspects of neutrino transport on the ejecta composition is non-trivial (figure 4.4). While the neutrino leakage and re-absorption modules seem to spread the ejecta Y_e between 0.02 to 0.5, the equilibration treatment concentrates more material around the intermediate values ($Y_e \approx 0.2$). Neutrino re-absorption does not seem to change noticeably the average ejecta Y_e, but pushes more ejecta mass both to lower ($Y_e \approx 0.05$) and to higher ($Y_e \approx 0.35$) electron fractions.

In order to assess the impact of the initial binary configuration on the ejecta properties and neutrino-related quantities, we performed a set of NS-NS merger simulations with different NS masses, mass asymmetries and EoSs. Unfortunately, a detailed comparison with other models reported in the literature is not possible due to underlying differences between the numerical approaches which are not directly related to the treatment of neutrinos. In fact, substantial discrepancies already exist amongst the various results published by different groups. These differences are possibly linked to the diverse treatments of hydrodynamics, the formulations of GR or resolution issues, besides the differences in the neutrino treatment, all of which can severely influence the impact of neutrino effects (Sekiguchi et al., 2015; Palenzuela et al., 2015; Foucart et al., 2016).

Therefore, the simulations reported in this work add to a small pool of computational models available in the literature, serving as a cross check of the qualitative results reported by other groups. Qualitatively, ILEAS reproduces the trends already observed by Sekiguchi et al. (2015) in the ejecta masses and composition and in the neutrino luminosities. Nevertheless, other groups do not find the same patterns (Palenzuela et al., 2015; Foucart et al., 2016). Further progress can only be achieved by direct comparison of neutrino schemes employing the same exact code for the hydrodynamical evolution of the NS-NS/BH merger. For this reason we are considering the option of opening ILEAS to public domain, or at least to make it available for other groups in a collaboration to improve our understanding of neutrino effects in NS-NS/BH merger simulations.

In conclusion, in this thesis we introduced a new improved neutrino leakage scheme, ILEAS, and demonstrated its outstanding performance, by reproducing neutrino transport results within ~ 10 per cent accuracy in several multi-dimensional astrophysical scenarios. ILEAS includes the fundamental physical effects of neutrino transport that play a role on evolution time-scales shorter than the diffusion time-scale. It surpasses the performance of "conventional" leakage schemes while retaining most of their efficiency and simplicity, providing a more complete picture of the variations of the matter composition in NS-NS mergers. The accuracy and computational efficiency of our scheme render it ideal for the exploration of the vast parameter space of possible binary configurations in NS-NS/BH merger simulations.

With the first direct detection of a GW signal from a NS-NS merger event (GW170817), followed by the observation of its associated EM counterparts (Abbott et al., 2017a,f), the era of multi-messenger astronomy has begun, and with it, the

demand for accurate predictions of future observables is more important than ever. At the time of the writing of this thesis, the three GW detectors are being upgraded for the next observing run (O3), which is due to start next autumn and last a whole year. With the new upgrade, the GW detectors will increase their detection distance by a factor ~ 2 (detection volume by a factor ~ 8) (Abbott et al., 2016a), and predictions suggest a NS-NS merger detection rate of $3 - 18$ events per year (Kim et al., 2015; Dominik et al., 2015). Many of these potential detections will likely be followed by an observable kilonova, which will provide invaluable information about the merger events and the ejected material.

The identification of a kilonova signal associated with the GW170817 event and the subsequent debate about its exact nature (e.g. Cowperthwaite et al. 2017; Nicholl et al. 2017; Chornock et al. 2017; Kasen et al. 2017; Smartt et al. 2017; Pian et al. 2017; Perego et al. 2017), have brought to light the need of a reliable understanding of the composition and spatial distribution of the merger ejecta. This knowledge can only be achieved by means of numerical simulations of NS-NS/BH mergers which include all the relevant physics to sufficient accuracy, especially neutrinos. Therefore, the tool presented in this work will serve the need of probing the parameter space of initial conditions that describe NS-NS/BH binaries (system masses and mass ratios, spins, orbital parameters, EoS), and will help to improve our understanding of the composition and distribution of the ejected material. This information will be used to predict the elemental abundances in the merger ejecta, as well as the characteristics of the associated kilonovae, to be contrasted with the future observations.

For an even more accurate description of the neutrino microphysics and their impact on the matter composition, upgrades of the neutrino interactions included in ILEAS should be considered in the future. Mean-field effects (Roberts, 2012; Roberts et al., 2012; Martínez-Pinedo et al., 2012), nucleon recoil and weak magnetism corrections (Horowitz, 2002) are significant improvements to the neutrino-nucleon interaction cross sections, relevant at the matter densities typical of NSs. All these effects alter the spectra and luminosities of each neutrino species in a different measure, thus potentially influencing the composition of matter outflows in NS mergers. Furthermore, neutrino oscillations have been shown to also have a relevant impact on the radiated luminosities in different neutrino species (Wu and Tamborra, 2017; Wu et al., 2017). The composition of the ejected material can be influenced by the exposition of the outflow to modified neutrino luminosities caused by fast flavour conversions of $\nu_e\bar{\nu}_e$ pairs to $\nu_\mu\bar{\nu}_\mu$ or $\nu_\tau\bar{\nu}_\tau$. For this reason also oscillation physics should be included in ILEAS and merger simulations in future modelling efforts.

Appendices

A. Comparative analysis of diffusion time-scale prescriptions used in the literature

Although leakage schemes have been around for more than two decades, not many comparisons between the different realizations can be found in the literature. Here we want to briefly compare the most common leakage implementations used in the context of neutrino physics in NS mergers, in particular, the schemes from Ruffert et al. (1996) (RJS) and Rosswog and Liebendörfer (2003) (RL).

There are three main differences between both schemes: the definition of the diffusion time-scale, the energy averaging and the prescription of the neutrino chemical potential to describe the neutrino spectra.

As we discussed in section 2.3.1, in a first approximation the diffusion time-scale can be obtained from a dimensional analysis of the diffusion equation as,

$$t_{\nu_i}^{\rm diff} = \frac{3d^2}{c\lambda_{\nu_i}}, \tag{A.1}$$

where d is simply a characteristic length-scale of the system. RJS took the approximation of a homogeneous sphere to define

$$\lambda_{\nu_i} = \frac{d}{\tau_{\nu_i}}. \tag{A.2}$$

By plugging equation (A.2) into (A.1) we are left with one factor of the length-scale, which is chosen as the integration path for the optical depth, taken as the minimum distance to the neutrinosphere ($r(\tau_{\nu_i} = 2/3)$):

$$t_{\nu_i}^{\rm diff,RJS} = \frac{3d}{c}\tau_{\nu_i}. \tag{A.3}$$

Similarly, RL proceeded to further approximate the remaining length-scale as $d \sim \tau_{\nu_i}\lambda_{\nu_i}$ (with $\lambda_{\nu_i} = 1/\kappa_{\nu_i}$) to obtain:

$$t_{\nu_i}^{\rm diff,RL} = \frac{3\lambda_{\nu_i}}{c}\tau_{\nu_i}^2. \tag{A.4}$$

It is worth noting that other groups have suggested alternative prescriptions for the definition of d, such as using the pressure scale-hight $d \simeq P/\boldsymbol{\nabla} P$ (Metzger and

Fernández, 2014). This approach could be generalized to using the scale-height of any convenient scalar quantity that defines the medium in which neutrinos diffuse.

One of the caveats of grey schemes is the unambiguity associated with the energy averaging of the neutrino quantities. In RJS, the diffusion time-scales are computed from spectrally averaged opacities (and optical depths),

$$\bar{\kappa}_{\nu_i} = \frac{\int_0^\infty \kappa_{\nu_i}(\epsilon)\epsilon^2 f(\epsilon;\eta_{\nu_i})\mathrm{d}\epsilon}{\int_0^\infty \epsilon^2 f(\epsilon;\eta_{\nu_i})\mathrm{d}\epsilon}. \tag{A.5}$$

In RL, on the contrary, the (roughly) ϵ^2 dependence of the opacities is factored out and carried on to the calculation of the integrated diffusion rates,

$$R^j_{\nu_i,\mathrm{diff}} = \int_0^\infty \frac{E^{j=0}_{\nu_i}(\epsilon)}{t^{\mathrm{diff}}_{\nu_i}(\epsilon)}\mathrm{d}\epsilon = \int_0^\infty \frac{E^{j=0}_{\nu_i}(\epsilon)}{t^{\mathrm{diff,RL}}_{\nu_i}\epsilon^2}\mathrm{d}\epsilon, \tag{A.6}$$

for lepton number diffusion and equivalently for the energy diffusion rate,

$$Q^j_{\nu_i,\mathrm{diff}} = \int_0^\infty \frac{E^{j=1}_{\nu_i}(\epsilon)}{t^{\mathrm{diff}}_{\nu_i}(\epsilon)}\mathrm{d}\epsilon = \int_0^\infty \frac{E^{j=1}_{\nu_i}(\epsilon)}{t^{\mathrm{diff,RL}}_{\nu_i}\epsilon^2}\mathrm{d}\epsilon. \tag{A.7}$$

In both schemes, the effective loss term is then calculated as an interpolation between diffusive and production rates:

$$R^-_{\nu_i} \equiv R_{\nu_i}\left(1+\frac{R_{\nu_i}}{R^j_{\nu_i,\mathrm{diff}}}\right)^{-1}, \tag{A.8}$$

and

$$Q^-_{\nu_i} \equiv Q_{\nu_i}\left(1+\frac{Q_{\nu_i}}{Q^j_{\nu_i,\mathrm{diff}}}\right)^{-1}, \tag{A.9}$$

for number and energy, respectively, which are equivalent to equations (2.21) and (2.22) in the case of the RJS averaging.

Moreover, without an actual energy-dependent transport scheme, it is impossible to determine the correct neutrino phase-space distribution. In the optically thick regime, neutrinos remain in β-equilibrium with the medium, thus their spectrum is a Fermi distribution with the chemical potential being easily obtained from the EoS. RL assume that this behaviour will remain a good approximation even in the optically thin regime, where neutrinos decouple from matter. RJS on the other hand also use a Fermi distribution throughout, but interpolate between the equilibrium chemical potential and an expected value at free streaming conditions of $\mu_\nu = 0$ (see equation 2.25).

We apply both schemes to one of our PNS cooling snapshots and compare the results to the ILEAS model presented in this work. To further disentangle the contribution of each approximation, we also test different permutations, combining the prescriptions for the diffusion time-scale, the spectral averaging and the neutrino

chemical potential out of equilibrium. A list of the models and the prescriptions employed are provided in table A.1. In order to focus on the impact of the leakage module alone, we let the system relax *without* including equilibration or neutrino absorption in any of the calculations. Relativistic corrections in the diffusion time-scale are omitted as well. Figure A.1 shows the radial profiles of the electron fraction and luminosity profiles for all the relaxed models (after 5 ms) together with the ones obtained by ALCAR and ILEAS (including all modules).

The first aspect that catches the eye is the substantial improvement of our prescription (model 7) with respect to all previous models. For the luminosities this is particularly true in the high-optical-depth regime, where the diffusion time-scale dominates. This is no surprise, as we define $t^{\text{diff}}_{\nu_i}$ directly from the diffusion equation, which encodes much more information about the way neutrinos are transported than the simple ansatz of equation (A.1). Due to the slightly slower increase of RL's $t^{\text{diff}}_{\nu_i}$ with growing optical depth (models 2,3,6) in comparison to RJS's $t^{\text{diff}}_{\nu_i}$ (models 1,4,5), neutrinos escape from further inside the star in the former models. As a consequence, they resemble a bit closer the transport profile, but overproduce neutrinos of all species at lower optical depths. On the other hand, the consequences of the energy averaging are much less straightforward. Differences between a few percent up to a factor 3 can be seen for the different species.

The choice of neutrino chemical potential does not significantly affect the results of the leakage scheme in the chosen snapshot. The differences could become more significant in a scenario where most neutrino luminosities are produced in the semitransparent region. Based on the current results, however, the interpolated μ_ν (equation 2.25) should be preferred, because it fulfils the correct limit at high optical depth and a well controlled behaviour at low optical depths, thus avoiding an undesirable behaviour of the analytical solutions of the Fermi integrals and their ratios at low optical depth.

It is impossible to draw a definitive conclusion from the presented data, but for the studied case, the standard formalism from RJS seems, overall, to be in somewhat better agreement with the transport results.

It is worth noticing that, as can be seen in the first panel of figure A.1, all leakage versions produce a similar effect on the electron fraction after relaxation. Namely, the low Y_e region near the NS surface expands outwards and the matter becomes more neutron rich. The cause for this effect is simply the inability of any leakage scheme to accurately describe the semitransparent region, which comes as no surprise being a model constructed as an interpolation between pure diffusion and pure free streaming. A similar effect, albeit to a much smaller extent due to the more accurate diffusion time-scale, can be observed when applying ILEAS. This comparison further highlights the advantages of the scheme presented in this work with respect to some of the leakage versions widely used in the literature.

Table A.1.: Summary of the prescriptions for the neutrino diffusion time-scale, $t^{\mathrm{diff}}_{\nu_i}$, energy averaging and neutrino chemical potential, μ_ν, employed for all models shown in figure A.1. Additionally, we present the neutrino luminosities of the three neutrino species obtained by applying them to a PNS snapshot at 0.5 s post-bounce. Models 1-7 do not include the effects of neutrino re-absorption or equilibration, whereas the results obtained by ILEAS and ALCAR do.

Model	$t^{\mathrm{diff}}_{\nu_i}$	Energy Avg.	μ_ν	L_{ν_e} (10^{51} erg$\cdot$s^{-1})	$L_{\bar{\nu}_e}$ (10^{51} erg$\cdot$s^{-1})	L_{ν_x} (10^{51} erg$\cdot$s^{-1})
Model 1	RJS[1]	RJS	RJS	7.0	7.8	4.2
Model 2	RL[2]	RL	RL	17.9	19.3	4.8
Model 3	RL	RJS	RJS	18.5	16.5	15.4
Model 4	RJS	RL	RJS	10.1	11.9	3.0
Model 5	RJS	RJS	RL	7.0	7.6	4.2
Model 6	RL	RL	RJS	18.6	19.3	4.8
Model 7	AJJB[3]	AJJB	AJJB	9.1	12.5	10.4
ILEAS	AJJB[3]	AJJB	AJJB	6.7	8.1	10.4
ALCAR	-	-	-	7.0	7.6	9.0

[1] Ruffert, Janka & Schäfer (Ruffert et al., 1996)
[2] Rosswog & Liebendörfer (Rosswog and Liebendörfer, 2003)
[3] Ardevol, Janka, Just & Bauswein (this work)

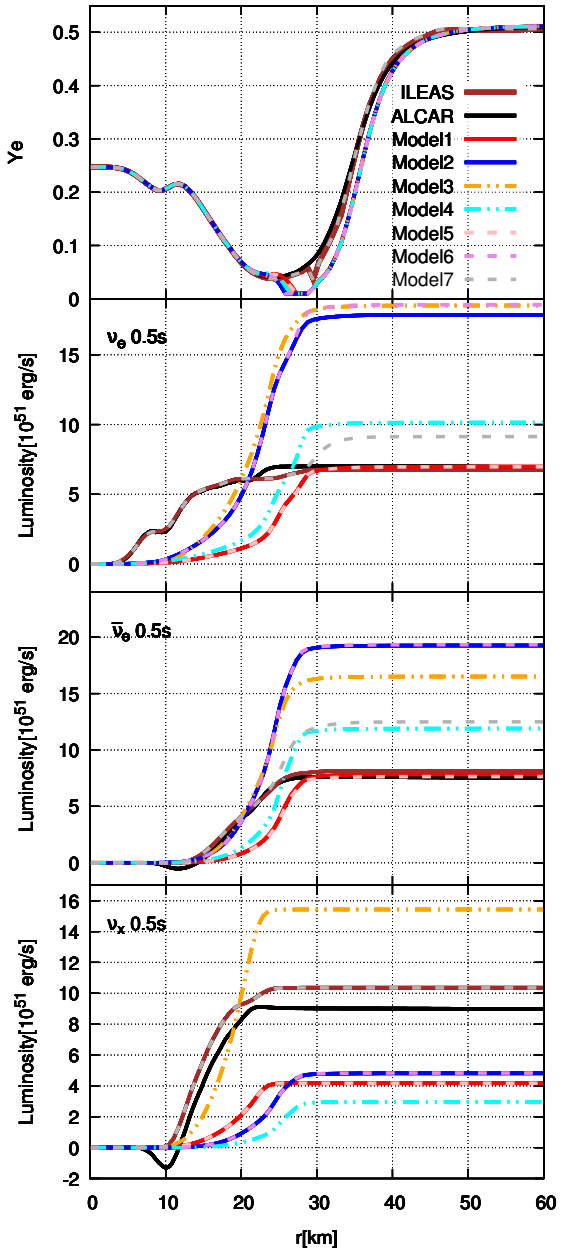

Figure A.1.: Radial profiles of the electron fraction and the neutrino luminosities of the three neutrino species obtained by the different leakage models summarized in table A.1, applied on a PNS snapshot (relaxed ALCAR background at 0.5 s post bounce). We did not include absorption or equilibration in any of the numbered models in order to focus on the differences of the leakage module alone. For comparison, we also plot the results obtained by ALCAR and ILEAS (with absorption and equilibration).

B. Neutrino reactions

In this appendix we collected the formulae for the different neutrino reactions (opacities and production rates) of all three neutrino species, employed in our scheme. Most reactions and their constants are extracted from Ruffert et al. (1996) and references therein. In this section, unlike in the body of this work, we employ only the superscript $Q^j_{\nu_i}$ with $j = 0, 1$ to denote number and energy rates respectively for reasons of compactness in the formulation. All production rates and opacities for ν_x include the contribution of all four species (ν_μ,$\bar{\nu}_\mu$,ν_τ and $\bar{\nu}_\tau$).

B.1. Opacities for diffusion

We define the energy-dependent absorption opacities, $\kappa_{\nu_i,\mathrm{a}}(\epsilon)$, following Bruenn (1985), with the correction of stimulated absorption (neutrino phase space blocking) from Rampp and Janka (2002),

$$\kappa^*_{\nu_i,\mathrm{a}}(\epsilon) \;=\; \kappa_{\nu_i,\mathrm{a}}(\epsilon)[1 - f(\epsilon;\eta^{\mathrm{eq}}_{\nu_i})]^{-1}. \tag{B.1}$$

Here, $f(\epsilon;\eta_i)) = [1+\exp((\epsilon/T)-\eta_i)]^{-1}$ is the distribution function of fermions with degeneracy parameter $\eta_i = \mu_i/T$ and energy ϵ. The superscript 'eq', in this case, denotes the usage of the equilibrium neutrino degeneracy instead of the interpolated one (see section 2.3). The opacity for ν_e absorption on neutrons, n, is given by

$$\begin{aligned}\kappa^*_{\nu_e,\mathrm{a}}(\epsilon) \;&=\; \frac{1+3g_A^2}{4}\sigma_0\xi_{np}\frac{[1-f(\epsilon+Q;\eta_{e^-})]}{[1-f(\epsilon;\eta^{\mathrm{eq}}_{\nu_e})]}\left(\frac{\epsilon+Q}{m_ec^2}\right)^2 \\ &\quad\cdot\left[1-\frac{(m_ec^2)^2}{(\epsilon+Q)^2}\right]^{\frac{1}{2}},\end{aligned} \tag{B.2}$$

and $\bar{\nu}_e$ absorption on protons, p, by

$$\begin{aligned}\kappa^*_{\bar{\nu}_e,\mathrm{a}}(\epsilon) \;&=\; \frac{1+3g_A^2}{4}\sigma_0\xi_{pn}\frac{[1-f(\epsilon-Q;\eta_{e^+})]}{[1-f(\epsilon;\eta^{\mathrm{eq}}_{\bar{\nu}_e})]}\left(\frac{\epsilon-Q}{m_ec^2}\right)^2 \\ &\quad\cdot\left[1-\frac{(m_ec^2)^2}{(\epsilon-Q)^2}\right]^{\frac{1}{2}}\Theta(\epsilon-Q-m_ec^2).\end{aligned} \tag{B.3}$$

Here c is the speed of light, $g_A \sim 1.25$, $\sigma_0 = 1.76{\cdot}10^{-44}\mathrm{cm}^2$ and m_e the electron mass. $[1 - f(\epsilon \pm Q;\eta_{e_\mp})]$ are the electron/positron phase space blocking factors and

ξ_{np} and ξ_{pn}[1] are related to the nucleon blocking factors Y_{np} and Y_{pn} as

$$\xi_{np} \;=\; (n_n + n_p)\cdot Y_{np} \;\equiv\; \mathcal{A}\rho\frac{Y_p - Y_n}{\mathrm{e}^{\eta_p-\eta_n}-1}, \tag{B.4}$$

and

$$\xi_{pn} \;=\; (n_n + n_p)\cdot Y_{pn} \;\equiv\; \mathcal{A}\rho\frac{Y_p - Y_n}{1-\mathrm{e}^{\eta_n-\eta_p}}, \tag{B.5}$$

where Y_p and Y_n are the proton and neutron number fractions, respectively and $\mathcal{A}$ is the Avogadro constant (Bruenn, 1985). As we pointed out in section 2.3, this formulation of the blocking factors assumes nucleons to be well represented by a free Fermi gas. In order to avoid unphysical behaviour, we make use of the free Fermi gas nucleon chemical potentials, which we calculate by inverting the relation (Rampp, 2000; Hecht, 1989),

$$n_N \;=\; \frac{4\pi}{(hc)^3}(2m_N T)^{3/2}F_{1/2}(\eta_N), \tag{B.6}$$

where N refers to the nucleon type, p or n.

If one assumes complete dissociation of matter in protons and neutrons, the nucleon fractions can be expressed as $Y_p = Y_e$ and $Y_n = (1 - Y_e)$, as in Ruffert et al. (1996). However, for more consistent comparison to ALCAR, we relaxed this assumption and employed the nucleon number densities obtained from the EoS. The Heaviside step function $\Theta(\epsilon - Q - m_e c^2)$ in equation (B.3) ensures that the opacity remains positive, setting the rest mass difference between particles on both sides of the interaction as the minimum energy for $\bar{\nu}_e$ absorption.

The transport opacities for neutrino-nucleon scattering of all three neutrino species are defined as

$$\kappa_{\nu_i,\mathrm{s}}(\epsilon) \;=\; C_N\sigma_0\xi_{NN}\left(\frac{\epsilon}{m_e c^2}\right)^2, \tag{B.7}$$

where $C_p = [4(C_V-1)^2 + 5g_A^2]/24$ and $C_n = (1+5g_A^2)/24$ with $C_V = 1/2 + 2\sin^2\theta_W$ and $\sin^2\theta_W = 0.23$. We define the nucleon Pauli blocking factor, Y_{NN}, following Mezzacappa and Bruenn (1993), as an interpolation between (non-relativistic) degenerate and non-degenerate limits:

$$\xi_{NN} \;=\; n_N\cdot Y_{NN} \;\equiv\; \mathcal{A}\rho Y_N\frac{\zeta_N}{\sqrt{1+\zeta_N^2}}, \tag{B.8}$$

$$\text{with}\;\; \zeta_N \;\equiv\; \frac{3T}{2E_N^F}, \tag{B.9}$$

where E_N^F is the Fermi energy of nucleon N,

$$E_N^F \;=\; \frac{h^2}{8\pi^2 m_b}\left(2\pi^2 n_N\right)^{2/3}. \tag{B.10}$$

[1]We relabelled the final state blocking ξ_N instead of η_N (Bruenn, 1985) to avoid confusion with degeneracy parameters.

Similarly, scattering on nuclei of mass number A can be expressed as,

$$\begin{aligned}\kappa_{\nu_i,\mathrm{s}}(\epsilon;A) &= \frac{1}{6}A^2\left[C_A - 1 + \frac{Z}{A}(2 - C_A - C_V)\right]^2 \\ &\quad \cdot \sigma_0 n_A \left(\frac{\epsilon}{m_e c^2}\right)^2,\end{aligned} \tag{B.11}$$

where $C_A = 1/2$, Z is the proton number of nuclei and n_A the nuclei number density. This equation is used both for scattering on heavy nuclei of average mass number and proton fraction $\bar{A}$ and $\bar{Z}$ and for scattering on α-particles ($A = 4$ and $Z = 2$).

The total opacities for each neutrino species, both for energy and number transport, are simply

$$\begin{aligned}\kappa_{\nu_e}(\epsilon) &= \kappa^*_{\nu_e,\mathrm{a}}(\epsilon) + \kappa_{\nu_e,\mathrm{s}}(\epsilon;n) + \kappa_{\nu_e,\mathrm{s}}(\epsilon;p) + \kappa_{\nu_e,\mathrm{s}}(\epsilon;\alpha) + \\ &\quad \kappa_{\nu_e,\mathrm{s}}(\epsilon;\bar{A}), \\ \kappa_{\bar{\nu}_e}(\epsilon) &= \kappa^*_{\bar{\nu}_e,\mathrm{a}}(\epsilon) + \kappa_{\bar{\nu}_e,\mathrm{s}}(\epsilon;n) + \kappa_{\bar{\nu}_e,\mathrm{s}}(\epsilon;p) + \kappa_{\bar{\nu}_e,\mathrm{s}}(\epsilon;\alpha) + \\ &\quad \kappa_{\bar{\nu}_e,\mathrm{s}}(\epsilon;\bar{A}), \\ \kappa_{\nu_x}(\epsilon) &= \kappa_{\nu_x,\mathrm{s}}(\epsilon;n) + \kappa_{\nu_x,\mathrm{s}}(\epsilon;p) + \kappa_{\nu_x,\mathrm{s}}(\epsilon;\alpha) + \kappa_{\nu_x,\mathrm{s}}(\epsilon;\bar{A}).\end{aligned} \tag{B.12}$$

These opacities are used for the calculation of the diffusion time-scales (equations 2.37 and 2.38) as explained in section 2.3.1.

B.2. Opacities for absorption and optical depth

We use spectrally averaged opacities to estimate the optical depth (equation 2.27) for the interpolation of the neutrino degeneracies (equation 2.25), as well as in the absorption module. For consistency with our production rates, we do not correct these opacities for stimulated absorption (equation B.1, see also the discussion in appendix C). Following Ruffert et al. (1996), we average the absorption opacities (ignoring electron rest-mass terms) as

$$\begin{aligned}\bar{\kappa}^j_{\nu_e,\mathrm{a}} &= \frac{\int_0^\infty \kappa_{\nu_e,\mathrm{a}}(\epsilon+Q)E^j_{\nu_e}(\epsilon)\mathrm{d}\epsilon}{\int_0^\infty E^j_{\nu_e}(\epsilon)\mathrm{d}\epsilon} \\ &= \frac{1+3g_A^2}{4(m_e c^2)^2}\sigma_0\xi_{np}\langle 1 - f(\bar{\epsilon}_{e^-};\eta_{e^-})\rangle \\ &\quad \cdot \frac{T^2 F_{4+j}(\eta_{\nu_e}) + 2QTF_{3+j}(\eta_{\nu_e}) + Q^2 F_{2+j}(\eta_{\nu_e})}{F_{2+j}(\eta_{\nu_e})},\end{aligned} \tag{B.13}$$

and

$$\begin{aligned}
\bar{\kappa}^{j}_{\bar{\nu}_e,\mathrm{a}} &= \frac{\int_0^\infty \kappa_{\bar{\nu}_e,\mathrm{a}}(\epsilon - Q) E^{j}_{\bar{\nu}_e}(\epsilon)\Theta(\epsilon - Q)\mathrm{d}\epsilon}{\int_0^\infty E^{j}_{\bar{\nu}_e}(\epsilon)\mathrm{d}\epsilon} \\
&= \frac{1+3g_A^2}{4(m_e c^2)^2}\sigma_0 \xi_{pn}\langle 1 - f(\bar{\epsilon}_{e^+};\eta_{e^+})\rangle \\
&\cdot \frac{T^2 F_{4+j}(\eta_{\bar{\nu}_e} - Q/T) + (2+j)QTF_{3+j}(\eta_{\bar{\nu}_e} - Q/T)}{F_{2+j}(\eta_{\bar{\nu}_e})} \\
&+ \frac{(1+2j)Q^2 F_{2+j}(\eta_{\bar{\nu}_e} - Q/T)}{F_{2+j}(\eta_{\bar{\nu}_e})} \\
&+ \frac{jQ^3 T^{-1} F_{1+j}(\eta_{\bar{\nu}_e} - Q/T)}{F_{2+j}(\eta_{\bar{\nu}_e})},
\end{aligned} \tag{B.14}$$

where T is the matter temperature, $E^{j}_{\nu_e}(\epsilon)$ is defined as equation (2.28) and $F_k = \int_0^\infty x^k f(x;\eta_{\nu_i})\mathrm{d}x$ are the Fermi integrals of order k of particle i, with $F_k(\eta_{e^\pm} \mp Q/T)$ evaluated including the nucleon rest mass correction to the lepton energy. In this averaging procedure, we consider the correction of the electron rest mass to the neutrino energy to be negligible. We also approximate the lepton blocking factors assuming the electron and positron mean production energies[2] to be

$$\bar{\epsilon}_{e^-} = T\frac{F_5(\eta_{e^-} - Q/T)}{F_4(\eta_{e^-})}, \tag{B.15}$$

$$\bar{\epsilon}_{e^+} = T\frac{F_5(\eta_{e^+})}{F_4(\eta_{e^+})}. \tag{B.16}$$

One can easily recover the results from Ruffert et al. (1996) by assuming the nucleon rest mass to be negligible, $\bar{\epsilon}_{e^-} \approx \bar{\epsilon}_{\nu_e}$ and $\bar{\epsilon}_{e^+} \approx \bar{\epsilon}_{\bar{\nu}_e}$.

Following the same procedure, the spectrally averaged scattering opacities read,

$$\bar{\kappa}^{j}_{\nu_i,\mathrm{s}} = C_N \sigma_0 \xi_{NN}\left(\frac{T}{m_e c^2}\right)^2 \frac{F_{4+j}(\eta_{\nu_i})}{F_{2+j}(\eta_{\nu_i})}, \tag{B.17}$$

for scattering on nucleons and,

$$\begin{aligned}
\bar{\kappa}^{j}_{\nu_i,\mathrm{s}}(A) &= \frac{1}{6}A^2\left[C_A - 1 + \frac{Z}{A}(2 - C_A - C_V)\right]^2 \\
&\sigma_0 n_A \left(\frac{T}{m_e c^2}\right)^2 \frac{F_{4+j}(\eta_{\nu_i})}{F_{2+j}(\eta_{\nu_i})},
\end{aligned} \tag{B.18}$$

for scattering on α-particles and heavy nuclei. Like for the energy-dependent opacities (equation B.12), we define the total number ($j = 0$) and energy ($j = 1$) averaged

[2]Note that produced e^- will have a minimum energy $\epsilon^{\min}_{e^-} = Q$.

opacities as,

$$\begin{aligned}
\bar{\kappa}^j_{\nu_e} &= \bar{\kappa}^j_{\nu_e,\mathrm{a}} + \bar{\kappa}^j_{\nu_e,\mathrm{s}}(n) + \bar{\kappa}^j_{\nu_e,\mathrm{s}}(p) + \bar{\kappa}^j_{\nu_e,\mathrm{s}}(\alpha) + \\
&\quad \bar{\kappa}^j_{\nu_e,\mathrm{s}}(\bar{A}), \\
\bar{\kappa}^j_{\bar{\nu}_e} &= \bar{\kappa}^j_{\bar{\nu}_e,\mathrm{a}} + \bar{\kappa}^j_{\bar{\nu}_e,\mathrm{s}}(n) + \bar{\kappa}^j_{\bar{\nu}_e,\mathrm{s}}(p) + \bar{\kappa}^j_{\bar{\nu}_e,\mathrm{s}}(\alpha) + \\
&\quad \bar{\kappa}^j_{\bar{\nu}_e,\mathrm{s}}(\bar{A}), \\
\bar{\kappa}^j_{\nu_x} &= \bar{\kappa}^j_{\nu_x,\mathrm{s}}(n) + \bar{\kappa}^j_{\nu_x,\mathrm{s}}(p) + \bar{\kappa}^j_{\nu_x,\mathrm{s}}(\alpha) + \bar{\kappa}^j_{\nu_x,\mathrm{s}}(\bar{A}).
\end{aligned} \tag{B.19}$$

Finally, in the calculation of the neutrino absorption rates, spectrally averaged absorption opacities are calculated as in equations (B.13) and (B.14), but employing the neutrino spectrum from the corresponding ray, as defined in section 2.4.

B.3. Production rates

The β-processes are the main (far dominant) production sources of ν_e and $\bar{\nu}_e$. From the emissivities obtained by Bruenn (1985), we define the corresponding spectrally averaged production rates (including nucleon rest mass corrections) as

$$\begin{aligned}
Q^j_{\nu_e,\beta} &= \frac{1+3g_A^2}{8}\frac{\sigma_0 c}{(m_e c^2)^2}\xi_{pn}\langle 1 - f(\bar{\epsilon}^\beta_{\nu_e};\eta_{\nu_e})\rangle \\
&\quad \cdot \frac{8\pi}{(hc)^3}\left[T^{5+j}F_{4+j}(\eta_{e^-} - Q/T)\right. \\
&\quad + 2QT^{4+j}F_{3+j}(\eta_{e^-} - Q/T) \\
&\quad \left. + Q^2T^{3+j}F_{2+j}(\eta_{e^-} - Q/T)\right],
\end{aligned} \tag{B.20}$$

for ν_e and

$$\begin{aligned}
Q^j_{\bar{\nu}_e,\beta} &= \frac{1+3g_A^2}{8}\frac{\sigma_0 c}{(m_e c^2)^2}\xi_{np}\langle 1 - f(\bar{\epsilon}^\beta_{\bar{\nu}_e};\eta_{\bar{\nu}_e})\rangle \\
&\quad \cdot \frac{8\pi}{(hc)^3}\left[T^{5+j}F_{4+j}(\eta_{e^+})\right. \\
&\quad + (2+j)QT^{4+j}F_{3+j}(\eta_{e^+}) \\
&\quad + (1+2j)Q^2T^{3+j}F_{2+j}(\eta_{e^+}) \\
&\quad \left. + jQ^3T^{2+j}F_{1+j}(\eta_{e^+})\right],
\end{aligned} \tag{B.21}$$

for $\bar{\nu}_e$. All quantities and constants are defined as in section B.1. The ν_e and $\bar{\nu}_e$ mean production energies[3] are approximated in analogy of equations (B.15) and (B.16) as,

$$\bar{\epsilon}^\beta_{\nu_e} = T\frac{F_5(\eta_{\nu_e})}{F_4(\eta_{\nu_e})}. \tag{B.22}$$

$$\bar{\epsilon}^\beta_{\bar{\nu}_e} = T\frac{F_5(\eta_{\bar{\nu}_e} - Q/T)}{F_4(\eta_{\bar{\nu}_e})}. \tag{B.23}$$

[3]Note that produced $\bar{\nu}_e$ will have a minimum energy $\epsilon^{\min}_{\bar{\nu}_e} = Q$..

Since the neutrino phase space blocking is small in the neutrino production dominated regions, the approximate average value employed in Ruffert et al. (1996), $[1 - f(\epsilon; \eta_{\nu_i})] \simeq \langle 1 - f(\bar{\epsilon}; \eta_{\nu_i})\rangle$, is very reasonable. We caution the reader that for the tests presented in section 3 the β-production rates were implemented following Rampp and Janka (2002), as is explained in detail in appendix C.

Thermal processes such as electron-positron pair annihilation are also an important source of neutrino pairs of all three species. Following Cooperstein et al. (1986, 1987), the ν_e and $\bar{\nu}_e$ production rates read

$$\begin{aligned} Q^j_{\nu_e,\bar{\nu}_e,ee} &= \frac{(C_1 + C_2)_{\nu_e\bar{\nu}_e}}{72} \frac{\sigma_0 c}{(m_e c^2)^2} \\ &\cdot \langle 1 - f(\bar{\epsilon}^{ee}_{e_i}; \eta_{\nu_e})\rangle \langle 1 - f(\bar{\epsilon}^{ee}_{e_i}; \eta_{\bar{\nu}_e})\rangle \\ &\cdot \left[\frac{8\pi}{(hc)^3}\right]^2 \left[T^{4+j} F_{3+j}(\eta_{e^-}) T^4 F_3(\eta_{e^+}) + \right. \\ &\left. T^4 F_3(\eta_{e^-}) T^{4+j} F_{3+j}(\eta_{e^+})\right], \end{aligned} \tag{B.24}$$

where the constants $(C_1 + C_2)_{\nu_e\bar{\nu}_e} = (C_V - C_A)^2 + (C_V + C_A)^2$, with C_A and C_V as defined in section B.1. Again, the mean neutrino energy in the neutrino phase space blocking is approximated as Ruffert et al. (1996),

$$\bar{\epsilon}^{ee}_{e_i} = T\left(\frac{1}{2}\frac{F_4(\eta_{e^-})}{F_3(\eta_{e^-})} + \frac{1}{2}\frac{F_4(\eta_{e^+})}{F_3(\eta_{e^+})}\right). \tag{B.25}$$

It is worth noting that the rates above are for each individual neutrino species. When comparing with the source material (Cooperstein et al., 1986, 1987), one should keep in mind that the energy production rate of ν_i is half of the energy of the produced pair, whereas the number production rate of ν_i is the same as the pair production rate.

For heavy-lepton neutrinos, the production rate via electron-positron annihilation for all 4 species is expressed as,

$$\begin{aligned} Q^j_{\nu_x,ee} &= \frac{(C_1 + C_2)_{\nu_x\nu_x}}{18} \frac{\sigma_0 c}{(m_e c^2)^2} \left(\langle 1 - f(\bar{\epsilon}^{ee}_{e_i}; \eta_{\nu_x})\rangle\right)^2 \\ &\cdot \left[\frac{8\pi}{(hc)^3}\right]^2 \left[T^{4+j} F_{3+j}(\eta_{e^-}) T^4 F_3(\eta_{e^+}) + \right. \\ &\left. T^4 F_3(\eta_{e^-}) T^{4+j} F_{3+j}(\eta_{e^+})\right], \end{aligned} \tag{B.26}$$

with $(C_1 + C_2)_{\nu_x\nu_x} = (C_V - C_A)^2 + (C_V + C_A - 2)^2$.

Finally, transversal plasmon decay will also contribute to the creation of all three

neutrino species with a production rate described by

$$Q^j_{\nu_e,\bar{\nu}_e,\gamma} \approx \frac{\pi^3}{3\alpha^*} C_V^2 \frac{\sigma_0 c}{(m_e c^2)^2} \frac{T^8}{(hc)^6} \gamma^6 \mathrm{e}^{-\gamma}(1+\gamma) \cdot \langle 1 - f(\bar{\epsilon}^\gamma_{e_i}; \eta_{\nu_e})\rangle \langle 1 - f(\bar{\epsilon}^\gamma_{e_i}; \eta_{\bar{\nu}_e})\rangle \left[\frac{1}{2} T \left(2 + \frac{\gamma^2}{1+\gamma}\right)\right]^j, \quad \text{(B.27)}$$

for ν_e and $\bar{\nu}_e$, and

$$Q^j_{\nu_x,\gamma} \approx \frac{4\pi^3}{3\alpha^*} (C_V - 1)^2 \frac{\sigma_0 c}{(m_e c^2)^2} \frac{T^8}{(hc)^6} \gamma^6 \mathrm{e}^{-\gamma}(1+\gamma) \left(\langle 1 - f(\bar{\epsilon}^\gamma_{e_i}; \eta_{\nu_x})\rangle\right)^2 \left[\frac{1}{2} T \left(2 + \frac{\gamma^2}{1+\gamma}\right)\right]^j, \quad \text{(B.28)}$$

for all ν_x together. $\alpha^* = 1/137.036$ is the fine structure constant and $\gamma = 5.565{\cdot}10^{-2} \sqrt{1/3(\pi^2 + 3\eta^2_{e^-})}$. The mean energy of neutrinos produced via plasmon decay is taken as

$$\bar{\epsilon}^\gamma_{e_i} = \left[\frac{1}{2} T \left(2 + \frac{\gamma^2}{1+\gamma}\right)\right]. \quad \text{(B.29)}$$

In addition to the reactions included in Ruffert et al. (1996), we incorporate the production of ν_x via nucleon-nucleon bremsstrahlung, which has been shown to have a significant contribution to the production of heavy-lepton neutrinos. For the total energy production rate (four ν_x species together), we employ the prescription of Thompson et al. (2000):

$$Q^{j=1}_{\nu_x,\mathrm{brems}} = 2.08{\cdot}10^2 \xi_{\mathrm{brems}} \left(Y_n^2 + Y_p^2 + \frac{28}{3} Y_n Y_p\right) \rho T^{5.5}. \quad \text{(B.30)}$$

Following Burrows et al. (2006), we set the constant $\xi_{\mathrm{brems}} = 0.5$, which is its approximate value at the typical neutrinosphere conditions in PNSs. The factor of 2 higher numerical value of equation (B.30) compared with Burrows et al. (2006) comes from the fact that we include two neutrino pairs ($\nu_\mu\bar{\nu}_\mu$ and $\nu_\tau\bar{\nu}_\tau$) in ν_x. In order to estimate a number production rate, we make an assumption of the average neutrino energy (Hannestad and Raffelt, 1998),

$$\bar{\epsilon}^{\mathrm{brems}}_{\nu_x} \sim 3T, \quad \text{(B.31)}$$

namely, that all the kinetic energy of the nucleons is transferred to the created neutrinos. Then, the total number production rate is simply,

$$Q^{j=0}_{\nu_x,\mathrm{brems}} = \frac{Q_{\nu_x,\mathrm{brems}}}{\bar{\epsilon}^{\mathrm{brems}}_{\nu_x}}. \quad \text{(B.32)}$$

for ν_x of all kinds in total.

The total neutrino production rates are then written as,

$$\begin{aligned} R_{\nu_e} &= Q^{j=0}_{\nu_e,\beta} + Q^{j=0}_{\nu_e,\bar{\nu}_e,ee} + Q^{j=0}_{\nu_e,\bar{\nu}_e,\gamma}, \\ R_{\bar{\nu}_e} &= Q^{j=0}_{\bar{\nu}_e,\beta} + Q^{j=0}_{\nu_e,\bar{\nu}_e,ee} + Q^{j=0}_{\nu_e,\bar{\nu}_e,\gamma}, \\ R_{\nu_x} &= Q^{j=0}_{\nu_x,ee} + Q^{j=0}_{\nu_x,\gamma} + Q^{j=0}_{\nu_x,\mathrm{brems}}, \end{aligned} \tag{B.33}$$

for numbers of ν_e, $\bar{\nu}_e$ and all kinds of ν_x,respectively, and

$$\begin{aligned} Q_{\nu_e} &= Q^{j=1}_{\nu_e,\beta} + Q^{j=1}_{\nu_e,\bar{\nu}_e,ee} + Q^{j=1}_{\nu_e,\bar{\nu}_e,\gamma}, \\ Q_{\bar{\nu}_e} &= Q^{j=1}_{\bar{\nu}_e,\beta} + Q^{j=1}_{\nu_e,\bar{\nu}_e,ee} + Q^{j=1}_{\nu_e,\bar{\nu}_e,\gamma}, \\ Q_{\nu_x} &= Q^{j=1}_{\nu_x,ee} + Q^{j=1}_{\nu_x,\gamma} + Q^{j=1}_{\nu_x,\mathrm{brems}}, \end{aligned} \tag{B.34}$$

for energy of ν_e, $\bar{\nu}_e$ and all kinds of ν_x,respectively.

C. Production rates and opacities used for tests

As we noted in section 3.1, there exists certain ambiguity in the derivation of the neutrino β-production rates, which could become a source of uncertainty in our neutrino treatment.

Following the derivation by Bruenn (1985), the rate of change of the neutrino distribution function due to β-interactions (emission and absorption), $Q^{\rm tot}_{\nu_i}$, is proportional to

$$Q^{\rm tot}_{\nu_i} \;\propto\; j_{\nu_i}(\epsilon)\left[1-f(\epsilon;\eta_{\nu_i})\right] - f(\epsilon;\eta_{\nu_i})\kappa_{\nu_i,{\rm a}}(\epsilon). \tag{C.1}$$

On one hand, one can derive the neutrino production rates from the neutrino emissivities as,

$$Q^{j}_{\nu_i} \;=\; \frac{4\pi c}{(hc)^3}\int_0^\infty \epsilon^{2+j} j_{\nu_i}(\epsilon)[1-f(\epsilon;\eta_{\nu_i})]{\rm d}\epsilon, \tag{C.2}$$

where $[1-f(\epsilon;\eta_{\nu_i})]$ accounts for the neutrino final state blocking, and the neutrino emissivities are defined as in Bruenn (1985),

$$j_{\nu_e}(\epsilon) \;=\; \frac{\sigma_0(1+3g_A^2)}{4m_e^2c^4}\xi_{pn} f(\epsilon+Q;\eta_{e^-})(\epsilon+Q)^2 \tag{C.3}$$

$$\cdot\sqrt{1-\frac{m_e^2c^4}{(\epsilon+Q)^2}}, \tag{C.4}$$

for ν_e and

$$j_{\bar\nu_e}(\epsilon) \;=\; \frac{\sigma_0(1+3g_A^2)}{4m_e^2c^4}\xi_{np} f(\epsilon-Q;\eta_{e^+})(\epsilon-Q)^2 \tag{C.5}$$

$$\cdot\sqrt{1-\frac{m_e^2c^4}{(\epsilon-Q)^2}}, \tag{C.6}$$

for $\bar\nu_e$. This formulation corresponds to the one adopted for the presented ILEAS scheme, as detailed in appendix B.

On the other hand, one can use the Kirchhoff-Planck relation,

$$\kappa_{\nu_i,{\rm a}} f(\epsilon;\eta^{\rm eq}_{\nu_i}) \;=\; j_{\nu_i}(\epsilon)\left[1-f(\epsilon;\eta^{\rm eq}_{\nu_i})\right], \tag{C.7}$$

to define a corrected absorption opacity, which includes the effects of stimulated absorption (Rampp and Janka, 2002),

$$\kappa^*_{\nu_i,\mathrm{a}}(\epsilon) = \frac{1}{1-f(\epsilon;\eta^{\mathrm{eq}}_{\nu_i})}\kappa_{\nu_i,\mathrm{a}}(\epsilon) \tag{C.8}$$

$$= j_{\nu_i}(\epsilon)+\kappa_{\nu_i,\mathrm{a}}(\epsilon), \tag{C.9}$$

as we described in equations (B.13) and (B.14). Then, equation (C.1) can be rewritten as,

$$Q^{\mathrm{tot}}_{\nu_i} \propto \kappa^*_{\nu_i,\mathrm{a}}(\epsilon)\left[f(\epsilon;\eta^{\mathrm{eq}}_{\nu_i})-f(\epsilon;\eta_{\nu_i})\right]. \tag{C.10}$$

This expression is *exactly* equivalent to equation (C.1), and can be interpreted as a redefinition of emission and absorption, with $\kappa^*_{\nu_i,\mathrm{a}}(\epsilon)$ as the new opacity and $j^*_{\nu_i}(\epsilon) = j_{\nu_i}(\epsilon)f(\epsilon;\eta^{\mathrm{eq}}_{\nu_i})\left[1-f(\epsilon;\eta_{\nu_i})\right]^{-1}$ as the new emissivity. The production rates can then be calculated accordingly, as

$$Q^{*,j}_{\nu_i} = \frac{4\pi c}{(hc)^3}\int_0^\infty \epsilon^{2+j}\kappa^*_{\nu_i,\mathrm{a}}(\epsilon)f(\epsilon;\eta^{\mathrm{eq}}_{\nu_i})\mathrm{d}\epsilon. \tag{C.11}$$

This formulation is adopted by many truncated moment schemes (Rampp and Janka, 2002; Just et al., 2015b) because it simplifies the computation of neutrino interactions to $\kappa^*_{\nu_i,\mathrm{a}}(\epsilon)$, instead of calculating the emissivities and opacities separately. Both codes employed in the comparisons presented in section 3, ALCAR and VERTEX, make use of this description. For this reason, we have also implemented this formulation of the β-production rates in ILEAS and used it for such tests. In order to be fully consistent, this reformulation requires to employ the corrected absorption opacities for the neutrino absorption scheme as well. This translates to redefining the opacities in equations (B.13) and (B.14) as

$$\begin{aligned}\bar{\kappa}^{*,j}_{\nu_e,\mathrm{a}} &= \frac{\int_0^\infty \kappa^*_{\nu_e,\mathrm{a}}(\epsilon+Q)E^j_{\nu_e}(\epsilon)\mathrm{d}\epsilon}{\int_0^\infty E^j_{\nu_e}(\epsilon)\mathrm{d}\epsilon}\\ &= \frac{1+3g_A^2}{4(m_ec^2)^2}\sigma_0\xi_{np}\frac{\langle 1-f(\bar{\epsilon}_{e^-};\eta_{e^-})\rangle}{\langle 1-f(\bar{\epsilon}_{\nu_e};\eta^{\mathrm{eq}}_{\nu_e})\rangle}\\ &\cdot\frac{T^2F_{4+j}(\eta_{\nu_e})+2QTF_{3+j}(\eta_{\nu_e})+Q^2F_{2+j}(\eta_{\nu_e})}{F_{2+j}(\eta_{\nu_e})},\end{aligned} \tag{C.12}$$

and

$$\bar{\kappa}^{*,j}_{\bar{\nu}_e,\mathrm{a}} = \frac{\int_0^\infty \kappa^*_{\bar{\nu}_e,\mathrm{a}}(\epsilon - Q)E^j_{\bar{\nu}_e}(\epsilon)\Theta(\epsilon - Q)\mathrm{d}\epsilon}{\int_0^\infty E^j_{\bar{\nu}_e}(\epsilon)\mathrm{d}\epsilon} \tag{C.13}$$

$$\begin{aligned} &= \frac{1+3g_A^2}{4(m_e c^2)^2}\sigma_0 \xi_{pn} \frac{\langle 1 - f(\bar{\epsilon}_{e^+}; \eta_{e^+})\rangle}{\langle 1 - f(\bar{\epsilon}_{\bar{\nu}_e}; \eta^{\mathrm{eq}}_{\bar{\nu}_e})\rangle} \\ &\cdot \frac{T^2 F_{4+j}(\eta_{\bar{\nu}_e} - Q/T) + (2+j)QTF_{3+j}(\eta_{\bar{\nu}_e} - Q/T)}{F_{2+j}(\eta_{\bar{\nu}_e})} \\ &+ \frac{(1+2j)Q^2 F_{2+j}(\eta_{\bar{\nu}_e} - Q/T)}{F_{2+j}(\eta_{\bar{\nu}_e})} \\ &+ \frac{jQ^3 T^{-1} F_{1+j}(\eta_{\bar{\nu}_e} - Q/T)}{F_{2+j}(\eta_{\bar{\nu}_e})}, \end{aligned} \tag{C.14}$$

and using them instead of $\bar{\kappa}^{\mathrm{a}}_{\nu_i}$ for equations (2.41) and (2.44) in the absorption algorithm. The electron, positron, ν_e and $\bar{\nu}_e$ mean energies are calculated as in equations (B.15), (B.16), (B.22) and (B.23), respectively

We remind the reader that for the tests presented in section 3 we employed only the reactions included in table 3.1 in order to consistently compare our results with those obtained by the ALCAR and VERTEX codes. The total neutrino production rates used for such tests are,

$$\begin{aligned} R_{\nu_e} &= Q^{*,j=0}_{\nu_e,\beta}, \\ R_{\bar{\nu}_e} &= Q^{*,j=0}_{\bar{\nu}_e,\beta}, \\ R_{\nu_x} &= Q^{j=0}_{\nu_x,ee} + Q^{j=0}_{\nu_x,\mathrm{brems}}, \end{aligned} \tag{C.15}$$

and

$$\begin{aligned} Q_{\nu_e} &= Q^{*,j=1}_{\nu_e,\beta}, \\ Q_{\bar{\nu}_e} &= Q^{*,j=1}_{\bar{\nu}_e,\beta}, \\ Q_{\nu_x} &= Q^{j=1}_{\nu_x,ee} + Q^{j=1}_{\nu_x,\mathrm{brems}}, \end{aligned} \tag{C.16}$$

for number and energy, respectively, with the β-production rates described in equation (C.11).

For a given nucleon species, n or p, equation (C.2) and equation (C.11) employ different nucleon blocking factors, either (B.4) or (B.5). These two blocking factors obey the relation (Bruenn, 1985),

$$\xi_{np} = e^{(\eta_e - \eta^{\mathrm{eq}}_{\nu_i})}\xi_{pn}. \tag{C.17}$$

Employing this relation, and the general mathematical property of Fermi functions, $f(x)$,

$$e^x = \frac{1 - f(x)}{f(x)}, \tag{C.18}$$

the two definitions of the β-production rates in equations (C.2) and (C.11) are, considering equation (C.7), equivalent except for a factor $[1 - f(\epsilon; \eta_{\nu_i})]^{-1}$ in the integrand of equation (C.11). This factor, which corresponds to the neutrino phase space blocking, amounts to a $1 - 2$ per cent correction on the local rates, which is accounted for by the correct redefinition of the absorption opacities in equations (C.12) and (C.14).

There is, however, a more subtle, yet important difference between equations (C.2) and (C.11). Our definitions of the nucleon phase space blocking (equations B.4 and B.5) assume nucleons behave like a free Fermi gas and, accordingly, employ the free Fermi gas nucleon chemical potentials in their calculation (equation B.6). As we already pointed out in section 2.3, it is essential to use the free Fermi gas chemical potentials, instead of the ones provided by the EoS, in order to avoid unphysical behaviour of the blocking factors (becoming negative, bigger than unity or not fulfilling the non-degenerate limits). This inconsistency between the nucleon degeneracies employed in the nucleon blocking factors (free Fermi gas, see equations B.4 and B.5) and in the calculation of the neutrino equilibrium degeneracies (EoS, see equations 2.25 and 2.26), is a source of discrepancy between the two approaches.

Because we employ the free Fermi gas nucleon chemical potentials in the blocking factors, $\eta_{\nu_i}^{\mathrm{eq}}$ in equation C.17 is different than the one obtained from the high-density EoS (which considers nucleons as interacting particles) by equation (2.26). In order to be able to recover (C.2) from (C.11) (except for a factor $[1 - f(\epsilon; \eta_{\nu_i})]^{-1}$), or vice versa, the same nucleon chemical potentials would need to be used consistently. Because in our formulation this is not the case, there appear notable differences between both rates in the regimes where the nucleon interactions (and thus deviations between the two values of $\eta_{\nu_i}^{\mathrm{eq}}$) become important. These differences are illustrated in figure C.1, which shows the logarithm of the ν_e and $\bar{\nu}_e$ β-production rates calculated following both approaches (equations C.2 and C.11) on a PNS snapshot (ALCAR snapshot at 0.5 s post-bounce).

However, at the high optical depth at which this discrepancy exists, the neutrino transport is dominated by diffusion. As a consequence, even though the production rates differ considerably in the two approaches, neutrino luminosities are vastly produced by the diffusion behaviour, and the impact of the prescription chosen for the production rates is small. In figure C.2 this small effect in the luminosities (less than 5 per cent) can be appreciated. We conclude thus, that the choice of formulation of the β-production rates is not significantly relevant for the present work, as its associated uncertainty lies well within the differences between the results obtained by ILEAS in comparison to more sophisticated transport schemes (section 3). If higher accuracy would be desired, mean-field effects should be taken into account in the nucleon-neutrino interactions. We refer the reader to Reddy et al. (1998) for details on the original formulation, and Roberts (2012); Roberts et al. (2012); Martínez-Pinedo et al. (2012) for the implementation and application of such corrections in the context of SN and PNS cooling simulations.

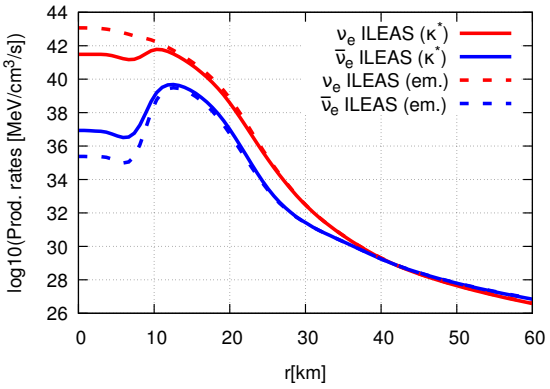

Figure C.1.: Neutrino β-production energy rates derived from the modified opacities (lines) and from the emissivities (dashed) for the ALCAR snapshot at 0.5 s post-bounce.

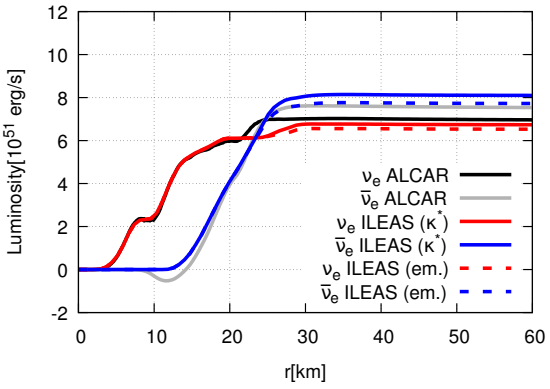

Figure C.2.: Neutrino luminosity profiles of ν_e and $\bar{\nu}_e$ obtained by ILEAS after 5 ms relaxation, employing the β-production rates derived from the modified opacities (lines) and from the emissivities (dashed), for the ALCAR relaxed snapshot at 0.5 s. The results obtained by ALCAR are also shown for comparison.

D. SPH rendering to a grid

It is widely known that SPH codes produce relatively spiky data, with occasional particles displaying a considerably larger or lower value for a given quantity, with respect to its neighbours. This undesirable behaviour can be of significant importance when calculating weak interaction rates, which depend on high powers of the temperature. It is thus advisable in any SPH code to smooth the thermodynamical quantities, specially the temperature, before applying any neutrino scheme. As mentioned in section 2.2, we decided to implement ILEAS on a 3D Cartesian grid for better comparison with grid based codes and, therefore, we naturally smooth the SPH quantities by rendering them onto a grid. This procedure, however, is not unambiguous, as can be seen in Price (2007), where the author developed an SPH rendering tool (SPLASH) for plotting purposes, or in Röttgers and Arth (2018). Unable to rely on a sophisticated rendering code such as SPLASH during our merger simulations, we tested different rendering procedures on several snapshots from a NS merger simulation, which we describe briefly hereunder.

The *standard* approach suggested in Price (2007) for rendering a given quantity A from SPH particles (A_j) to a grid ($\langle A(\boldsymbol{r})\rangle$), derives directly from the SPH discretization, as a summation over the particles whose kernel overlaps with a grid point, $\boldsymbol{r}$ (we refer the reader to section 2.1 for details on the SPH notation):

$$\langle A_{\rm std}(\boldsymbol{r})\rangle \;=\; \sum_j \frac{m_j}{\rho_j^*} A_j W(|\boldsymbol{r}-\boldsymbol{r}_j|, h_j). \tag{D.1}$$

Here m_j and ρ_j^* are the mass and conserved rest mass density, respectively, of a particle with index j. One can alternatively *normalize* this expression, by dividing it by the interpolation of unity,

$$\langle A_{\rm norm}(\boldsymbol{r})\rangle \;=\; \frac{\langle A_{\rm std}(\boldsymbol{r})\rangle}{\sum_j \frac{m_j}{\rho_j^*} W(|\boldsymbol{r}-\boldsymbol{r}_j|, h_j)}. \tag{D.2}$$

As Price (2007) suggests, this normalization is desirable to avoid a misestimation of the rendered quantity in locations with low SPH particle count. However, this approach is known to cause a blur effect when rendering the edges of a solid object.

Expression (D.2) allows for the straightforward inclusion of a weighing factor, such as ρ^*, in order to smooth the rendered data (ρ^*-*weighted*). Such modification is achieved by rendering the quantity $A_j\rho_j^*$ instead, and normalizing by the interpolated ρ^*, as

$$\langle A_\rho(\boldsymbol{r})\rangle \;=\; \frac{\sum_j \frac{m_j}{\rho_j^*} A_j \rho_j^* W(|\boldsymbol{r}-\boldsymbol{r}_j|, h_j)}{\sum_j \frac{m_j}{\rho_j^*} \rho_j^* W(|\boldsymbol{r}-\boldsymbol{r}_j|, h_j)}. \tag{D.3}$$

Recently, Röttgers and Arth (2018) have suggested a few modifications (*S-binning*) to the procedures discussed in Price (2007), which are worth exploring. First, they introduce a new weighting factor, S_j, which is the integral of the SPH particle's kernel discretized over the grid,

$$S_j \;=\; \sum_{\boldsymbol{k}} V_{\boldsymbol{k}} W(|\boldsymbol{r}_{\boldsymbol{k}} - \boldsymbol{r}_j|, h_j), \tag{D.4}$$

with the cell volume, $V_{\boldsymbol{k}}$, and the sumation over all grid points $\boldsymbol{k}$. Notice that in the limit of an infinitely small cell size, $S \to 1$. Then we can rewrite equation D.2 (for all particles j which fulfil $S > 0$) as

$$\langle A_{\mathrm{Sbin}}(\boldsymbol{r})\rangle \;=\; \frac{\sum_j \frac{m_j}{\rho_j^*} S^{-1} A_j W(|\boldsymbol{r} - \boldsymbol{r}_j|, h_j)}{\sum_j \frac{m_j}{\rho_j^*} S^{-1} W(|\boldsymbol{r} - \boldsymbol{r}_j|, h_j)}. \tag{D.5}$$

This ensures that any given particle contributes with its whole A_j to the grid (see Röttgers and Arth 2018 for examples). In order to take into account the contributions of particles which *fall through the grid*, i.e. particles whose kernel does not overlap with any grid point (and thus $S = 0$), they are added to the nearest grid point as

$$\langle A_{\mathrm{Sbin}}(\boldsymbol{r})\rangle \;=\; \langle A_{\mathrm{Sbin}}(\boldsymbol{r})\rangle + \frac{\left(m_j/\rho_j^*\right) A_j}{V_{\boldsymbol{k}}} \tag{D.6}$$

For particles intersecting with the grid boundaries, they suggest to set $S = 1$, which reduces equation D.5 to D.2 for that particle's contribution to the rendered value.

In most scenarios, all the presented rendering procedures yield comparable results, even with more sophisticated plotting tools such as SPLASH, as figures D.1,D.2 and D.3 demonstrate. However, the matter configuration obtained during the NS collision (up to ~ 1 ms post merger), poses a real problem. The different rendering approaches yield significantly different results in such violent conditions, even when using SPLASH, as can be seen in figures D.4,D.5 and D.6. As we mentioned earlier, there is no perfect way of rendering SPH particles to a grid. All the models we introduced perform better in some circumstances than in others, and thus, it is necessary to make a choice based on the available information. With this in mind, we consider the rendering described by equation (D.3) as the best candidate, and thus we employ it for the simulations carried out in this work.

The motivation for our choice can be traced mainly to figure D.6. The panels situated on the right column, as well as the centre left panel, display striking artefacts, which are inadmissible if we strive to obtain meaningful results. In this figure, one would expect to see the two neutron rich ($Y_e \lesssim 0.1$) NSs surrounded by an environment of slightly higher Y_e, raised by the interactions with the neutrinos emitted from the hot collision interface. This is the picture described by the top-left and bottom-left panels, which rely on the mapping described by equation (D.3). Furthermore, the higher temperatures (figure D.5) and densities (figure D.6) obtained by this same prescription, are more in the line of what one would expect at this stage

of the NS merger. However, it is also important to keep in mind, that the better performance of our chosen rendering procedure in the scenarios we tested does not exclude some pathological behaviour under other specific conditions.

In this section we showed that SPH rendering can be a major source of uncertainty in our models if not handled properly and, based on the presented tests, we choose the rendering procedure described by equation (D.3) for the NS merger models presented in this work. However, in order to fully understand the limitations of the chosen approach, a more detailed study on the topic should be considered in future work.

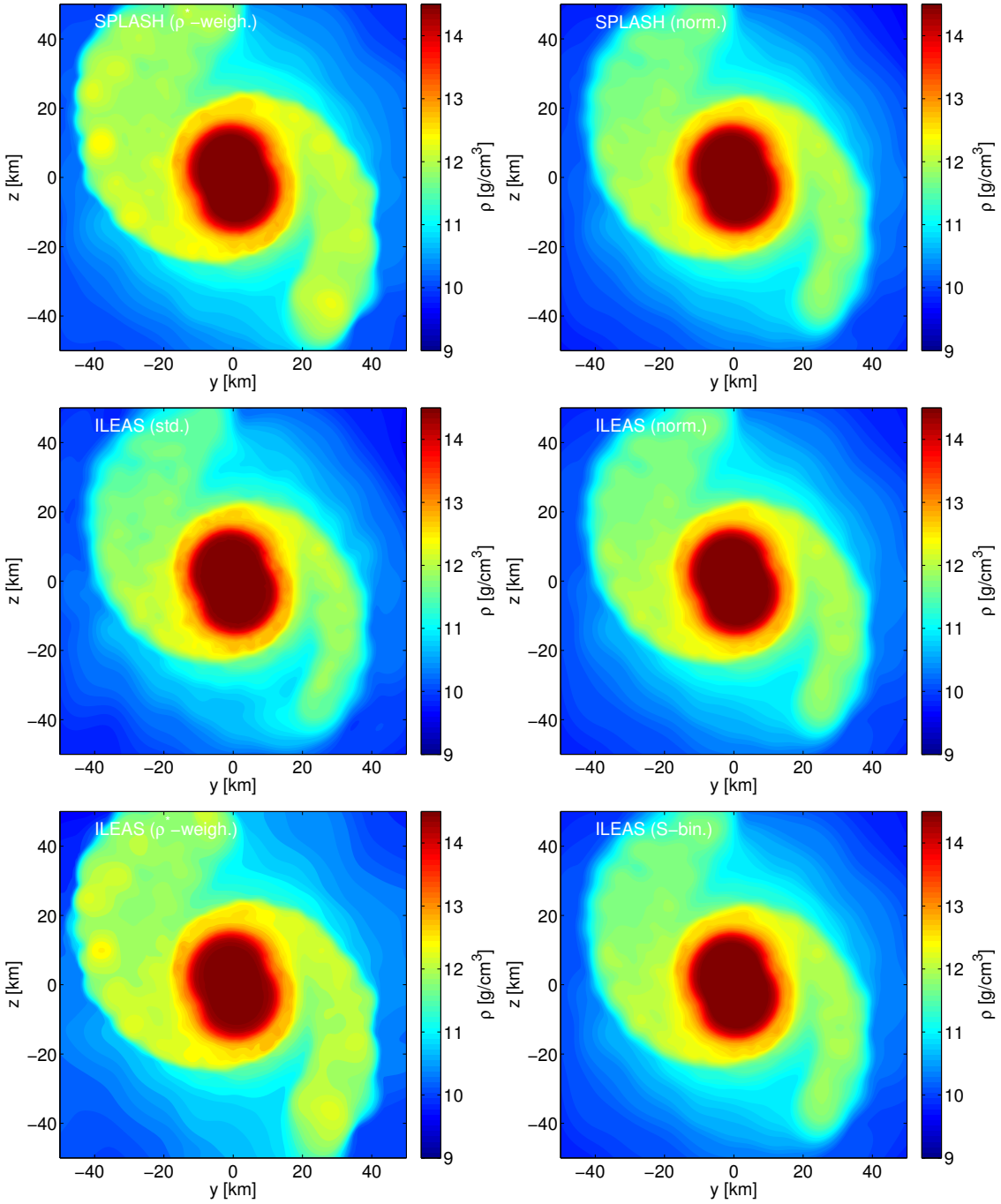

Figure D.1.: Rest mass density in the horizontal plane of a symmetric NS merger with 1.35 $M_\odot$ NSs and the DD2 EoS at 3 ms after the merger. Each panel shows the results obtained by different rendering procedures from SPH particles to a Cartesian grid. The programs and methods used for the rendering are: *top-left:* SPLASH (ρ^*-weighted, equation D.3), *top-right:* SPLASH (normalized, equation D.2), *centre-left:* ILEAS (standard, equation D.1), *centre-right:* ILEAS (normalized, equation D.3), *bottom-left:* ILEAS (ρ^*-weighted, equation D.3), *bottom-right:* ILEAS (S-binning, equation D.5).

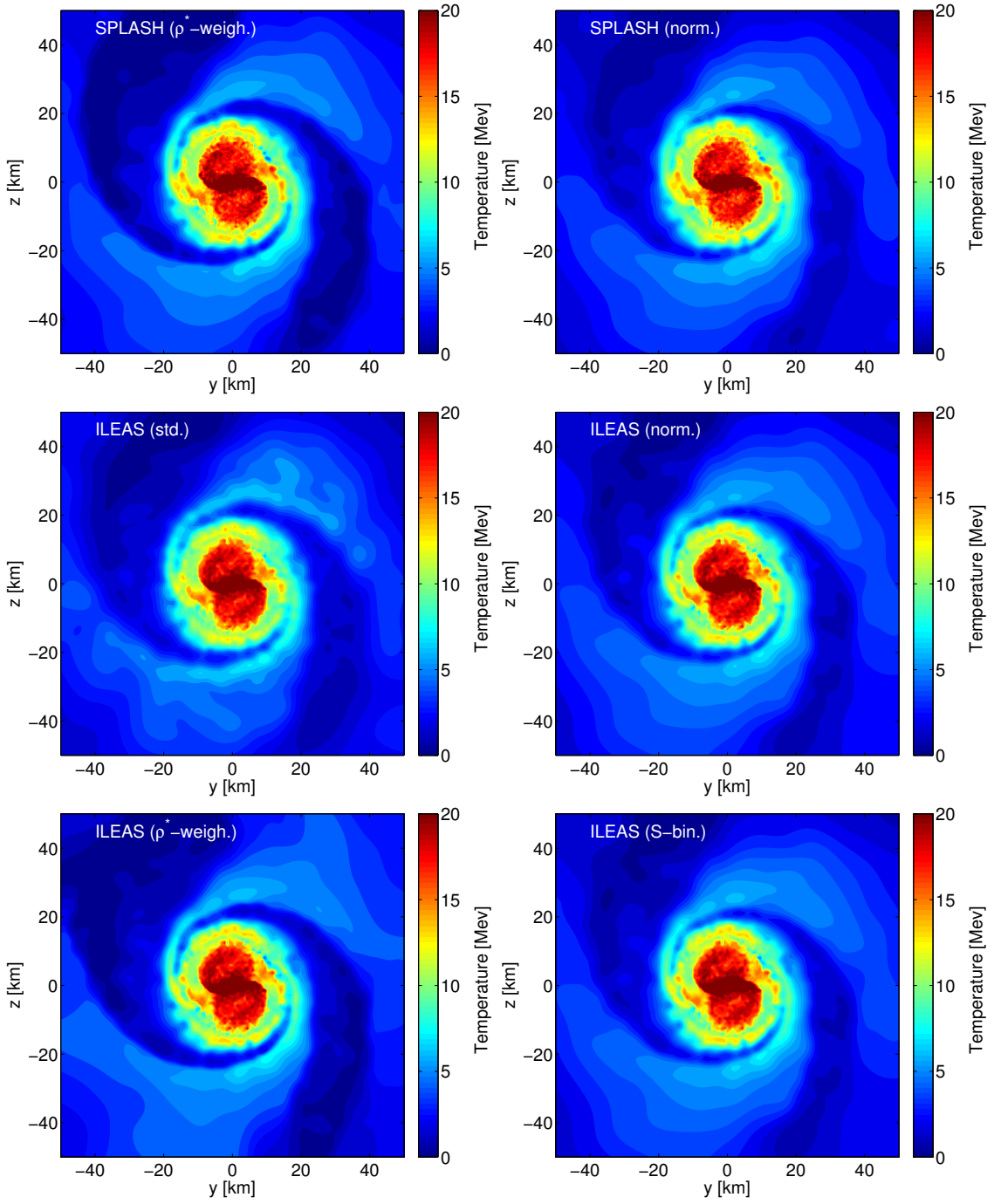

Figure D.2.: Temperature in the horizontal plane of a symmetric NS merger with 1.35 $M_\odot$ NSs and the DD2 EoS at 3 ms after the merger. Each panel shows the results obtained by different rendering procedures from SPH particles to a Cartesian grid. The programs and methods used for the rendering are: *top-left:* SPLASH (ρ^*-weighted, equation D.3), *top-right:* SPLASH (normalized, equation D.2), *centre-left:* ILEAS (standard, equation D.1), *centre-right:* ILEAS (normalized, equation D.3), *bottom-left:* ILEAS (ρ^*-weighted, equation D.3), *bottom-right:* ILEAS (S-binning, equation D.5).

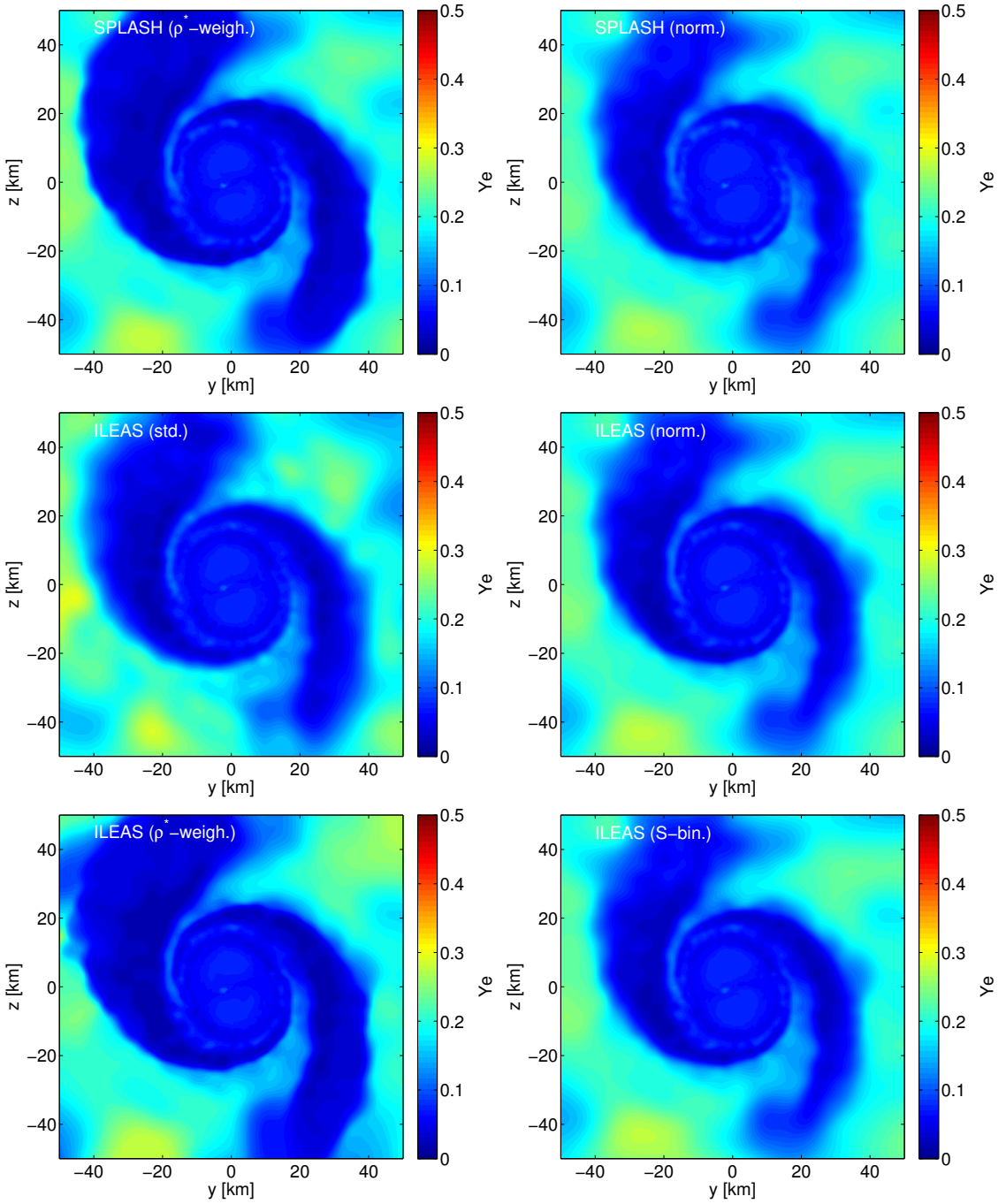

Figure D.3.: Electron fraction in the horizontal plane of a symmetric NS merger with 1.35 $M_\odot$ NSs and the DD2 EoS at 3 ms after the merger. Each panel shows the results obtained by different rendering procedures from SPH particles to a Cartesian grid. The programs and methods used for the rendering are: *top-left:* SPLASH (ρ^*-weighted, equation D.3), *top-right:* SPLASH (normalized, equation D.2), *centre-left:* ILEAS (standard, equation D.1), *centre-right:* ILEAS (normalized, equation D.3), *bottom-left:* ILEAS (ρ^*-weighted, equation D.3), *bottom-right:* ILEAS (S-binning, equation D.5).

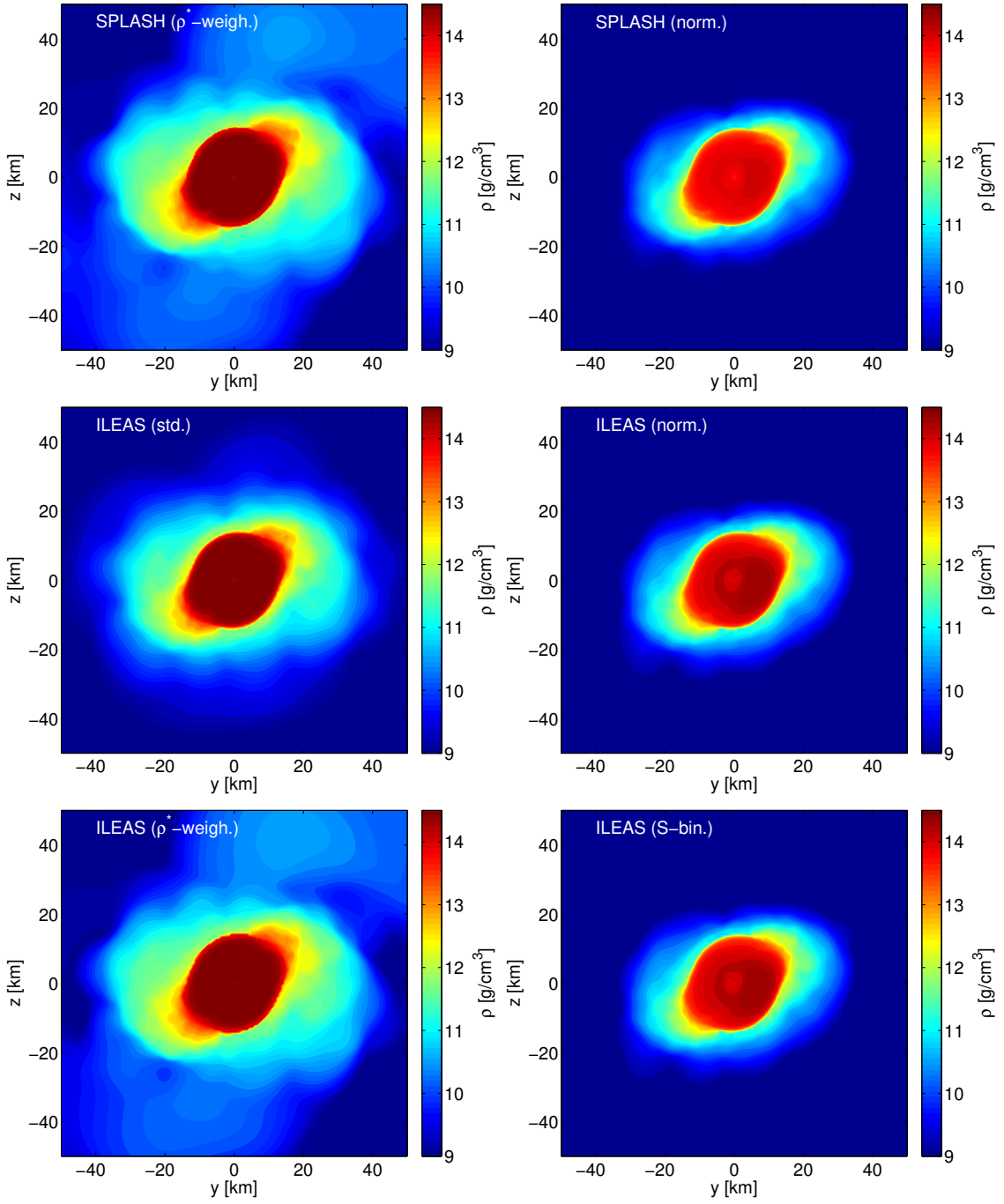

Figure D.4.: Rest mass density in the horizontal plane of a symmetric NS merger with 1.35 $M_\odot$ NSs and the DD2 EoS at 3 ms after the merger. Each panel shows the results obtained by different rendering procedures from SPH particles to a Cartesian grid. The programs and methods used for the rendering are: *top-left:* SPLASH (ρ^*-weighted, equation D.3), *top-right:* SPLASH (normalized, equation D.2), *centre-left:* ILEAS (standard, equation D.1), *centre-right:* ILEAS (normalized, equation D.3), *bottom-left:* ILEAS (ρ^*-weighted, equation D.3), *bottom-right:* ILEAS (S-binning, equation D.5).

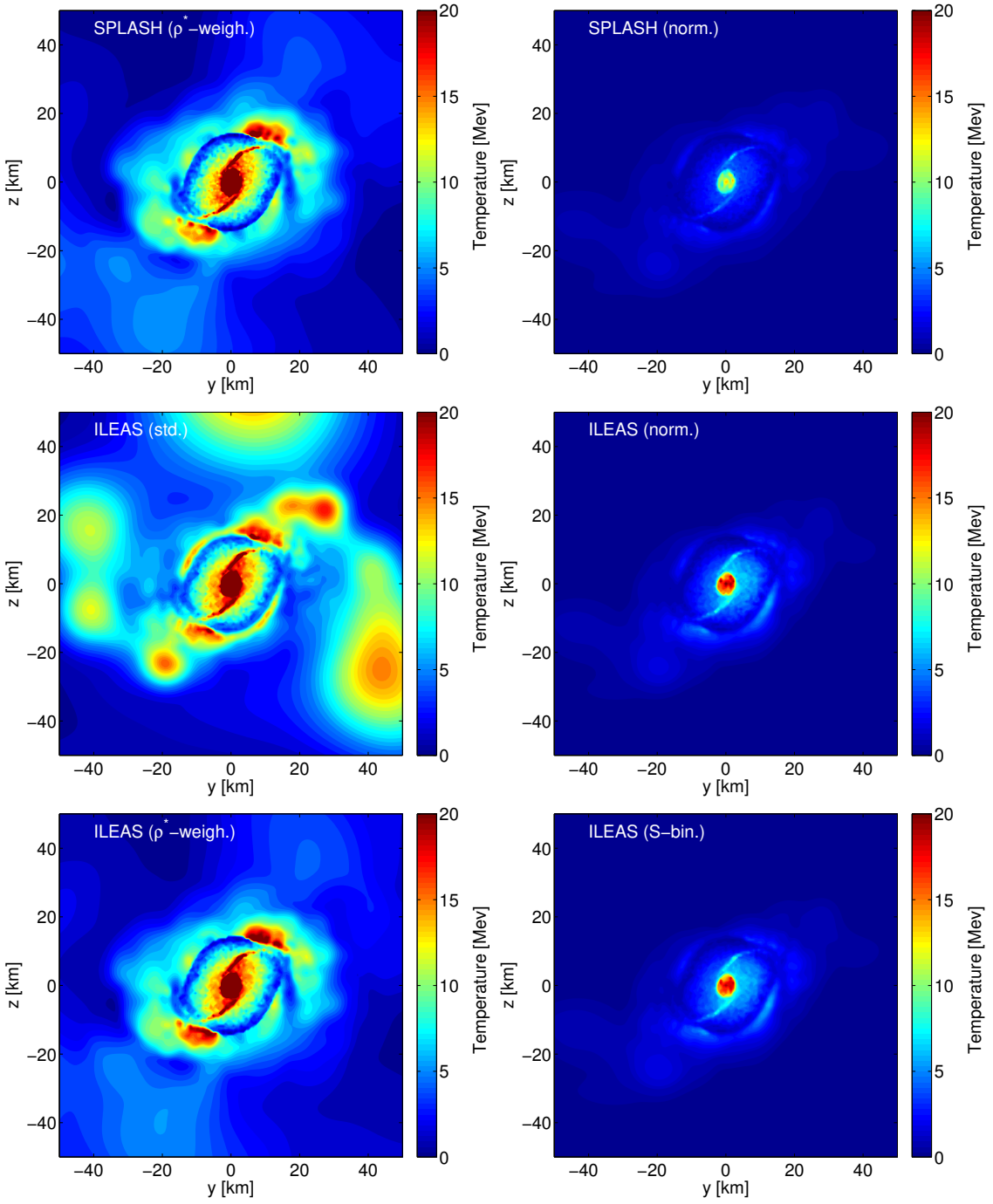

Figure D.5.: Temperature in the horizontal plane of a symmetric NS merger with 1.35 $M_\odot$ NSs and the DD2 EoS at 3 ms after the merger. Each panel shows the results obtained by different rendering procedures from SPH particles to a Cartesian grid. The programs and methods used for the rendering are: *top-left:* SPLASH (ρ^*-weighted, equation D.3), *top-right:* SPLASH (normalized, equation D.2), *centre-left:* ILEAS (standard, equation D.1), *centre-right:* ILEAS (normalized, equation D.3), *bottom-left:* ILEAS (ρ^*-weighted, equation D.3), *bottom-right:* ILEAS (S-binning, equation D.5).

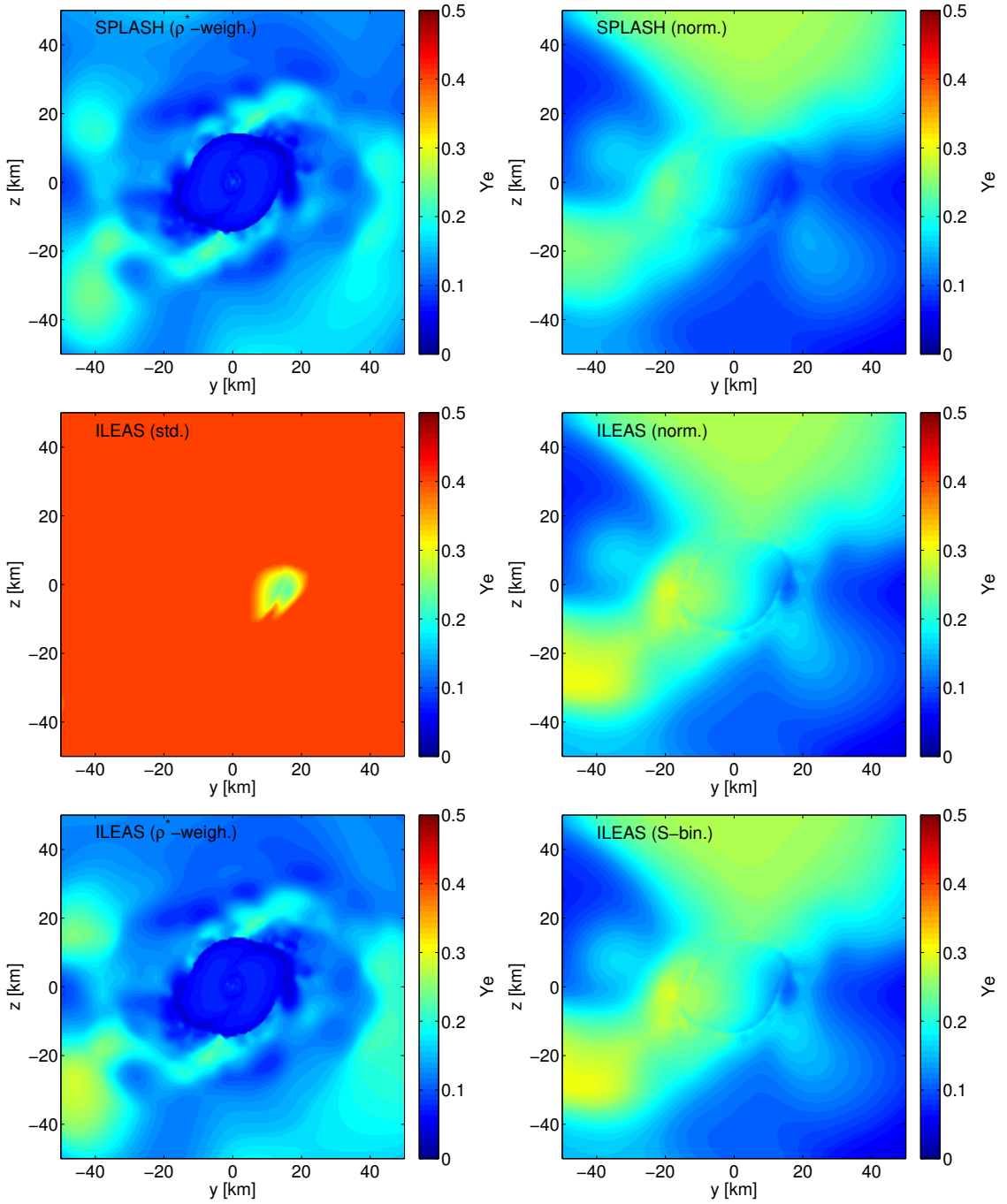

Figure D.6.: Electron fraction in the horizontal plane of a symmetric NS merger with 1.35 $M_\odot$ NSs and the DD2 EoS at 3 ms after the merger. Each panel shows the results obtained by different rendering procedures from SPH particles to a Cartesian grid. The programs and methods used for the rendering are: *top-left:* SPLASH (ρ^*-weighted, equation D.3), *top-right:* SPLASH (normalized, equation D.2), *centre-left:* ILEAS (standard, equation D.1), *centre-right:* ILEAS (normalized, equation D.3), *bottom-left:* ILEAS (ρ^*-weighted, equation D.3), *bottom-right:* ILEAS (S-binning, equation D.5).

E. Employed equations of state for neutron star matter

One of the most uncertain aspects of NSs is the equation of state (EoS) of matter beyond nuclear density ($\rho_{\rm nuc} \gtrsim 2.7 \cdot 10^{14}$ g/cm^3). The extreme conditions occurring in the core of a NS can not be reproduced in a laboratory, and the exact composition of NS matter remains a mystery. Although originally assumed to be composed mainly of neutrons, more exotic particles such as hyperons and mesons could also be present. It has also been proposed that NSs may be made of pure strange quark matter (see e.g. Stuart L. Shappiro 1983). Nuclear physicists perform experiments to constrain the properties of matter close to nuclear densities, as well as the coupling terms present in the nuclear forces between nucleons and hyperons (see Lattimer 2012 and Özel and Freire 2016 for recent reviews, and references therein). Astronomical observations can place constraints on the EoS as well. The most remarkable is the discovery of two NSs with exactly $\sim 2M_\odot$ by Demorest et al. (2010) and Antoniadis et al. (2013). For a theoretical EoS model to be plausible, it has to support a cold NS with a mass of at least $2M_\odot$, in agreement with the observed lower limit of the maximum NS mass. Further constraints are expected to be obtained in the near future with more detections of NS merger events, by making use of the GWs and the EM radiation. All of these experiments and observations combined with approximate descriptions of the particle interactions allow for the creation of reasonable EoS models which are widely used in numerical simulations (e.g. Shen et al. 1998; Hempel and Schaffner-Bielich 2010).

In order to close the set of evolution equations and to retrieve the thermodynamical quantities necessary for the computation of the weak interactions, we require an EoS of NS matter. For our presented simulations, we use several microphysical EoS in tabulated from, as functions of the density, ρ, the temperature, T, and the electron fraction, Y_e.

In section 3, we employed the SHEN EoS (Shen et al., 1998, 2011) for the evolution of a PNS, in the comparison between the performance of ILEAS and more sophisticated transport schemes. It is one of the most widely used EoS in the SN and merger community and, despite being one of the first microphysical EoS developed, it can support NSs of $2M_\odot$, as required by observations. Figure E.1 shows the mass-radius relation of a cold NS in neutrino-less β-equilibrium with the SHEN EoS.

For the NS merger simulations we have employed a set of EoS widely used in the literature in the context of NS mergers: DD2 (Typel et al., 2010), SFHo (Steiner et al., 2013) and TM1 (Sugahara and Toki, 1994). They are all based on the nucleon

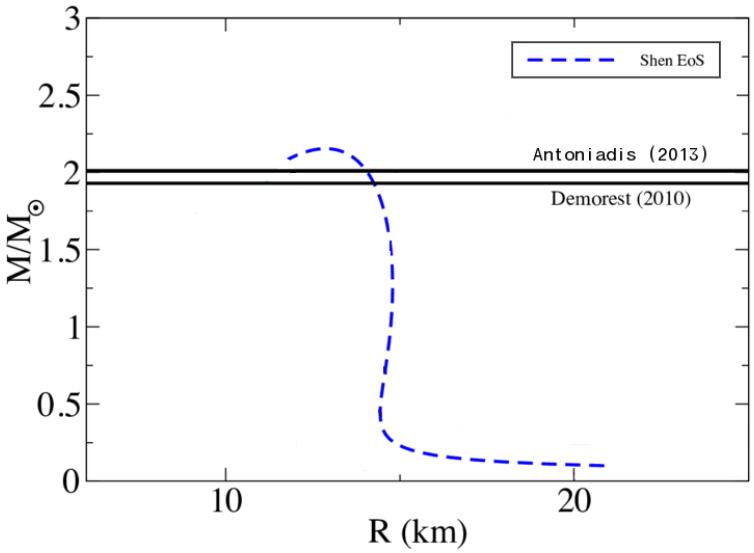

Figure E.1.: Mass radius relation of a cold NS in β-equilibrium with the SHEN EoS, which was employed in the comparisons with more sophisticated transport schemes in section (3). Picture modified from the original one found in Mathews et al. (2013).

mean field model described in Hempel and Schaffner-Bielich (2010) (with different parametrizations) and can support (within the error bars) a $2M_{\odot}$ NS. Figure E.2 allows for a direct comparison of the mass-radius relation of a cold NS when employing each of the three models. In both figures (E.1 and E.2) we show the two $\sim 2M_{\odot}$ NS observations for comparison. We chose these EoS in order to cover the spread in the predicted NS radius, which has not been unequivocally constrained, and has a significant impact on the merger dynamics. The soft EoS SFHo allows the formation of a more compact NS, whereas TM1 is a stiff EoS and, for a given mass, the resulting NS will have bigger radius.

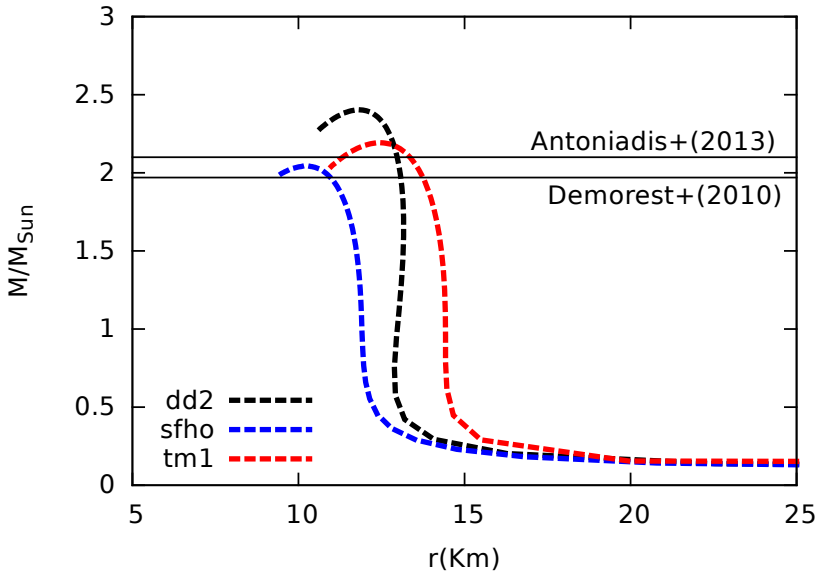

Figure E.2.: Mass radius relation of a cold NS in β-equilibrium with the DD2, SFHo and TM1 EoS, which was employed in the NS merger simulations in section 4.

Bibliography

J. Abadie, B. P. Abbott, R. Abbott, et al. TOPICAL REVIEW: Predictions for the rates of compact binary coalescences observable by ground-based gravitational-wave detectors. *Classical and Quantum Gravity*, 27(17):173001, Sept. 2010.

B. P. Abbott, R. Abbott, T. D. Abbott, et al. Prospects for Observing and Localizing Gravitational-Wave Transients with Advanced LIGO and Advanced Virgo. *Living Reviews in Relativity*, 19:1, Feb. 2016a.

B. P. Abbott, R. Abbott, T. D. Abbott, et al. Observation of Gravitational Waves from a Binary Black Hole Merger. *Physical Review Letters*, 116(6):061102, Feb. 2016b.

B. P. Abbott, R. Abbott, T. D. Abbott, et al. GW151226: Observation of Gravitational Waves from a 22-Solar-Mass Binary Black Hole Coalescence. *Physical Review Letters*, 116(24):241103, June 2016c.

B. P. Abbott, R. Abbott, T. D. Abbott, et al. Multi-messenger Observations of a Binary Neutron Star Merger. *ApJL*, 848:L12, Oct. 2017a.

B. P. Abbott, R. Abbott, T. D. Abbott, et al. Estimating the Contribution of Dynamical Ejecta in the Kilonova Associated with GW170817. *ApJL*, 850:L39, Dec. 2017b.

B. P. Abbott, R. Abbott, T. D. Abbott, et al. GW170608: Observation of a 19 Solar-mass Binary Black Hole Coalescence. *ApJL*, 851:L35, Dec. 2017c.

B. P. Abbott, R. Abbott, T. D. Abbott, et al. GW170104: Observation of a 50-Solar-Mass Binary Black Hole Coalescence at Redshift 0.2. *Physical Review Letters*, 118 (22):221101, June 2017d.

B. P. Abbott, R. Abbott, T. D. Abbott, et al. GW170814: A Three-Detector Observation of Gravitational Waves from a Binary Black Hole Coalescence. *Physical Review Letters*, 119(14):141101, Oct. 2017e.

B. P. Abbott, R. Abbott, T. D. Abbott, et al. GW170817: Observation of Gravitational Waves from a Binary Neutron Star Inspiral. *Physical Review Letters*, 119 (16):161101, Oct. 2017f.

M. Alcubierre. *Introduction to 3+1 Numerical Relativity*. Oxford Science Publications, 2008.

K. D. Alexander, E. Berger, W. Fong, et al. The Electromagnetic Counterpart of the Binary Neutron Star Merger LIGO/Virgo GW170817. VI. Radio Constraints on a Relativistic Jet and Predictions for Late-time Emission from the Kilonova Ejecta. *ApJL*, 848:L21, Oct. 2017.

J. Antoniadis, P. C. C. Freire, N. Wex, et al. A Massive Pulsar in a Compact Relativistic Binary. *Science*, 340:448, Apr. 2013.

W. D. Arnett. Type I supernovae. I - Analytic solutions for the early part of the light curve. *ApJ*, 253:785–797, Feb. 1982.

J. Barnes, D. Kasen, M.-R. Wu, and G. Martínez-Pinedo. Radioactivity and Thermalization in the Ejecta of Compact Object Mergers and Their Impact on Kilonova Light Curves. *ApJ*, 829:110, Oct. 2016.

A. Bauswein. *Relativistic simulations of compact object mergers for nucleonic matter and strange quark matter*. PhD thesis, Jan. 2010.

A. Bauswein, S. Goriely, and H.-T. Janka. Systematics of Dynamical Mass Ejection, Nucleosynthesis, and Radioactively Powered Electromagnetic Signals from Neutron-star Mergers. *ApJ*, 773:78, Aug. 2013.

A. Bauswein, R. Ardevol Pulpillo, H.-T. Janka, and S. Goriely. Nucleosynthesis Constraints on the Neutron Star-Black Hole Merger Rate. *ApJL*, 795:L9, Nov. 2014a.

A. Bauswein, N. Stergioulas, and H.-T. Janka. Revealing the high-density equation of state through binary neutron star mergers. *Phys. Rev. D*, 90(2):023002, July 2014b.

K. Belczynski, S. Repetto, D. E. Holz, et al. Compact Binary Merger Rates: Comparison with LIGO/Virgo Upper Limits. *ApJ*, 819:108, Mar. 2016.

S. Bernuzzi, D. Radice, C. D. Ott, et al. How loud are neutron star mergers? *Phys. Rev. D*, 94(2):024023, July 2016.

H. A. Bethe. Supernova mechanisms. *Reviews of Modern Physics*, 62:801–866, Oct. 1990.

H. A. Bethe and J. R. Wilson. Revival of a stalled supernova shock by neutrino heating. *ApJ*, 295:14–23, Aug. 1985.

L. Bildsten and C. Cutler. Tidal interactions of inspiraling compact binaries. *ApJ*, 400:175–180, Nov. 1992.

L. Blanchet and T. Damour. Post-Newtonian generation of gravitational waves. *Annales de L'Institut Henri Poincare Section (A) Physique Theorique*, 50:377–408, 1989.

R. D. Blandford and R. L. Znajek. Electromagnetic extraction of energy from Kerr black holes. *MNRAS*, 179:433–456, May 1977.

S. A. Bludman and K. A. van Riper. Diffusion approximation to neutrino transport in dense matter. *ApJ*, 224:631–642, Sept. 1978.

S. W. Bruenn. Stellar core collapse - Numerical model and infall epoch. *ApJS*, 58: 771–841, Aug. 1985.

E. M. Burbidge, G. R. Burbidge, W. A. Fowler, and F. Hoyle. Synthesis of the Elements in Stars. *Reviews of Modern Physics*, 29:547–650, 1957.

A. Burrows, S. Reddy, and T. A. Thompson. Neutrino opacities in nuclear matter. *Nuclear Physics A*, 777:356–394, Oct. 2006.

R. Chornock, E. Berger, D. Kasen, et al. The Electromagnetic Counterpart of the Binary Neutron Star Merger LIGO/Virgo GW170817. IV. Detection of Near-infrared Signatures of r-process Nucleosynthesis with Gemini-South. *ApJL*, 848: L19, Oct. 2017.

R. Ciolfi, W. Kastaun, B. Giacomazzo, et al. General relativistic magnetohydrodynamic simulations of binary neutron star mergers forming a long-lived neutron star. *Phys. Rev. D*, 95(6):063016, Mar. 2017.

J. Cooperstein, L. J. van den Horn, and E. A. Baron. Neutrino flows in collapsing stars - A two-fluid model. *ApJ*, 309:653–666, Oct. 1986.

J. Cooperstein, L. J. van den Horn, and E. Baron. Neutrino pair energy deposition in supernovae. *ApJL*, 321:L129–L132, Oct. 1987.

P. S. Cowperthwaite, E. Berger, V. A. Villar, et al. The Electromagnetic Counterpart of the Binary Neutron Star Merger LIGO/Virgo GW170817. II. UV, Optical, and Near-infrared Light Curves and Comparison to Kilonova Models. *ApJL*, 848:L17, Oct. 2017.

M. B. Davies, W. Benz, T. Piran, and F. K. Thielemann. Merging neutron stars. 1. Initial results for coalescence of noncorotating systems. *ApJ*, 431:742–753, Aug. 1994.

M. B. Deaton, M. D. Duez, F. Foucart, et al. Black Hole-Neutron Star Mergers with a Hot Nuclear Equation of State: Outflow and Neutrino-cooled Disk for a Low-mass, High-spin Case. *ApJ*, 776:47, Oct. 2013.

M. Della Valle. Supernovae and Gamma-Ray Bursts. *Chinese Journal of Astronomy and Astrophysics Supplement*, 6(1):315–322, Dec. 2006.

P. B. Demorest, T. Pennucci, S. M. Ransom, M. S. E. Roberts, and J. W. T. Hessels. A two-solar-mass neutron star measured using Shapiro delay. *Nature*, 467:1081–1083, Oct. 2010.

T. Dietrich, S. Bernuzzi, M. Ujevic, and W. Tichy. Gravitational waves and mass ejecta from binary neutron star mergers: Effect of the stars' rotation. *Phys. Rev. D*, 95(4):044045, Feb. 2017.

B. W. Dimitri Mihalas. *Foundations of Radiation Hydrodynamics*. Oxford University Press, 1984.

M. Dominik, E. Berti, R. O'Shaughnessy, et al. Double Compact Objects III: Gravitational-wave Detection Rates. *ApJ*, 806:263, June 2015.

M. D. Duez, F. Foucart, L. E. Kidder, et al. Evolving black hole-neutron star binaries in general relativity using pseudospectral and finite difference methods. *Phys. Rev. D*, 78(10):104015, Nov. 2008.

W. E. East, F. Pretorius, and B. C. Stephens. Eccentric black hole-neutron star mergers: Effects of black hole spin and equation of state. *Phys. Rev. D*, 85(12): 124009, June 2012.

D. Eichler, M. Livio, T. Piran, and D. N. Schramm. Nucleosynthesis, neutrino bursts and gamma-rays from coalescing neutron stars. *Nature*, 340:126–128, July 1989.

A. Einstein. Zur allgemeinen Relativitätstheorie. *Sitzungsberichte der Königlich Preußischen Akademie der Wissenschaften (Berlin), Seite 778-786.*, 1915.

A. Einstein. Über Gravitationswellen. *Sitzungsberichte der Königlich Preußischen Akademie der Wissenschaften (Berlin), Seite 154-167.*, 1918.

J. A. Faber and F. A. Rasio. Binary Neutron Star Mergers. *Living Reviews in Relativity*, 15:8, July 2012.

J. A. Faber, P. Grandclément, and F. A. Rasio. Mergers of irrotational neutron star binaries in conformally flat gravity. *Phys. Rev. D*, 69(12):124036, June 2004.

R. Fernández and B. D. Metzger. Delayed outflows from black hole accretion tori following neutron star binary coalescence. *MNRAS*, 435:502–517, Oct. 2013.

R. Fernández and B. D. Metzger. Electromagnetic Signatures of Neutron Star Mergers in the Advanced LIGO Era. *Annual Review of Nuclear and Particle Science*, 66:23–45, Oct. 2016a.

R. Fernández and B. D. Metzger. Electromagnetic Signatures of Neutron Star Mergers in the Advanced LIGO Era. *ArXiv e-prints*, Oct. 2016b.

R. Fernández, D. Kasen, B. D. Metzger, and E. Quataert. Outflows from accretion discs formed in neutron star mergers: effect of black hole spin. *MNRAS*, 446: 750–758, Jan. 2015a.

R. Fernández, E. Quataert, J. Schwab, D. Kasen, and S. Rosswog. The interplay of disc wind and dynamical ejecta in the aftermath of neutron star-black hole mergers. *MNRAS*, 449:390–402, May 2015b.

R. Fernández, F. Foucart, D. Kasen, et al. Dynamics, nucleosynthesis, and kilonova signature of black hole-neutron star merger ejecta. *Classical and Quantum Gravity*, 34(15):154001, Aug. 2017.

W. Fong, E. Berger, R. Margutti, and B. A. Zauderer. A Decade of Short-duration Gamma-Ray Burst Broadband Afterglows: Energetics, Circumburst Densities, and Jet Opening Angles. *ApJ*, 815:102, Dec. 2015.

W. Fong, E. Berger, P. K. Blanchard, et al. The Electromagnetic Counterpart of the Binary Neutron Star Merger LIGO/Virgo GW170817. VIII. A Comparison to Cosmological Short-duration Gamma-Ray Bursts. *ApJL*, 848:L23, Oct. 2017.

F. Foucart, M. B. Deaton, M. D. Duez, et al. Neutron star-black hole mergers with a nuclear equation of state and neutrino cooling: Dependence in the binary parameters. *Phys. Rev. D*, 90(2):024026, July 2014.

F. Foucart, E. O'Connor, L. Roberts, et al. Post-merger evolution of a neutron star-black hole binary with neutrino transport. *Phys. Rev. D*, 91(12):124021, June 2015.

F. Foucart, R. Haas, M. D. Duez, et al. Low mass binary neutron star mergers: Gravitational waves and neutrino emission. *Phys. Rev. D*, 93(4):044019, Feb. 2016.

F. Foucart, D. Desai, W. Brege, et al. Dynamical ejecta from precessing neutron star-black hole mergers with a hot, nuclear-theory based equation of state. *Classical and Quantum Gravity*, 34(4):044002, Feb. 2017.

S. Fujibayashi, Y. Sekiguchi, K. Kiuchi, and M. Shibata. Properties of Neutrino-driven Ejecta from the Remnant of a Binary Neutron Star Merger: Pure Radiation Hydrodynamics Case. *ApJ*, 846:114, Sept. 2017.

F. Galeazzi, W. Kastaun, L. Rezzolla, and J. A. Font. Implementation of a simplified approach to radiative transfer in general relativity. *Phys. Rev. D*, 88(6):064009, Sept. 2013.

R. A. Gingold and J. J. Monaghan. Smoothed particle hydrodynamics - Theory and application to non-spherical stars. *MNRAS*, 181:375–389, Nov. 1977.

B. P. Gompertz, P. T. O'Brien, G. A. Wynn, and A. Rowlinson. Can magnetar spin-down power extended emission in some short GRBs? *MNRAS*, 431:1745–1751, May 2013.

S. Goriely, A. Bauswein, and H.-T. Janka. r-process Nucleosynthesis in Dynamically Ejected Matter of Neutron Star Mergers. *ApJL*, 738:L32, Sept. 2011.

S. Goriely, A. Bauswein, O. Just, E. Pllumbi, and H.-T. Janka. Impact of weak interactions of free nucleons on the r-process in dynamical ejecta from neutron star mergers. *MNRAS*, 452:3894–3904, Oct. 2015.

O. Gottlieb, E. Nakar, and T. Piran. The cocoon emission - an electromagnetic counterpart to gravitational waves from neutron star mergers. *MNRAS*, 473:576–584, Jan. 2018.

J. Grindlay, S. Portegies Zwart, and S. McMillan. Short gamma-ray bursts from binary neutron star mergers in globular clusters. *Nature Physics*, 2:116–119, Feb. 2006.

S. Hannestad and G. Raffelt. Supernova Neutrino Opacity from Nucleon-Nucleon Bremsstrahlung and Related Processes. *ApJ*, 507:339–352, Nov. 1998.

T. Hecht. Deleptonisierung und Kuehlung junger Neutronensterne. Master's thesis, Technische Universität München, 1989. section 2.2.

M. Hempel and J. Schaffner-Bielich. A statistical model for a complete supernova equation of state. *Nuclear Physics A*, 837:210–254, June 2010.

F. Herwig. Evolution of Asymptotic Giant Branch Stars. *ARA& A*, 43:435–479, Sept. 2005.

C. J. Horowitz. Weak magnetism for antineutrinos in supernovae. *Phys. Rev. D*, 65 (4):043001, Feb. 2002.

K. Hotokezaka, S. Nissanke, G. Hallinan, et al. Radio Counterparts of Compact Binary Mergers Detectable in Gravitational Waves: A Simulation for an Optimized Survey. *ApJ*, 831:190, Nov. 2016.

L. Hüdepohl, B. Müller, H.-T. Janka, A. Marek, and G. G. Raffelt. Neutrino Signal of Electron-Capture Supernovae from Core Collapse to Cooling. *Physical Review Letters*, 104(25):251101, June 2010.

R. A. Hulse and J. H. Taylor. Discovery of a pulsar in a binary system. *ApJL*, 195: L51–L53, Jan. 1975.

H.-T. Janka. Implications of detailed neutrino transport for the heating by neutrino-antineutrino annihilation in supernova explosions. *A&A*, 244:378–382, Apr. 1991.

H.-T. Janka. Conditions for shock revival by neutrino heating in core-collapse supernovae. *A&A*, 368:527–560, Mar. 2001.

O. Just, A. Bauswein, R. A. Pulpillo, S. Goriely, and H.-T. Janka. Comprehensive nucleosynthesis analysis for ejecta of compact binary mergers. *MNRAS*, 448:541–567, Mar. 2015a.

O. Just, M. Obergaulinger, and H.-T. Janka. A new multidimensional, energy-dependent two-moment transport code for neutrino-hydrodynamics. *MNRAS*, 453:3386–3413, Nov. 2015b.

O. Just, M. Obergaulinger, H.-T. Janka, A. Bauswein, and N. Schwarz. Neutron-star Merger Ejecta as Obstacles to Neutrino-powered Jets of Gamma-Ray Bursts. *ApJL*, 816:L30, Jan. 2016.

D. Kasen, N. R. Badnell, and J. Barnes. Opacities and Spectra of the r-process Ejecta from Neutron Star Mergers. *ApJ*, 774:25, Sept. 2013.

D. Kasen, R. Fernández, and B. D. Metzger. Kilonova light curves from the disc wind outflows of compact object mergers. *MNRAS*, 450:1777–1786, June 2015.

D. Kasen, B. Metzger, J. Barnes, E. Quataert, and E. Ramirez-Ruiz. Origin of the heavy elements in binary neutron-star mergers from a gravitational-wave event. *Nature*, 551:80–84, Nov. 2017.

M. M. Kasliwal, E. Nakar, L. P. Singer, et al. Illuminating gravitational waves: A concordant picture of photons from a neutron star merger. *Science*, 358:1559–1565, Dec. 2017.

W. Kastaun and F. Galeazzi. Properties of hypermassive neutron stars formed in mergers of spinning binaries. *Phys. Rev. D*, 91(6):064027, Mar. 2015.

W. Kastaun, F. Galeazzi, D. Alic, L. Rezzolla, and J. A. Font. Black hole from merging binary neutron stars: How fast can it spin? *Phys. Rev. D*, 88(2):021501, July 2013.

T. L. Kay and J. T. Kajiya. Ray Tracing Complex Scenes. *Siggraph'86, Association for Computing Machinery*, 20(4), 1986.

C. Kim, B. B. P. Perera, and M. A. McLaughlin. Implications of psr j07373039b for the galactic nsns binary merger rate. *Monthly Notices of the Royal Astronomical Society*, 448(1):928–938, 2015.

K. Kiuchi, Y. Sekiguchi, K. Kyutoku, and M. Shibata. Gravitational waves, neutrino emissions and effects of hyperons in binary neutron star mergers. *Classical and Quantum Gravity*, 29(12):124003, June 2012.

K. Kiuchi, Y. Sekiguchi, K. Kyutoku, et al. High resolution magnetohydrodynamic simulation of black hole-neutron star merger: Mass ejection and short gamma ray bursts. *Phys. Rev. D*, 92(6):064034, Sept. 2015.

C. S. Kochanek. Coalescing binary neutron stars. *ApJ*, 398:234–247, Oct. 1992.

O. Korobkin, S. Rosswog, A. Arcones, and C. Winteler. On the astrophysical robustness of the neutron star merger r-process. *MNRAS*, 426:1940–1949, Nov. 2012.

S. R. Kulkarni. Modeling Supernova-like Explosions Associated with Gamma-ray Bursts with Short Durations. *ArXiv Astrophysics e-prints*, Oct. 2005.

K. Kyutoku, K. Ioka, and M. Shibata. Anisotropic mass ejection from black hole-neutron star binaries: Diversity of electromagnetic counterparts. *Phys. Rev. D*, 88(4):041503, Aug. 2013.

K. Kyutoku, K. Kiuchi, Y. Sekiguchi, M. Shibata, and K. Taniguchi. Neutrino transport in black hole-neutron star binaries: Neutrino emission and dynamical mass ejection. *Phys. Rev. D*, 97(2):023009, Jan. 2018.

A. Lattimer, J. Steiner. stellarcollapse.org. http://www.stellarcollapse.org/nsmasses. Accessed: 2018-02-21.

J. M. Lattimer. The Nuclear Equation of State and Neutron Star Masses. *Annual Review of Nuclear and Particle Science*, 62:485–515, Nov. 2012.

J. M. Lattimer and D. N. Schramm. Black-hole-neutron-star collisions. *ApJL*, 192: L145–L147, Sept. 1974.

W. H. Lee, E. Ramirez-Ruiz, and D. López-Cámara. Phase Transitions and He-Synthesis-Driven Winds in Neutrino Cooled Accretion Disks: Prospects for Late Flares in Short Gamma-Ray Bursts. *ApJL*, 699:L93–L96, July 2009.

L. Lehner, S. L. Liebling, C. Palenzuela, et al. Unequal mass binary neutron star mergers and multimessenger signals. *Classical and Quantum Gravity*, 33(18): 184002, Sept. 2016a.

L. Lehner, S. L. Liebling, C. Palenzuela, and P. M. Motl. m =1 instability and gravitational wave signal in binary neutron star mergers. *Phys. Rev. D*, 94(4): 043003, Aug. 2016b.

C. D. Levermore and G. C. Pomraning. A flux-limited diffusion theory. *ApJ*, 248: 321–334, Aug. 1981.

L.-X. Li and B. Paczyński. Transient Events from Neutron Star Mergers. *ApJL*, 507:L59–L62, Nov. 1998.

LIGO. ligo.caltech.edu. https://www.ligo.caltech.edu/page/facts. Accessed: 2018-05-4.

R. W. Lindquist. Relativistic transport theory. *Annals of Physics*, 37:487–518, May 1966.

J. Lippuner, R. Fernández, L. F. Roberts, et al. Signatures of hypermassive neutron star lifetimes on r-process nucleosynthesis in the disc ejecta from neutron star mergers. *MNRAS*, 472:904–918, Nov. 2017.

L. B. Lucy. A numerical approach to the testing of the fission hypothesis. *AJ*, 82: 1013–1024, Dec. 1977.

R. Margutti, E. Berger, W. Fong, et al. The Electromagnetic Counterpart of the Binary Neutron Star Merger LIGO/Virgo GW170817. V. Rising X-Ray Emission from an Off-axis Jet. *ApJL*, 848:L20, Oct. 2017.

D. Martin, A. Perego, W. Kastaun, and A. Arcones. The role of weak interactions in dynamic ejecta from binary neutron star mergers. *Classical and Quantum Gravity*, 35(3):034001, Feb. 2018.

J. G. Martinez, K. Stovall, P. C. C. Freire, et al. Pulsar J0453+1559: A Double Neutron Star System with a Large Mass Asymmetry. *ApJ*, 812:143, Oct. 2015.

G. Martínez-Pinedo, T. Fischer, A. Lohs, and L. Huther. Charged-Current Weak Interaction Processes in Hot and Dense Matter and its Impact on the Spectra of Neutrinos Emitted from Protoneutron Star Cooling. *Physical Review Letters*, 109 (25):251104, Dec. 2012.

D. V. Martynov, E. D. Hall, B. P. Abbott, et al. Sensitivity of the Advanced LIGO detectors at the beginning of gravitational wave astronomy. *Phys. Rev. D*, 93(11): 112004, June 2016.

G. J. Mathews, M. Meixner, J. P. Olson, et al. Updates of the nuclear equation of state for core-collapse supernovae and neutron stars: effects of 3-body forces, QCD, and magnetic fields. In *Journal of Physics Conference Series*, volume 445 of *Journal of Physics Conference Series*, page 012023, July 2013.

N. Mennekens and D. Vanbeveren. Massive double compact object mergers: gravitational wave sources and r-process element production sites. *A&A*, 564:A134, Apr. 2014.

B. D. Metzger. Kilonovae. *Living Reviews in Relativity*, 20:3, May 2017.

B. D. Metzger and R. Fernández. Red or blue? A potential kilonova imprint of the delay until black hole formation following a neutron star merger. *MNRAS*, 441: 3444–3453, July 2014.

B. D. Metzger, G. Martínez-Pinedo, S. Darbha, et al. Electromagnetic counterparts of compact object mergers powered by the radioactive decay of r-process nuclei. *MNRAS*, 406:2650–2662, Aug. 2010.

B. D. Metzger, A. Bauswein, S. Goriely, and D. Kasen. Neutron-powered precursors of kilonovae. *MNRAS*, 446:1115–1120, Jan. 2015.

A. Mezzacappa and S. W. Bruenn. Type II supernovae and Boltzmann neutrino transport - The infall phase. *ApJ*, 405:637–668, Mar. 1993.

E. Nakar and T. Piran. Detectable radio flares following gravitational waves from mergers of binary neutron stars. *Nature*, 478:82–84, Oct. 2011.

D. Neilsen, S. L. Liebling, M. Anderson, et al. Magnetized neutron stars with realistic equations of state and neutrino cooling. *Phys. Rev. D*, 89(10):104029, May 2014.

M. Nicholl, E. Berger, D. Kasen, et al. The Electromagnetic Counterpart of the Binary Neutron Star Merger LIGO/Virgo GW170817. III. Optical and UV Spectra of a Blue Kilonova from Fast Polar Ejecta. *ApJL*, 848:L18, Oct. 2017.

J. P. Norris and J. T. Bonnell. Short Gamma-Ray Bursts with Extended Emission. *ApJ*, 643:266–275, May 2006.

E. O'Connor. An Open-source Neutrino Radiation Hydrodynamics Code for Core-collapse Supernovae. *ApJS*, 219:24, Aug. 2015.

E. O'Connor and C. D. Ott. A new open-source code for spherically symmetric stellar collapse to neutron stars and black holes. *Classical and Quantum Gravity*, 27(11):114103, June 2010.

R. Oechslin, S. Rosswog, and F.-K. Thielemann. Conformally flat smoothed particle hydrodynamics application to neutron star mergers. *Phys. Rev. D*, 65(10):103005, May 2002.

R. Oechslin, H.-T. Janka, and A. Marek. Relativistic neutron star merger simulations with non-zero temperature equations of state. I. Variation of binary parameters and equation of state. *A&A*, 467:395–409, May 2007.

F. Özel and P. Freire. Masses, Radii, and the Equation of State of Neutron Stars. *ARA& A*, 54:401–440, Sept. 2016.

B. Paczynski. Gamma-ray bursters at cosmological distances. *ApJL*, 308:L43–L46, Sept. 1986.

C. Palenzuela, L. Lehner, M. Ponce, et al. Electromagnetic and Gravitational Outputs from Binary-Neutron-Star Coalescence. *Physical Review Letters*, 111(6): 061105, Aug. 2013.

C. Palenzuela, S. L. Liebling, D. Neilsen, et al. Effects of the microphysical equation of state in the mergers of magnetized neutron stars with neutrino cooling. *Phys. Rev. D*, 92(4):044045, Aug. 2015.

V. Paschalidis, M. Ruiz, and S. L. Shapiro. Relativistic Simulations of Black Hole-Neutron Star Coalescence: The Jet Emerges. *ApJL*, 806:L14, June 2015.

A. Perego, E. Gafton, R. Cabezón, S. Rosswog, and M. Liebendörfer. MODA: a new algorithm to compute optical depths in multidimensional hydrodynamic simulations. *A&A*, 568:A11, Aug. 2014a.

A. Perego, S. Rosswog, R. M. Cabezón, et al. Neutrino-driven winds from neutron star merger remnants. *MNRAS*, 443:3134–3156, Oct. 2014b.

A. Perego, R. M. Cabezón, and R. Käppeli. An Advanced Leakage Scheme for Neutrino Treatment in Astrophysical Simulations. *ApJS*, 223:22, Apr. 2016.

A. Perego, D. Radice, and S. Bernuzzi. AT 2017gfo: An Anisotropic and Three-component Kilonova Counterpart of GW170817. *ApJL*, 850:L37, Dec. 2017.

E. Pian, P. D'Avanzo, S. Benetti, et al. Spectroscopic identification of r-process nucleosynthesis in a double neutron-star merger. *Nature*, 551:67–70, Nov. 2017.

K. A. Postnov and L. R. Yungelson. The Evolution of Compact Binary Star Systems. *Living Reviews in Relativity*, 17:3, May 2014.

D. J. Price. splash: An Interactive Visualisation Tool for Smoothed Particle Hydrodynamics Simulations. *PASA*, 24:159–173, Oct. 2007.

D. Radice. General-relativistic Large-eddy Simulations of Binary Neutron Star Mergers. *ApJL*, 838:L2, Mar. 2017.

D. Radice, F. Galeazzi, J. Lippuner, et al. Dynamical mass ejection from binary neutron star mergers. *MNRAS*, 460:3255–3271, Aug. 2016.

D. Radice, S. Bernuzzi, W. Del Pozzo, L. F. Roberts, and C. D. Ott. Probing Extreme-density Matter with Gravitational-wave Observations of Binary Neutron Star Merger Remnants. *ApJL*, 842:L10, June 2017.

D. Radice, A. Perego, F. Zappa, and S. Bernuzzi. GW170817: Joint Constraint on the Neutron Star Equation of State from Multimessenger Observations. *ApJL*, 852:L29, Jan. 2018.

M. Rampp. *Radiation hydrodynamics with neutrinos: Stellar core collapse and explosion mechanism of type II supernovae.* PhD thesis, Technische Universität München, 2000.

M. Rampp and H.-T. Janka. Radiation hydrodynamics with neutrinos. Variable Eddington factor method for core-collapse supernova simulations. *A&A*, 396:361–392, Dec. 2002.

F. A. Rasio and S. L. Shapiro. Hydrodynamics of binary coalescence. 1: Polytropes with stiff equations of state. *ApJ*, 432:242–261, Sept. 1994.

S. Reddy, M. Prakash, and J. M. Lattimer. Neutrino interactions in hot and dense matter. *Phys. Rev. D*, 58(1):013009, July 1998.

S. Richers, D. Kasen, E. O'Connor, R. Fernández, and C. D. Ott. Monte Carlo Neutrino Transport through Remnant Disks from Neutron Star Mergers. *ApJ*, 813:38, Nov. 2015.

L. F. Roberts. A New Code for Proto-neutron Star Evolution. *ApJ*, 755:126, Aug. 2012.

L. F. Roberts, S. Reddy, and G. Shen. Medium modification of the charged-current neutrino opacity and its implications. *Phys. Rev. C*, 86(6):065803, Dec. 2012.

S. Rosswog. Fallback accretion in the aftermath of a compact binary merger. *MNRAS*, 376:L48–L51, Mar. 2007.

S. Rosswog. The dynamic ejecta of compact object mergers and eccentric collisions. *Philosophical Transactions of the Royal Society of London Series A*, 371: 20120272–20120272, Apr. 2013.

S. Rosswog. The multi-messenger picture of compact binary mergers. *International Journal of Modern Physics D*, 24:1530012-52, Feb. 2015a.

S. Rosswog. SPH Methods in the Modelling of Compact Objects. *Living Reviews in Computational Astrophysics*, 1:1, Oct. 2015b.

S. Rosswog and M. Liebendörfer. High-resolution calculations of merging neutron stars - II. Neutrino emission. *MNRAS*, 342:673–689, July 2003.

S. Rosswog, E. Ramirez-Ruiz, and M. B. Davies. High-resolution calculations of merging neutron stars - III. Gamma-ray bursts. *MNRAS*, 345:1077–1090, Nov. 2003.

S. Rosswog, T. Piran, and E. Nakar. The multimessenger picture of compact object encounters: binary mergers versus dynamical collisions. *MNRAS*, 430:2585–2604, Apr. 2013.

B. Röttgers and A. Arth. SPH to Grid: a new integral conserving method. *ArXiv e-prints*, Mar. 2018.

M. Ruffert and H.-T. Janka. Gamma-ray bursts from accreting black holes in neutron star mergers. *A&A*, 344:573–606, Apr. 1999.

M. Ruffert and H.-T. Janka. Coalescing neutron stars - A step towards physical models. III. Improved numerics and different neutron star masses and spins. *A&A*, 380:544–577, Dec. 2001.

M. Ruffert, H.-T. Janka, and G. Schaefer. Coalescing neutron stars - a step towards physical models. I. Hydrodynamic evolution and gravitational-wave emission. *A&A*, 311:532–566, July 1996.

M. Ruffert, H.-T. Janka, K. Takahashi, and G. Schaefer. Coalescing neutron stars - a step towards physical models. II. Neutrino emission, neutron tori, and gamma-ray bursts. *A&A*, 319:122–153, Mar. 1997.

M. Ruiz, R. N. Lang, V. Paschalidis, and S. L. Shapiro. Binary Neutron Star Mergers: A Jet Engine for Short Gamma-Ray Bursts. *ApJL*, 824:L6, June 2016.

J. Samsing, M. MacLeod, and E. Ramirez-Ruiz. The Formation of Eccentric Compact Binary Inspirals and the Role of Gravitational Wave Emission in Binary-Single Stellar Encounters. *ApJ*, 784:71, Mar. 2014.

Y. Sekiguchi. An implementation of the microphysics in full general relativity: a general relativistic neutrino leakage scheme. *Classical and Quantum Gravity*, 27 (11):114107, June 2010.

Y. Sekiguchi, K. Kiuchi, K. Kyutoku, and M. Shibata. Gravitational Waves and Neutrino Emission from the Merger of Binary Neutron Stars. *Physical Review Letters*, 107(5):051102, July 2011a.

Y. Sekiguchi, K. Kiuchi, K. Kyutoku, and M. Shibata. Effects of Hyperons in Binary Neutron Star Mergers. *Physical Review Letters*, 107(21):211101, Nov. 2011b.

Y. Sekiguchi, K. Kiuchi, K. Kyutoku, and M. Shibata. Current status of numerical-relativity simulations in Kyoto. *Progress of Theoretical and Experimental Physics*, 2012(1):01A304, Oct. 2012.

Y. Sekiguchi, K. Kiuchi, K. Kyutoku, and M. Shibata. Dynamical mass ejection from binary neutron star mergers: Radiation-hydrodynamics study in general relativity. *Phys. Rev. D*, 91(6):064059, Mar. 2015.

Y. Sekiguchi, K. Kiuchi, K. Kyutoku, M. Shibata, and K. Taniguchi. Dynamical mass ejection from the merger of asymmetric binary neutron stars: Radiation-hydrodynamics study in general relativity. *Phys. Rev. D*, 93(12):124046, June 2016.

B. J. Shappee, J. D. Simon, M. R. Drout, et al. Early spectra of the gravitational wave source GW170817: Evolution of a neutron star merger. *Science*, 358:1574–1578, Dec. 2017.

H. Shen, H. Toki, K. Oyamatsu, and K. Sumiyoshi. Relativistic equation of state of nuclear matter for supernova and neutron star. *Nuclear Physics A*, 637:435–450, July 1998.

H. Shen, H. Toki, K. Oyamatsu, and K. Sumiyoshi. Relativistic Equation of State for Core-collapse Supernova Simulations. *ApJS*, 197:20, Dec. 2011.

M. Shibata and K. Taniguchi. Coalescence of Black Hole-Neutron Star Binaries. *Living Reviews in Relativity*, 14:6, Aug. 2011.

M. Shibata, T. Nakamura, and K.-i. Oohara. Coalescence of Spinning Binary Neutron Stars of Equal Mass — 3D Numerical Simulations —. *Progress of Theoretical Physics*, 88:1079–1095, Dec. 1992.

M. Shibata, Y.-I. Sekiguchi, and R. Takahashi. Magnetohydrodynamics of Neutrino-Cooled Accretion Tori around a Rotating Black Hole in General Relativity. *Progress of Theoretical Physics*, 118:257–302, Aug. 2007.

M. Shibata, K. Kiuchi, Y. Sekiguchi, and Y. Suwa. Truncated Moment Formalism for Radiation Hydrodynamics in Numerical Relativity. *Progress of Theoretical Physics*, 125:1255–1287, June 2011.

M. Shibata, S. Fujibayashi, K. Hotokezaka, et al. Modeling GW170817 based on numerical relativity and its implications. *Phys. Rev. D*, 96(12):123012, Dec. 2017.

S. J. Smartt, T.-W. Chen, A. Jerkstrand, et al. A kilonova as the electromagnetic counterpart to a gravitational-wave source. *Nature*, 551:75–79, Nov. 2017.

E. V. S.N. Shore, M.Livio. *Interacting Binaries*. Springer-Verlag, 1992.

C. Sneden, J. J. Cowan, and R. Gallino. Neutron-Capture Elements in the Early Galaxy. *ARA& A*, 46:241–288, Sept. 2008.

M. Soares-Santos, D. E. Holz, J. Annis, et al. The Electromagnetic Counterpart of the Binary Neutron Star Merger LIGO/Virgo GW170817. I. Discovery of the Optical Counterpart Using the Dark Energy Camera. *ApJL*, 848:L16, Oct. 2017.

A. W. Steiner, M. Hempel, and T. Fischer. Core-collapse Supernova Equations of State Based on Neutron Star Observations. *ApJ*, 774:17, Sept. 2013.

S. A. T. Stuart L. Shappiro. *Black Holes, White Dwarfs and Neutron Stars: the physics of compact objects*. Wiley-VCH, 1983.

Y. Sugahara and H. Toki. Relativistic mean-field theory for unstable nuclei with non-linear σ and ω terms. *Nuclear Physics A*, 579:557–572, Oct. 1994.

J. K. Swiggum, R. Rosen, M. A. McLaughlin, et al. PSR J1930-1852: a Pulsar in the Widest Known Orbit around Another Neutron Star. *ApJ*, 805:156, June 2015.

K. Takahashi, M. F. El Eid, and W. Hillebrandt. Beta transition rates in hot and dense matter. *A&A*, 67:185–197, July 1978.

M. Tanaka, Y. Utsumi, P. A. Mazzali, et al. Kilonova from post-merger ejecta as an optical and near-Infrared counterpart of GW170817. *PASJ*, 69:102, Dec. 2017.

M. Tanaka, D. Kato, G. Gaigalas, et al. Properties of Kilonovae from Dynamical and Post-merger Ejecta of Neutron Star Mergers. *ApJ*, 852:109, Jan. 2018.

T. M. Tauris, N. Langer, and P. Podsiadlowski. Ultra-stripped supernovae: progenitors and fate. *MNRAS*, 451:2123–2144, Aug. 2015.

J. H. Taylor and J. M. Weisberg. Further experimental tests of relativistic gravity using the binary pulsar PSR 1913 + 16. *ApJ*, 345:434–450, Oct. 1989.

F.-K. Thielemann, M. Eichler, I. V. Panov, and B. Wehmeyer. Neutron Star Mergers and Nucleosynthesis of Heavy Elements. *Annual Review of Nuclear and Particle Science*, 67:253–274, Oct. 2017.

T. A. Thompson, A. Burrows, and J. E. Horvath. μ and τ neutrino thermalization and production in supernovae: Processes and time scales. *Phys. Rev. C*, 62(3): 035802, Sept. 2000.

S. Typel, G. Röpke, T. Klähn, D. Blaschke, and H. H. Wolter. Composition and thermodynamics of nuclear matter with light clusters. *Phys. Rev. C*, 81(1):015803, Jan. 2010.

S. Wanajo, Y. Sekiguchi, N. Nishimura, et al. Production of All the r-process Nuclides in the Dynamical Ejecta of Neutron Star Mergers. *ApJL*, 789:L39, July 2014.

J. M. Weisberg and J. H. Taylor. The Relativistic Binary Pulsar B1913+16: Thirty Years of Observations and Analysis. In F. A. Rasio and I. H. Stairs, editors, *Binary Radio Pulsars*, volume 328 of *Astronomical Society of the Pacific Conference Series*, page 25, July 2005.

J. R. Wilson, R. Couch, S. Cochran, J. Le Blanc, and Z. Barkat. Neutrino flow and the collapse of stellar cores. In P. G. Bergman, E. J. Fenyves, and L. Motz, editors, *Seventh Texas Symposium on Relativistic Astrophysics*, volume 262 of *Annals of the New York Academy of Sciences*, pages 54–64, Oct. 1975.

J. R. Wilson, G. J. Mathews, and P. Marronetti. Relativistic numerical model for close neutron-star binaries. *Phys. Rev. D*, 54:1317–1331, July 1996.

M.-R. Wu and I. Tamborra. Fast neutrino conversions: Ubiquitous in compact binary merger remnants. *Phys. Rev. D*, 95(10):103007, May 2017.

M.-R. Wu, R. Fernández, G. Martínez-Pinedo, and B. D. Metzger. Production of the entire range of r-process nuclides by black hole accretion disc outflows from neutron star mergers. *MNRAS*, 463:2323–2334, Dec. 2016.

M.-R. Wu, I. Tamborra, O. Just, and H.-T. Janka. Imprints of neutrino-pair flavor conversions on nucleosynthesis in ejecta from neutron-star merger remnants. *Phys. Rev. D*, 96(12):123015, Dec. 2017.

Z. Xing, J. M. Centrella, and S. L. W. McMillan. Gravitational radiation from coalescing binary neutron stars. *Phys. Rev. D*, 50:6247–6261, Nov. 1994.

F. Zappa, S. Bernuzzi, D. Radice, A. Perego, and T. Dietrich. Gravitational-Wave Luminosity of Binary Neutron Stars Mergers. *Physical Review Letters*, 120(11): 111101, Mar. 2018.